BIOPROSTHETIC PULMONARY VALVE HEMODYNAMICS IN TETRALOGY OF FALLOT PATIENTS

By
Nicole K. Schiavone, John K. Eaton and Alison Marsden

Prepared with support from
the American Heart Association
the Stanford Bio-X Bowes Fellowship,
the Stanford Graduate Fellowship,
the Stanford Maternal and Child Health Research Institute, and
the Vera Moulton Will Center for Pulmonary Vascular Disease

Report No. TF-181

Flow Physics and Computational Engineering Group
Department of Mechanical Engineering
Stanford University
Stanford, CA 94305

August 2021

Bioprosthetic Pulmonary Valve Hemodynamics In Tetralogy of Fallot Patients

By
Nicole K. Schiavone, John K. Eaton and Alison Marsden

Prepared with support from
the American Heart Association
the Stanford Bio-X Bowes Fellowship,
the Stanford Graduate Fellowship,
the Stanford Maternal and Child Health Research Institute, and
the Vera Moulton Will Center for Pulmonary Vascular Disease

Report No. TF-181

Flow Physics and Computational Engineering Group
Department of Mechanical Engineering
Stanford University
Stanford, CA 94305

August 2021

Abstract

Tetralogy of Fallot (ToF) is a congenital heart defect affecting 1 in 2500 live births annually in the United States, making it the most common defect with deficient blood oxygenation. ToF is comprised of four different defects: a ventricular septal defect (VSD), an overriding aorta, right ventricular hypertrophy, and right ventricular outflow tract (RVOT) obstruction. Typical surgical repair for ToF requires an initial surgery at a few months of age to close the VSD and reconstruct the RVOT. The defects and repair often leave the patient without a fully functional pulmonary valve. Pulmonary valve replacement (PVR) is necessary in most ToF patients in their early teen years to restore pulmonary valve function. Bioprosthetic valves, which are the commonly used prostheses in PVR, are subject to degradation and dysfunction over time, typically within 15 years of implantation and often leading to additional surgical interventions. However, these valves fail early and unpredictably in as many as 30% of ToF patients and there is currently little understanding of what hemodynamic and anatomic factors may lead to early valve dysfunction. The objectives of this thesis were to determine the impact of patient-specific features such as RVOT anatomy, cardiac output, and valve orientation and placement during PVR on the hemodynamics local to the bioprosthetic valve.

We developed a physiological flow loop to study hemodynamics in 3D printed anatomical models of the RVOT with an implanted 25mm St. Jude Medical Epic surgical valve. Full 3D, three-component, phase-averaged velocity fields were obtained using 4D flow MRI. The scans were phase-locked with the trigger signal driving the pulsatile flow, allowing us to capture multiple time points over the cardiac cycle.

The effects of RVOT anatomy were evaluated by comparing a healthy control model to a diseased model with a dilated main pulmonary artery (MPA). For both models, we also studied two valve orientations: the native orientation of healthy pulmonary valves and an orientation rotated 180 degrees from native. The cardiac output was 3.5 L/min for these experiments. Flow features, such as recirculation, vortex formation, and reversed flow regions, differed significantly with the RVOT anatomy and valve orientation. All cases produced asymmetry in the streamwise velocity while the dilated MPA anatomy revealed additional asymmetry in the radial flows. Quantitative integral metrics quantified the streamwise momentum and secondary flow strength in each of the cases. The dilated MPA geometry with the rotated orientation had increased secondary flow strength and recirculation, which demonstrated the compound effect of RVOT anatomy and valve orientation on the hemodynamics.

The dilated MPA model was used to assess the impact of varying cardiac output. We conducted 4D flow MRI experiments for three cardiac outputs with the native valve orientation: 2 L/min, 3.5 L/min, and 5 L/min. The 2 L/min and 3.5 L/min cases were also studied with the rotated orientation. High-speed imaging experiments visualized the valve leaflet behavior in all three cases, each with the two valve orientations. Varying the cardiac output through the same 25mm valve corresponds to the clinical question of valve sizing. The 2 L/min case represents valve oversizing, the 3.5 L/min case represents standard sizing, and the 5 L/min case presents valve undersizing.

The flow fields in the dilated MPA model varied substantially with cardiac output, including differences in jet shape, size and location of recirculation regions, and areas of reversed flow. In the 2 L/min case, the jet through the valve was more asymmetric and the secondary flows were stronger than the other cases. We calculated the valve orifice area using the high-speed imaging experiments. The 5 L/min case had the largest orifice area, indicating the valve was most efficient at this cardiac output.

The valve leaflet behavior over the cycles revealed that at 2 L/min, certain portions of the leaflets remained partially closed throughout systole, blocking flow through the valve orifice. This produced the asymmetry seen in the corresponding flow fields from 4D flow MRI scans in both the native and rotated orientation. This connection

demonstrates how flow features can reveal valve leaflet behavior. Overall, we discovered multiple adverse flow and leaflet features in the 2 L/min case, indicating that valve oversizing may produce a hemodynamic environment that predisposes the valve for failure.

The effects of valve position were examined in two RVOT models with an acute angle between the RV and MPA. In one case, the valve annulus was aligned with the RV. The other case aligned the valve with the MPA. Four 4D flow MRI scans were conducted: the native and rotated orientation for each of the models. Each valve alignment produced a different hemodynamic environment in the models. When the valve was aligned with the MPA in the native orientation, it produced jet impingement on the vessel wall above the bifurcation, though this was largely alleviated in the rotated orientation case. When the valve was aligned with the RV, the flow was characterized by large reversed flow volumes and high secondary flow strength. The jet impacted the MPA vessel wall in this case, with the valve orientation shifting the location of impingement. These studies illustrated the importance of valve position in anatomies with extreme curvature as the global flow features were significantly different in these two cases.

The 4D flow MRI data from the healthy control model with the native orientation were used to validate a design-based mechanistic valve model using the immersed boundary method for fluid-structure interaction simulations. This process demonstrated how the experiments conducted in this work provide high quality data for comparisons with computational results. The simulations successfully captured the jet angle and reversed flow regions present in the experimental data. Further tuning for the simulations is necessary to better match the triangular shape of the jet.

Overall, this work demonstrated that RVOT anatomy, cardiac output, valve orientation, and valve position have a significant impact on the hemodynamics local to bioprosthetic valves in ToF patients. This emphasizes the need for a better clinical understanding of how the hemodynamic environment impacts early valve failure. Ultimately, this research could aid clinicians in determining the optimal pulmonary valve placement for long-term performance on a patient-specific basis, enabling personalized care for ToF patients.

Acknowledgments

The authors would like to acknowledge the funding sources that made this research possible: the Stanford Graduate Fellowship, the Benchmark Capital Fellowship in Congenital Cardiovascular Engineering from the Vera Moulton Will Center for Pulmonary Vascular Disease, the Stanford Bio-X Bowes Fellowship, the Stanford Maternal and Child Health Research Institute, and a Transformational Project Award from the American Heart Association. This project could not have been done without the assistance of the following: Dr. Doff McElhinney, the main clinical collaborator; Dr. Christopher Elkins for running all of the MRI experiments; and Dr. Katsuhide Maeda for allowing observation of multiple pulmonary valve replacement surgeries.

Contents

List of Tables

List of Figures

Nomenclature

Commonly Used Abbreviations

CHD	Congenital heart disease
FSI	Fluid-structure interaction
IB	Immersed boundary
LPA	Left pulmonary artery
LPN	Lumped parameter network
MPA	Main pulmonary artery
MRI	Magnetic resonance imaging
PA	Pulmonary artery
PVR	Pulmonary valve replacement
RPA	Right pulmonary artery
RV	Right ventricle
RVOT	Right ventricular outflow tract
SNR	Signal to noise ratio
ToF	Tetralogy of Fallot

Roman Symbols

A	Cross-sectional area
B_0	Main magnetic field strength
C	Capacitance
I_1	Streamwise flow momentum flux
I_2	Secondary flow strength
L	Length
l	Inductance
P	Pressure
R	Resistance
r	Radius
U_{ref}	Reference velocity
U_{RVOT}	RVOT velocity upstream of the valve at peak systole
u_r	Radial velocity component
u_x	Streamwise (x-component) velocity
V	Volume
$VENC$	Velocity encoding value

Greek Symbols

δ_u	Velocity uncertainty in 4D flow MRI
γ	Gyromagnetic ratio
μ	Dynamic viscosity

ω_0	Larmor frequency
ω_x	Streamwise (x-component) vorticity
ρ	Density

Chapter 1

Introduction

1.1 Background and Motivation

1.1.1 Congenital Heart Disease

Congenital heart disease (CHD) is the most common congenital disorder, occurring in approximately 1 of 125 live births every year. Nearly all CHDs require repair early in the patient's life, with the most severe CHDs necessitating palliative surgery within the first few months after birth. Before the successful development of the cardiopulmonary bypass and other surgical techniques in the 1950s, severe CHD was almost universally fatal (Wu et al., 2020). The surgical procedures that have developed since then allow children with CHD to survive into adulthood, with the overall survival of all CHD patients increasing from 15% in the 1950s to 90% today (Brida and Gatzoulis, 2020). The remarkable success of early surgical repair for CHD and continued development of innovative surgical techniques has led to a rapidly growing population of adult patients with CHD (Gilboa et al., 2016; Hoffman and Kaplan, 2002; Schwartz et al., 2018; Marelli et al., 2007; Ionescu-Ittu et al., 2010; Bouma and Mulder, 2017; Brida and Gatzoulis, 2020; Lui et al., 2014). In fact, in 2010, adults accounted for approximately 66% of the entire CHD population (Marelli et al., 2014).

Patients with CHD are at risk for lifelong comorbidities and often require multiple reinterventions, as early surgical treatment of these diseases is rarely curative (Lui et al., 2014; Bouma and Mulder, 2017; Schwartz et al., 2018). As such, especially with the growing CHD population, there is increasing focus on improving intermediate and long-term care for CHD patients following an initial repair. Various studies have highlighted the improvements in surgical techniques and examined longitudinal data to review the long-term outcomes for CHD patients beyond early childhood (Holst et al., 2017; Martin and Jonas, 2018; Smith et al., 2019). However, there is naturally large variation within the CHD population, as each disease type comes with different defects and requires different forms of repair. Therefore, improvements to the treatment of CHD are typically directed towards specific diseases.

1.1.2 Tetralogy of Fallot

Tetralogy of Fallot (ToF) is the most common cyanotic (characterized by deficient blood oxygenation) CHD, affecting 1 in 2500 live births annually in the United States. ToF patients of all ages account for 7-10% of all cardiac malformations (van Doorn, 2002; Louvelle et al., 2019). ToF is comprised of four different defects: a ventricular septal defect (VSD), an overriding aorta, right ventricular hypertrophy, and right ventricular outflow tract (RVOT) obstruction, often with a stenotic pulmonary valve, as seen in Figure 1.1. ToF was universally fatal until the first palliation was successfully conducted by Blalock and Taussig using a systemic artery to pulmonary shunt in 1945, which extended ToF patient life expectancy from a few months to a few years (Blalock and Taussig, 1984; Holmes, 2012). In 1954, Lillehei performed the first full open-heart repair of ToF, making it a correctable malformation with most of Lillehei's ToF patients surviving into adolescence and adulthood (Lillehei et al., 1955, 1986). In current surgical practice, ToF patients typically undergo surgical repair during the first few months of life. During this initial open-heart surgery, the VSD is closed, which also corrects the overriding aorta, and the RVOT obstruction is relieved, typically with a transannular patch or right ventricle (RV) to pulmonary artery (PA) conduit (Hirsch et al., 2000). Due to the remarkable success of this initial repair surgery, 90% of ToF patients are expected to live beyond 40 years old, which makes ToF the fastest growing CHD patient population (Suleiman et al., 2015; Moons et al., 2010).

Correcting the RVOT obstruction is a crucial part of ToF surgical repair, as it creates an unobstructed path for blood flow from the RV to the lungs. However, widening the RVOT during this surgery typically leaves patients without a fully functioning pulmonary valve and they acquire pulmonary regurgitation or insufficiency (Kogon et al., 2007). Achieving pulmonary competence during the initial repair is difficult and generally unsuccessful, as attempts to construct or insert valves at this stage fail due to structural deterioration and lack of growth (van Doorn, 2002). While the pulmonary regurgitation from the initial surgery can be well-tolerated throughout the early postoperative years, it increases RV volume load and eventually results in progressive RV dilation and dysfunction as the compensatory mechanisms in the right heart break down (Geva, 2011; Suleiman et al., 2015; van Doorn, 2002; Holmes, 2012). Chronic pulmonary regurgitation and RV dysfunction are important risk factors for long-term adverse outcomes, including ventricular arrhythmias and sudden death (van Doorn, 2002; Holmes, 2012; DiLorenzo et al., 2018). Pulmonary regurgitation can be treated with the placement of a competent pulmonary valve, which relieves the RV volume overload and can restore RV function, decreasing the risk of sudden cardiac death (Fuller, 2014). The details of pulmonary valve replacement (PVR) surgery are discussed in depth in Section 1.2.

In addition to complications caused by widening the RVOT, the initial repair of ToF and the ToF defects themselves lead to patient anatomies that are significantly different from a healthy right heart and pulmonary anatomy. Clinical observation also reveals a wide range of RVOT anatomies among the ToF patient population, with significant variations in vessel dilation, radius of curvature, RVOT angle as it extends from the RV, and angle at the first pulmonary artery bifurcation (Schievano et al., 2007). Figure 1.2 illustrates two of the variations seen in the ToF patient population compared to a healthy anatomy, including dilation in the main pulmonary artery (MPA), which is one of the most common variations, and an acute angle of curvature in the RVOT.

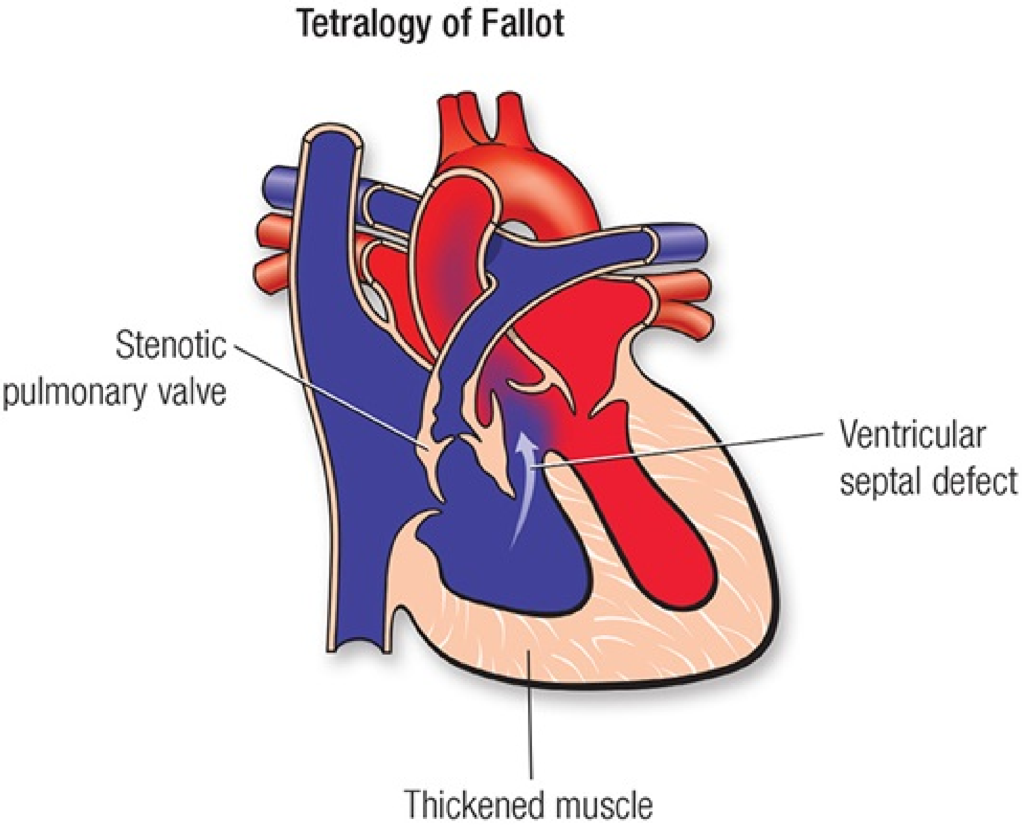

Figure 1.1: Schematic of ToF, which is comprised of four defects: a ventricular septal defect, an overriding aorta, right ventricular hypertrophy, and RVOT obstruction with a stenotic pulmonary valve. The overriding aorta is shown where the light blue arrow indicates blood flow going into the aorta from the right ventricle. Right ventricular hypertrophy results in the thickened muscle around the right ventricle (source: American Heart Association).

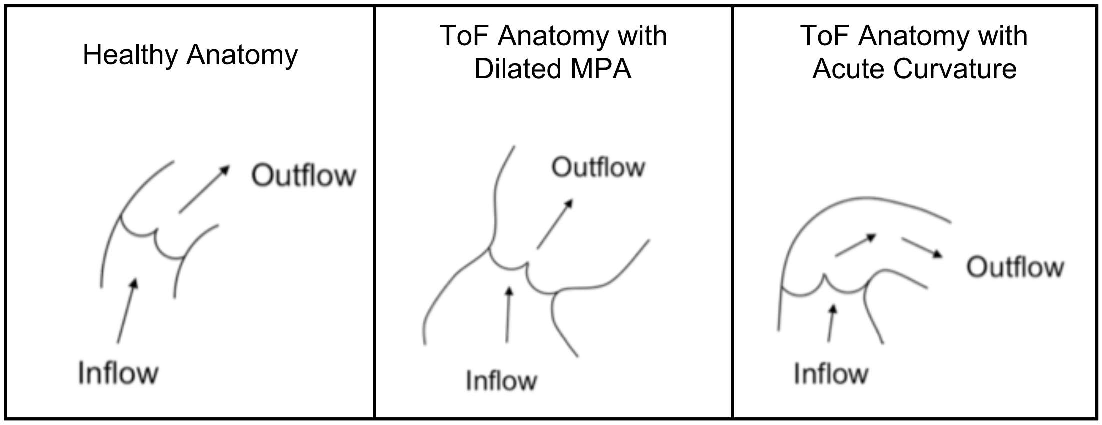

Figure 1.2: Simplified illustrations of a healthy RVOT (left), an RVOT with a dilated MPA (middle), and an RVOT with an acute angle of curvature (right). The middle and right images depict common variations seen in ToF (illustrations provided by Dr. Doff McElhinney).

1.1.3 ToF Geometric Features Associated with Surgical Outcomes

Geometric variations in ToF patients may impact the implementation and success of future reinterventions, including PVR. Studies have found that patient morphology can be associated with both the short-term outcome (Kirklin et al., 1992) and long-term function (Shen et al., 2021) after the initial ToF repair. The recent study by Shen et al. (2021) examined patients with repaired ToF and found that the shape of RVOT was associated with RV volume remodeling and other indicators of poor RV function over 10 years after their initial repair. This study measured a wide range of geometric parameters, but focused on the patient function before their first PVR surgery. Henkens et al. (2007) examined the role of geometry on PVR outcomes by measuring RV size and function before and after the surgery. Their findings indicated that RV end-systolic volume was the best predictor for RV volumes after PVR and should be a key factor in determining the timing of surgery. In another study examining patients with homografts inserted during PVR, the geometry of the homograft itself influenced the likelihood of valve incompetence (Nordmeyer et al., 2009). These studies emphasize the role geometry plays in heart function and outcomes for

ToF patients, but there is limited literature that focuses on PVR specifically while accounting for numerous measurements of RVOT and PA geometry.

In collaboration with clinical colleagues, we examined image data of a cohort of 81 ToF patients to determine associations between pre-operative anatomy and outcomes after PVR surgery (Arana et al., 2021). We measured a wide range of geometric features for each patient, including the lengths of the RVOT, MPA, and branch PAs, the diameters of those segments at various cross-sections, and the angles of the vessels at the RV and at the bifurcation. We also calculated segment volumes, cross-sectional areas and eccentricities, and area ratios along vessel segments based on those measurements. From the vessel diameters, we were able to categorize the patients into six RVOT shape types, based on the definitions of five types provided in a study of RVOT morphology by Schievano et al. (2007) with an additional category for patients who did not fit in the original five types. These shape types group patients by changes in diameter along the RVOT. For example, Type I represents an RVOT that decreases in diameter from the RV to the PA bifurcation, starting with a dilated MPA, while Type III is an RVOT that increases in diameter along its length. While these morphological types are useful for categorizing RVOTs, we found that there were significant variations in eccentricity along the RVOT within each type; the circumferential shape at the cross-sections does not follow the same patterns as the diameters. The bifurcation angles also varied greatly within each shape category. Thus, the RVOT morphology classification based on the variation of vessel diameter along its length oversimplifies the complex geometry, as the eccentricity and angles of the vessel can also have significant impacts on the environment of the pulmonary valve. This highlights the complex nature of the RVOT anatomy in ToF patients.

We also performed a preliminary analysis with this 81 patient cohort to identify associations between the pre-operative geometric features and freedom from valve dysfunction, an important outcome in ToF patients after pulmonary valve replacement. Due to the limited size of the patient cohort, the number of parameters measured for this study was close to the number of patients, with 74 parameters and 81 patients. Therefore, we explored associations between pre-PVR parameters and freedom from valve dysfunction using a conditional inference forest (CIF), a random-forest method that handles time-to-event data and differs from common survival random forest algorithms by avoiding the bias towards variables with many split points (Nasejje et al., 2017). For the final version of the model, we selected 36 parameters out of the 74 total to include the most comprehensive set of parameters while minimizing redundancy. The CIF identified the most important parameters in determining freedom from dysfunction, but we could not use this model alone to evaluate the association since we did not have a testing data set. Therefore, we assessed the top 25% most important parameters using univariable and multivariable Cox proportional hazards regression, with statistical significance defined as $p < 0.05$.

The CIF model ranked the ratio between the surgical pulmonary valve size and the preoperative pulmonary valve annulus and the RVOT and RPA length, both indexed by body surface area, within the top five most important parameters associated with shorter freedom from valve dysfunction (Figure 1.3). Several branch PA parameters were also assigned importance values within the top 25%, with smaller volume left pulmonary arteries (LPA) ($p = 0.018$) and narrowing right pulmonary arteries (RPA) ($p = 0.024$) significantly associated with shorter freedom from valve dysfunction. While there are limitations in this preliminary study, particularly the small cohort size and the use of retrospective data which did not always document the pulmonary valve location sufficiently, the overall findings suggest that the preoperative geometric features of the RVOT and PA bifurcation may be related to valve dysfunction. Further details can be found in Arana et al. (2021).

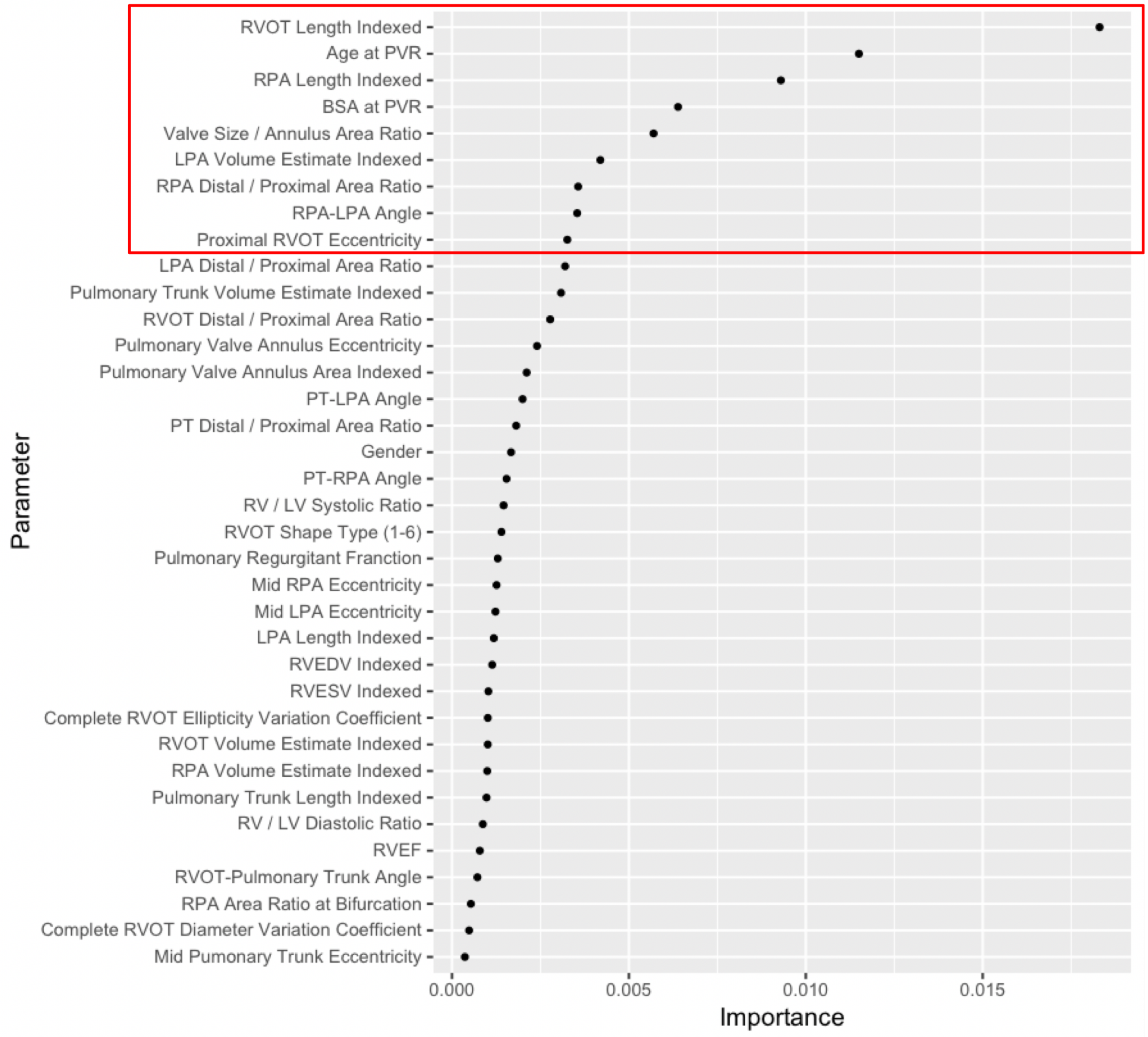

Figure 1.3: Results from the multi-parameter valve function survival analysis using a conditional inference forest model with 10,000 trees evaluating 36 parameters of pre-operative geometric features and patient demographics. The top 25% of parameters (red box) were further evaluated with Cox proportional hazards regression (figure reproduced from Arana et al. (2021)).

1.2 Pulmonary Valve Replacement

1.2.1 Current Surgical Practices

PVR is necessary in most ToF patients to restore pulmonary valve function and eliminate the pulmonary regurgitation created by the initial repair. The indications for when to perform PVR are varied and still debated in the clinical literature (Geva, 2011; Holmes, 2012). For ToF patients with pulmonary regurgitation, the presence of symptoms such as fatigue and decreased exercise tolerance often serves as an indication for PVR surgery (Fuller, 2014). For asymptomatic patients with pulmonary regurgitation from varied causes, the criteria for surgery are not completely standardized. Most recommendations include increased RV volume and a higher fraction of pulmonary regurgitation, though the exact threshold for these values varies (Fuller, 2014; Frigiola et al., 2006; Geva, 2011; Oosterhof et al., 2007; Holmes, 2012). Holmes et al. (2012) note that the decision for PVR timing is a balance between preserving RV function, which indicates operating earlier before dysfunction becomes irreversible, and minimizing the potential number of future interventions, which tends to be higher for patients who undergo PVR earlier. Regardless of these variations in indications for PVR, all studies concur that successful PVR reduces or eliminates pulmonary regurgitation by placing a functioning valve, which in turn allows for RV recovery in volume and function (Gengsakul et al., 2007). For most ToF patients, PVR is performed in late childhood or adolescence, due to the benefits of relieving the chronic pulmonary regurgitation (Kanter et al., 2002; Mitropoulos et al., 2017; Fuller, 2014).

Kogon et al. (2007) provide a detailed description of typical PVR technique. Surgical PVR is an open-heart procedure performed with the patient on cardiopulmonary bypass, conducted with either cold cardioplegic arrest or a beating heart technique depending on the patient-specific defects and anatomy. An incision is made in the MPA and partially into the RV to provide access to the pulmonary valve annulus. Typically, the surgeon will excise any pulmonary valve leaflet tissue left from the native valve. Then the surgeon will use valve sizers to choose the replacement valve size and sew the valve in place along the posterior side into the native MPA vessel. To close the incision, an RVOT patch made of bovine or pericardium is shaped to fit over the incision area. The RVOT patch is sutured to the MPA, then the anterior section of the valve annulus is sewn in, followed by closing the RV end of the incision with the patch.

Xenograft bioprosthetic valves, along with allograft or xenograft valved conduits, are the most commonly used prostheses for RVOT reconstruction in patients with ToF and other forms of congenital heart disease in which PVR is necessary (Kogon et al., 2007; Batlivala et al., 2012; Chen et al., 2012; Babu-Narayan et al., 2014; Zubairi et al., 2011; Lee et al., 2012). In particular, Kogon et al. (2007) note that they prefer to use bovine, porcine, and pericardial bioprosthetic valves for PVR because they are easy to implant, durable in the low-pressure system of the right heart, and have cost and availability advantages. While mechanical valves are more durable than bioprostheses, they require long-term anti-coagulation therapy, which poses high risks in children (Siddiqui et al., 2009). The main disadvantage of bioprosthetic valves, however, is that most are subject to structural degeneration and dysfunction over time, often within 10-15 years of implantation depending on patient age, size, and other factors (McElhinney et al., 2011; Siddiqui et al., 2009; Vongpatanasin et al., 1996).

Bioprosthetic pulmonary valves are placed during surgical PVR, which is still regarded by most as the gold standard procedure for adolescent and adult ToF patients (Suleiman et al., 2015). However, transcatheter pulmonary valves are emerging as an option for PVR. The first transcatheter replacement of a pulmonary valve installed a bovine bioprosthetic valve in an RV to PA conduit with valve dysfunction (Bonhoeffer et al., 2000). This first operation and subsequent trials on larger cohorts of patients have demonstrated the success and safety of using transcatheter valves for PVR (Bonhoeffer et al., 2000; Khambadkone et al., 2005; Lurz et al., 2008). The Melody valve (Medtronic Inc, Minneapolis, Minn), a modified version of the original device used by Bonhoeffer, has been approved by the United States Food and Drug Association (FDA) for use in dysfunctional RVOT conduits and is commercially available throughout the world (McElhinney et al., 2010). McElhinney et al. conducted a multicenter US clinical trial which demonstrated that Melody implants provide pulmonary valve competency, reduce RVOT obstruction, improve RV function, and can be safely placed by experienced interventional cardiologists (McElhinney et al., 2010; Zahn et al., 2009). However, all of these Melody valve studies were conducted in dysfunctional RVOT conduits, which are not placed in all ToF patients, and transcatheter valve use is limited by patient size and RVOT anatomy. Since most ToF patients undergo an initial repair with a transannular patch and are left with a dilated native RVOT, transcatheter techniques generally cannot be used in these situations, which constitutes over 85% of ToF patients who require PVR (Suleiman et al., 2015; Fuller, 2014). Though there is early-stage development for transcatheter valves that can be used in native RVOTs (Cao et al., 2014; Schievano et al., 2010) and techniques for using multiple stents with existing transcatheter valves in large RVOTs (Boudjemline et al., 2012), these options are still far from ready for regular clinical use (Suleiman et al., 2015). Therefore, while transcatheter valves are emerging as an attractive option for treating RVOT obstruction, they are rarely a viable solution for ToF patients undergoing their first PVR.

Valve sizing and position during surgical PVR are often left to the surgeon's discretion. Kogon et al. (2007) note that the size should be chosen such that two thirds of bioprosthetic valve fit within the native pulmonary annulus. However, some surgeons often oversize the valve to allow for somatic growth (Kwak et al., 2016; Maeda et al., 2021). In contrast, some studies have found that valve oversizing may actually contribute to early bioprosthetic valve failure (Wells et al., 2002; Karamlou et al., 2005; Chen et al., 2012). Thus, there are discrepancies in surgical practice for determining valve size during PVR and the effects of valve oversizing are not fully understood. Valve position within the MPA and rotational orientation can be difficult to standardize due to the wide variation in ToF anatomies. It is important to place the valve and its supportive struts in a location that avoids coronary artery compression (McElhinney et al., 2010; Kogon et al., 2007). The valve placement also has to facilitate closure by the RVOT patch. Kogon et al. (2007) make a recommendation to orient the valve such that it aligns with the downstream PAs, but it is not clear if this is possible in all ToF patients. Beyond these considerations and normative dimensions, there are no standard clinical guidelines for valve placement or sizing during PVR surgery.

1.2.2 Early Bioprosthetic Valve Dysfunction

PVR surgeries in ToF patients successfully restore pulmonary valve competency in the early postoperative years. However, bioprosthetic valves are subject to dysfunction over time, which typically presents as pulmonary regurgitation, pulmonary stenosis, or a combination of both (Batlivala et al., 2012; Lee et al., 2016; Nordmeyer et al., 2009). While this eventual dysfunction is expected over a period of 10-15 years, these valves fail early and unpredictably in as many as 30% of ToF patients despite extensive clinical experience with bioprosthetic valves in the RVOT (Oliver et al., 2015; Khanna et al., 2015). Several studies have identified younger age is a predictor of shorter longevity in bioprosthetic valves and valved conduits (Maeda et al., 2021; Chen et al., 2012; Oliver et al., 2015; Batlivala et al., 2012; Kwak et al., 2016; Zubairi et al., 2011; Lee et al., 2011). For young patients, valve failure may be partially a function of somatic growth, as the valve cannot accommodate the increasing cardiac output as a patient grows. Oliver et al. (2015) found that when the patient was older that 20.5 years at the time of PVR, freedom from reintervention for pulmonary valve failure at 15 years was 70%. When the patient was younger than 20.5 years, the freedom from reintervention dropped to 33%. Chen et al. (2012) identified a similar cut-off point with patients younger than 20 years at PVR having increased risk of structural valve deterioration. Even within a cohort where all patients were under 21 years at PVR, younger age was still found to be associated with shorter freedom from reintervention (Batlivala et al., 2012). This repeated finding highlights the risk of early valve dysfunction in the ToF patient population, who typically undergo PVR during adolescence. Bioprosthetic valve degeneration and dysfunction, and the reinterventions necessary to replace them, are important causes of morbidity in these patients. Thus, extending long-term valve function is crucial in improving overall outcomes for ToF patients who undergo PVR.

There are various modes of valve failure that lead to dysfunction, including calcification, valve leaflet tears, and pannus growth (Siddiqui et al., 2009; Konakci et al., 2005; Schoen et al., 1987; Butany and Leask, 2001). Calcification is the most common mode of valve degeneration; it can produce regurgitation or stenosis and is also considered a predisposing factor in leaflet tears. Calcific deposits can begin to form within 3 years of valve implantation and the most common sites are the commissures and the basal area of the leaflets, which is where the leaflets meet the annulus. Calcific leaflets are prone to tearing, which then leads to regurgitation through the damaged leaflet. Alternatively, these calcific leaflets can stiffen and prevent full motion, leading to pulmonary stenosis. Calcification may be caused by several possible factors, including immune system response, chemical interaction in the blood, and mechanical stress (Siddiqui et al., 2009; Schoen and Levy, 1999; Liao et al., 2008). Additionally, immunologic factors may contribute to other modes of dysfunction when valved homograft conduits are placed during PVR (Christenson et al., 2004; Baskett et al., 2003). In addition to calcification, bioprosthetic valve failure can be caused by leaflet tears and pannus, which is the growth of the patient native tissue onto the implanted valve. Leaflet tears can be generated directly by high pressures during opening and closing periods and are commonly seen at the commissures, where the stress is highest (Siddiqui et al., 2009). Some pannus is expected as part of the natural healing process after PVR, but when pannus extends onto the valve leaflets, it can lead to thickening that stiffens the leaflets and fixes them in place, which in turn causes stenosis (Siddiqui et al., 2009). Valve degeneration and failure can also be caused by rarer modes, such as infective endocarditis or valve thrombosis.

The complex hemodynamics and blood flow patterns produced by bioprosthetic valves can play a significant role in producing these failure modes and in their overall function. Several overview studies provide an in-depth description of the fluid dynamics of native pulmonary valves, which involve a high-speed jet through the valve opening together with small regions of reverse flow during later systole (Sacks and Yoganathan, 2007; Sacks et al., 2009). Similar fluid dynamics reviews of prosthetic valves demonstrate their impact on hemodynamics in producing flow patterns not seen in native heart valves (Yoganathan et al., 2004, 2005; Sotiropoulos et al., 2016;

Dasi et al., 2009). Prosthetic valves are shown to produce regions with higher velocity and higher turbulent shear stress than native valves, along with flow instabilities and large recirculation regions outside of the jet (Yoganathan et al., 2005; Dasi et al., 2009). These complex hemodynamic features have been linked to clinical complications, such as increased fluid stresses that induce leaflet calcification or tearing and affect red blood cells and endothelial cells (Yoganathan et al., 2005; Dasi et al., 2009; Sotiropoulos et al., 2016; Raghav et al., 2018; Nordmeyer et al., 2009). Reversed flow is a key feature for valve performance as some literature suggests some reversed flow enables more efficient valve closure, but other studies indicate that too much reversed flow produces regions where hemolysis and hemostasis can occur (Yoganathan et al., 2005; Sotiropoulos et al., 2016). Regions of flow stagnation and flow separation in the vicinity of the valve have also been linked to tissue overgrowth and calcification (Yoganathan et al., 2004). Overall, these studies demonstrate that bioprosthetic heart valve hemodynamics can have a significant impact on long-term valve function.

The blood flow patterns local to bioprosthetic valves are not only created by the valves themselves, but also by the surrounding anatomy. Sotiropoulous et al. (2016) found that bioprosthetic valves generate complex flow structures and vortex rings that interact with the surrounding cardiac anatomy to generate shear layers and regions of recirculation. They noted that the location and orientation of prosthetic heart valves during implantation, in addition to the geometry of the valves, have an important role in the resulting hemodynamics. The relationship between geometric features and hemodynamics has been extensively studied in other cardiovascular environments, such as the carotid artery bifurcation and stenotic coronary arteries, revealing key relationships between geometry and clinical outcomes (Lee et al., 2008; Niu et al., 2018; Bressloff, 2007; Morbiducci et al., 2016; Peng et al., 2016; Cheung et al., 2010; Manbachi et al., 2011; Nguyen et al., 2008). On the pulmonary side, examinations of healthy PA bifurcations have demonstrated complex three-dimensional flows, including swirling flow in the LPA and RPA, that vary with patient-specific anatomy and with resting versus exercise conditions (Tang et al., 2011; Capuano et al., 2019).

In the ToF patient population, the influence of geometric features on hemodynamics is particularly crucial due to the wide range of anatomic variations. After initial repair, geometric complexity in ToF, such as bifurcation angles and vessel diameters and tortuosities, can impact flow separation, recirculation, and regurgitation and reverse flow in the MPA and branch PAs (Louvelle et al., 2019; Zhang et al., 2016; Chern et al., 2012, 2008). PVR procedures introduce additional geometric complexity and variations in ToF patients, which can alter the hemodynamic and biomechanical characteristics of the right heart compared to normal anatomies, leading to adverse effects on RV function (DiLorenzo et al., 2018; Lee et al., 2013; Das et al., 2010; van Straten et al., 2004).

These previous studies provide a wealth of knowledge on the hemodynamics of native and prosthetic pulmonary valves, the role hemodynamics can play in valve function, and the relationship between geometric features and flow characteristics in ToF. However, there has only been limited work examining the role of specific anatomic variations or the impact of valve placement during surgery, particularly in the pulmonary position (Schievano et al., 2011; Biglino et al., 2013b; Vismara et al., 2009; Louvelle et al., 2019). In general, PVR outcomes in ToF patients remain poorly understood. While modes of valve failure have been identified, the anatomic and hemodynamic factors that contribute to the degeneration and dysfunction of bioprosthetic valves in the RVOT reamin poorly understood. Though studies have identified younger age as one risk factor for early valve dysfunction, within this younger cohort it is currently not possible to predict which patients will experience earlier valve dysfunction. Thus, it remains unknown why the trajectory of bioprosthetic valve failure varies so extensively in the RVOT. At present, there are no surgical or clinical measures proven to extend bioprosthetic pulmonary valve longevity.

1.3 Present Work

The objectives of this project were to discover how patient-specific features such as RVOT anatomy, cardiac output (particularly relative to bioprosthetic valve size), valve orientation, and valve position within the RVOT impact the hemodynamics local to the valve placed during PVR in ToF patients. We believe that the flow features generated by these parameters will impact the environment of the valve and its long-term performance. In particular, we wanted to analyze full three-dimensional (3D), three-component velocity fields over the cardiac cycle in models that accurately represented typical ToF anatomies and surgical valve behavior. To accomplish this goal, we chose to design and examine experimental models using 4D flow magnetic resonance imaging (MRI), which is also called magnetic resonance velocimetry (MRV). The specific objectives of this work are:

- Design and print anatomical models of the RVOT which allow for surgical valve placement and represent key variations seen in the ToF patient population.
- Develop an MRI-compatible physiological flow loop which can accurately capture pulmonary pressure and flows. The flow loop should be reusable for all RVOT models.
- Analyze full 3D, three-component flow fields over the cardiac cycle for a variety of ToF anatomies and valve positions that would be considered during surgical PVR.
- Characterize the hemodynamic differences between healthy and diseased geometries, between different valve orientations or placements within those geometries, and between varied cardiac outputs.
- Validate a novel simulation technique for flow through valves in realistic anatomical models and demonstrate use of experimental data as a gold standard for validating valve leaflet simulation methods.

Chapter 2 describes our methodology in detail. There are many benefits to using 4D flow MRI for this project. It does not require optical access to measure velocity fields, allowing us to 3D print complex opaque models that capture key anatomical features of the RVOT anatomy. This *in vitro* study enables us to change valve position, orientation, and cardiac output with the same geometry, which is not possible *in vivo*. While 4D flow MRI is the same technique that is used *in vivo*, longer scan times are possible with experimental phantoms which leads to better spatial resolution in the data. Though the rigid printed models do not represent anatomical material properties, they facilitate the scan procedure, providing greater consistency in measurement resolution and uncertainty between cases. Critically, this experimental project is designed to use clinical surgical valves, guaranteeing that we are capturing true valve leaflet dynamics. Computational methods are limited in this capacity due to the difficulty of accurately simulating valve leaflets along with fluid flow and the surrounding anatomy.

A series of experiments were carefully designed to test various aspects of patient variability and valve hemodynamics. Four different modular ToF anatomy models were printed: a healthy control, a disease case with a dilated MPA, and two diseased cases for different valve placements within an RVOT and MPA with acute curvature. Two different valve orientations were analyzed for all four models and three different cardiac outputs were studied in the dilated MPA model. 4D flow MRI experiments were conducted for all of these cases. Additionally, high-speed video was used to capture instantaneous leaflet motion for selected configurations.

Chapter 3 compares the flow fields of the healthy control model to the dilated MPA model, each with two valve orientations. We illustrate the qualitative and quantitative differences in key flow features between the two cases. In particular, we demonstrate the compound impacts of changing both RVOT anatomy and bioprosthetic valve orientation.

Chapter 4 examines the effect of changing cardiac output in the dilated MPA model. We employ both 4D flow MRI and high-speed video experiments to study the differences in the hemodynamics throughout the model and the instantaneous behavior of the valve leaflets.

Chapter 5 analyzes the two models that represent an RVOT with an acute angle. Clinically, surgeons presented with this anatomy often have to make a choice on whether to align the valve with the RV or with the downstream PA. We analyze these choices with two different models based on the same curved anatomy and examine how the valve position and orientation change the overall hemodynamics.

In Chapter 6, we use the experimental data from the healthy control model to validate a novel simulation method. This preliminary work demonstrates the capabilities of this method, which utilizes an immersed boundary method and a mechanistic valve model to capture realistic valve leaflet motion. This work also illustrates how the data collected during this project can be used as a gold standard for validating valve simulations.

Finally, Chapter 7 presents conclusions and suggests future research. We discuss the learnings from our experimental models and the potential for linking hemodynamic features to clinical outcomes in ToF patients.

Chapter 2

Experimental Methodology

2.1 4D Flow Magnetic Resonance Imaging

The experiments in this study utilize 4D flow magnetic resonance imaging (MRI), also called 4D phase contrast MRI or magnetic resonance velocimetry, to obtain full 3D, three-component, phase-averaged velocity fields in physical models of the RVOT. This section summarizes the basic principles of MRI and describes how velocity data are generated over the cardiac cycle using 4D flow MRI sequences. Detailed reviews of the development and use of these methods in analyzing fluid dynamics problems is provided by Elkins et al. (2003) and Elkins and Alley (2007).

2.1.1 Principles of MRI

MRI utilizes the resonant properties of hydrogen protons in water molecules when subject to an applied magnetic field. The hydrogen protons precess around the strong magnetic field, called B_0, at a rate called the Larmor frequency, defined as

$$\omega_0 = \gamma B_0 \,, \tag{2.1}$$

where γ is the gyromagnetic ratio, a material property of the resonant species. The gyromagnetic ratio of hydrogen is 42.58 MHz/T and all studies in this work were conducted in a magnet with a field strength of 3T. To generate signal, a radiofrequency (RF) pulse tips the hydrogen proton spins out of alignment with the main magnetic field. The spins relax after the pulse is provided, still precessing around the applied magnetic field. The RF signal produced by the relaxing spins is measured by receiving coils in the MRI scanner. In addition to the static B_0 field, weak magnetic field gradients are applied along the three physical axes of the magnet. This allows spatial information to be encoded in the acquired signal, since the frequency of the spins is directly proportional to the external magnetic field.

In 4D flow MRI, velocity information is obtained using the phase of the MR signal. In a static, uniform magnetic field, the phase of stationary and moving spins, subject to an RF pulse, would be the same since they would precess at the same frequency. To encode velocity information, a magnetic field gradient is applied in the direction of the desired velocity component. A spin moving in this field will be subject to spatially varying magnetic field strength, which results in varying precession frequency. The phase of the signal for each spin reflects this varying precession frequency, which was caused by the movement of the spin, thereby encoding velocity information. When these magnetic field gradients are applied in all three principle directions, the MRI data produces three-component velocity fields.

While applying magnetic field gradients allows velocity information to be encoded in the signal phase, the initial position of a spin can also be encoded in the phase depending on how the gradients are applied. To avoid this, scanning sequences in velocity encoding typically use a bipolar pair of magnetic field gradients. This pair has equal positive and negative lobes to produce a gradient signal with zero mean magnetization over time. This eliminates the effect of the initial spin position. In addition, the signal phase can be dependent on other sources, such as B_0 or RF inhomogeneity, susceptibility differences, and off-resonance effects (Pelc, 1995). To eliminate these other dependencies, two acquisitions of phase signal are used for each component of velocity. Each of the phase acquisitions is produced from the same underlying velocity field and experiences the same B_0 inhomogeneity and other static properties that may effect phase. The phase information that is only sensitive to velocity is calculated by taking the difference of these two acquisitions. This procedure is called phase contrast imaging. Further details of the scanning sequence and the timing of the applied magnetic field gradients for the data acquisition done in this work are described in Pelc et al. (1994) and Elkins et al. (2003).

The velocities that can be measured in a given phase contrast scan are limited by the range of the phase differences, which is $[-\pi, \pi]$ radians. The maximum velocity produces a phase shift of π radians and is known as the velocity encoding value, or VENC. The VENC is typically set to be slightly higher than a user estimate of the largest expected velocity in a given study. The magnitude of the applied magnetic field gradients are then set such that the range of velocities [-VENC,VENC] are represented by the range of phase differences.

The expected uncertainty of 4D flow MRI velocity measurements is given by

$$\delta_u = \frac{\sqrt{2}}{\pi}\frac{\mathrm{VENC}}{\mathrm{SNR}}\,, \tag{2.2}$$

where SNR is the signal to noise ratio. For the experiments in this work, the signal to noise ratio was calculated as the ratio of the signal in the flow region to the signal in the solid wall, as done in Banko et al. (2015). The signal in the flow region was averaged over a region of interest in the free stream flow. The solid wall of the model within the domain was identified using a threshold for signal magnitude. The signal of the wall was averaged over the voxels denoted by this threshold. The uncertainty is calculated individually for each case and presented with the data analysis in the later chapters.

The MRI sequence for measuring flow can be gated in order to measure pulsatile time-varying flows. The trigger signal that indicates the start of each cardiac cycle is recorded by the MRI along with the velocity data. The data are then sorted into a specified number of time bins, or phases, during the acquisition. Over the acquisition process, the velocity data are averaged within each phase. Note that for 4D flow MRI scans, the VENC must be set high enough to prevent velocity aliasing during phases with high velocity flow, but still low enough to allow for sufficient resolution at low velocities. This 4D flow MRI procedure results in time-resolved, three-component, phase-averaged velocity data over the 3D volume encompassing the test section for each study.

2.1.2 Scan Procedure

The experiments were performed in a whole body, 3 Tesla General Electric MRI scanner at the Richard M. Lucas Center for Imaging at Stanford University. The flow loop, as described in Section 2.3, was assembled in the magnet room with the test section passing through the bore of the magnet for each session (Figure 2.1). For each study, multiple 4D flow MRI scans were conducted and averaged to increase signal strength and reduce noise. Additionally, scans were conducted both with the pump on and with the pump off. The scans with the pump off were taken when the flow had completely come to rest. These pump-off scans were averaged and subtracted from the pump-on scans to reduce various sources of error, including eddy current effects (Elkins and Alley, 2007). To account for drift in the eddy currents and other signal properties, pump-on and pump-off scans were alternated. Only the pump-off scans taken immediately before and after each pump-on scan was used for the subtraction for that particular scan. All of the pump-on scans, with the pump-off data already subtracted, were then averaged to comprise the final data set. Four pump-on scans and three pump-off scans were taken for each case in this work, with each individual scan taking approximately 20 minutes to run.

The scanning sequence for all cases was *mm4dflow*, developed by Christopher Elkins and Marcus Alley. The acquisition was extended dynamic range with gating, with a temporal resolution of 0.077s resulting in 10-11 measured phases. The velocity data were interpolated during reconstruction to provide 20 phases over the cardiac cycle. The spatial resolution was 0.9mm in all three directions. During data acquisition, the x and y corners of the domain were cut off to decrease scan time. Additional scan parameters for most of the cases in this work are detailed in Table 2.1. The field of view (FOV) values, echo time (TE), and repetition time (TR) were varied for the cases discussed in Chapter 5 and their values are noted there.

Figure 2.1: Experimental flow loop setup on the MRI magnet table in the Richard M. Lucas Center for Imaging at Stanford University.

Scan Parameter	Value
Slice Direction	Sagittal
Frequency FOV	16.0cm
Phase FOV	0.6
Slice Thickness	0.9mm
Number of Slices	88
Imagining Matrix	178x178
Flip Angle	15 degrees
Bandwidth	62.5kHz
TE	1502 microseconds
TR	3952 microseconds
Views per Segment	5
Gating Setting	ECG II Inverted

Table 2.1: 4D flow MRI scan parameters

2.1.3 Advantages and Limitations of 4D Flow MRI

Using 4D flow MRI to acquire the velocity data for the studies in this work has numerous benefits. MRI captures the full mean velocity fields throughout the domain without the need for optical access that is required by other methods, such as particle image velocimetry (PIV). This allows interrogation of complex geometries that are 3D printed with non-transparent materials. Thus, we were able to design and print our geometries based on clinical insight and anatomic accuracy, without being limited by our experimental method.

The 4D flow MRI method provides three-component velocity fields on a Cartesian grid over the entire 3D domain, which facilitates direct comparison to computational data as explored in Chapter 6. In addition, our sequence is nearly identical to those used in clinical scans, allowing for future comparison to *in vivo* data. Phase-locked MRI is being used increasingly in various clinical contexts for assessing flow behavior (Stankovic et al., 2014; Lawley et al., 2017; Bächler et al., 2013; Reiter et al., 2008; Barker et al., 2015; Hess et al., 2013; Schäfer et al., 2018). Experimental 4D flow MRI scans can also be completed in one day. For this work, we typically conducted two cases in each session with each case requiring approximately 4 hours of scan time and an additional 4 hours needed for setup and break down in the magnet room as well as transitioning between cases.

Limitations of 4D flow MRI must also be considered. The conventional 4D flow MRI technique is limited to measuring mean velocity fields and thus it cannot provide instantaneous flow behavior. The 4D flow MRI sequence also presents tradeoffs between spatial resolution, temporal resolution, and scan time, with higher resolutions resulting in longer scans. While studying experimental models allows for more flexibility in scan time than *in vivo* settings, the spatial and temporal resolutions of 4D flow MRI data are typically lower than PIV data. However, comparison studies have described the quantitative similarities between 4D flow MRI and PIV data, despite the differences in resolutions between the two techniques (Medero et al., 2018, 2020). Measurements from 4D flow MRI also have limitations near solid surfaces, as voxels at the boundary may contain both the fluid and the solid surface. The signal in such voxels is decreased and the data there cannot be reliably used to calculate quantitative metrics that are used commonly in computational studies, such as wall shear stress.

There are also challenges in experimental design, due to the strong magnetic fields present in MRI. All components that will be placed in the bore or close to the magnet cannot contain any ferromagnetic material, as that can damage the MRI equipment and be dangerous for those operating the scanner. The test section must also be free of all metals and any other materials that may cause artifacts in the MRI data. Thus, the vast majority of the components used in these experiments are plastic or nylon, with the necessary metal components kept far away from the magnet.

2.2 RVOT Geometry Design

The anatomic models used in this work were designed to analyze the flow fields local to bioprosthetic valves in healthy and various diseased ToF anatomies. Each model extends from the outlet of the RV to the left and right branches of the PAs after the first bifurcation. The same 25mm St. Jude Medical Epic valve was used for all cases. It is a porcine trileaflet surgical valve with support scaffolding at the commissures and a sewing ring that is used to suture the valve to the RVOT vessel in the patient (Figure 2.2).

The base model design is modular to allow for adjustments in overall geometry and valve placement. Each model consists of three components: the RV, the valve-holder, and the downstream MPA, LPA, and RPA. The details of the RV component are discussed in Section 2.3.3 due to its role in driving the experimental flow loop. The valve-holder is a two-piece component with a groove that matches the dimensions of the sewing ring on the 25mm St. Jude valve. This groove is clamped around the sewing ring with the two pieces screwed together to secure the valve, as shown in Figure 2.4b. The valve-holder can rotate independently of the other components, allowing for experiments to be run with the valve in different rotational orientations. The downstream component was designed individually for each case to represent a different healthy or ToF anatomy.

Figure 2.2: The St. Jude Medical Epic Valve, which is produced by Abbott (source: Abbott).

The entire model design process was supervised by Dr. Doff McElhinney, a pediatric interventional cardiologist at Stanford Hospital. The individual components and the overall geometry for every case were carefully reviewed and approved by Dr. McElhinney to ensure they accurately represent clinical scenarios. The models were designed in SolidWorks (Waltham, MA) and were manufactured using stereolithography (SLA) with DSM Somos WaterShed XC 11122 resin at the W.M. Keck Center at the University of Texas, El Paso. All components of models and the valve itself are fully MR compatible.

2.2.1 Healthy Control Model

A model of a healthy patient without ToF was designed as a control model and as a baseline for designing the diseased anatomies and comparing the results that will be discussed in the subsequent chapters. The healthy control model is based on measurements made from MRI data of the right heart and PAs of six healthy subjects between ages 11 and 13, the typical age range for the first PVR surgery in ToF patients. MRI data were collected for clinical purposes and used for modeling under an IRB-approved protocol. For each patient, we measured the diameters of

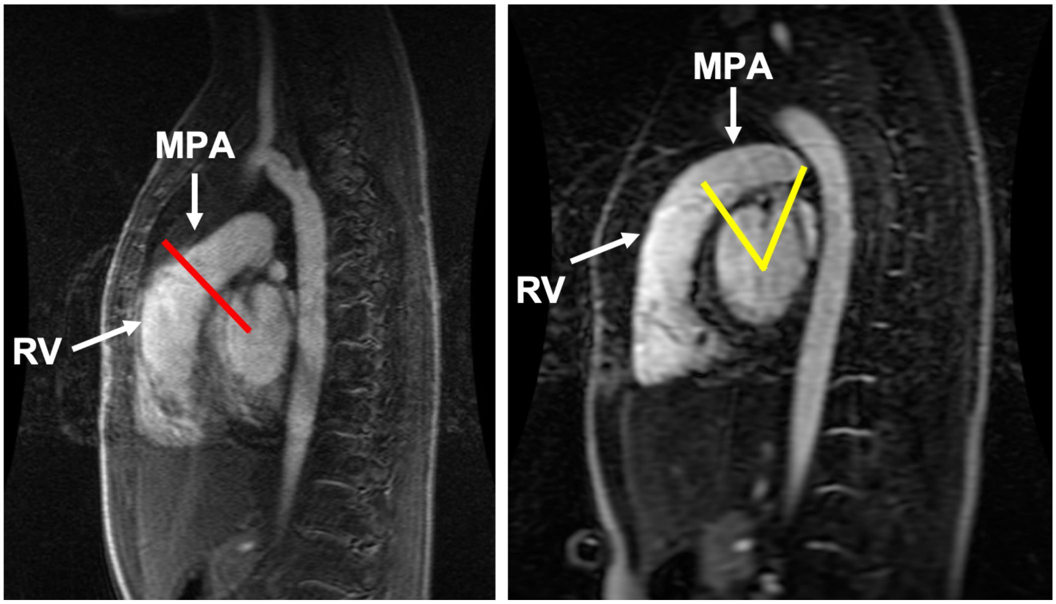

Figure 2.3: Sagittal slices of MRI data from healthy patients used to design the control model. The RV and MPA are labeled on each image. The image on the left has a red line indicating the location of the valve annulus where measurements were taken, and the image on the right shows two yellow lines demonstrating the measurement of MPA radius of curvature.

the MPA, LPA, and RPA in the sagittal and axial planes. The MPA measurement location was at the valve annulus while the locations for the LPA and RPA were immediately downstream of the bifurcation.

In a sagittal plane approximately through the center of the RVOT, we measured the turning angle, radius of curvature, and arc length of the RV outlet to the MPA and of the MPA from the valve annulus to the bifurcation. Figure 2.3 shows examples of the valve annulus located on the MRI data (performed by Dr. McElhinney) and of the radius of curvature measurements for the MPA. We also measured the turning angle, radius of curvature, and arc length of the MPA in an axial slice cutting through the vessel and the bifurcation. The other key parameters were the three angles at the bifurcation: LPA to RPA, MPA to LPA, and MPA to RPA. Measurements were done in ImageJ (Bethesda, MD).

Median values for all subjects of the diameters, lengths, radii of curvature, and

Parameter	Model Value (mm)
MPA Diameter	25
LPA Diameter	12
RPA Diameter	14
Centerline Length from Annulus to LPA Outlet	62.2
RV Radius of Curvature - Sagittal	49.6
MPA Radius of Curvature - Sagittal	41
MPA Radius of Curvature - Axial	38
LPA to RPA Bifurcation Angle	108 degrees
MPA to LPA Bifurcation Angle	116 degrees
MPA to RPA Bifurcation Angle	129 degrees

Table 2.2: Healthy control model dimensions

bifurcation angles were used to construct the healthy control model. Median values were chosen to reduce the effect of outliers in the patient measurements, though differences between median and mean were generally small. The model design was scaled to fit the 25mm bioprosthetic valve, resulting in an MPA diameter of 25mm, LPA diameter of 12mm, and RPA diameter of 14mm. All scaled values fell within the range of measured values from the patient cohort, resulting in a scaled model that accurately represented the 11 to 13 year-old patient population. The key design dimensions for the healthy control model are summarized in Table 2.2. The printed healthy control model is shown in Figure 2.4a, with the RV, valve-holder, and downstream components fully assembled.

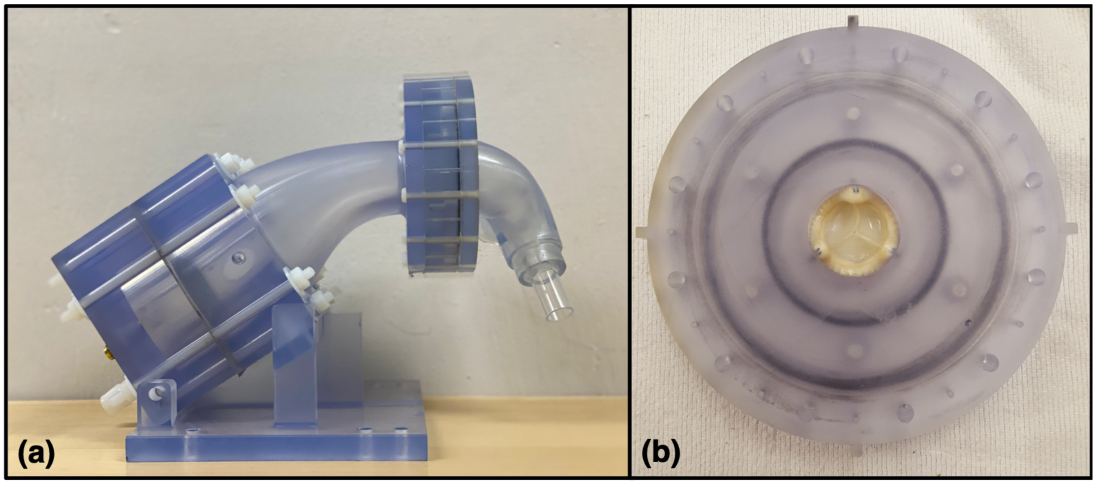

Figure 2.4: 3D printed healthy control model in full assembly (a) and with the valve clamped in the valve-holder component (b)

2.3 Physiological Flow Loop

It is necessary to develop a flow loop that replicates physiological conditions in order for *in vitro* studies to provide clinically relevant results. We developed an experimental setup that reasonably matches the flow rate and pressure values and waveforms over the cardiac cycle for the pediatric pulmonary system. We wanted the entire flow loop, including the 3D printed RVOT models, to be modular so that flow rate, left and right flow balance, valve position, valve orientation, and downstream vessel geometry could be easily adjusted within the same experiment to match typical clinical values.

In this section, we summarize our initial experimental design and describe the changes that were made to achieve reasonable flow rates and pressures within our system. We provide extensive detail on the final flow loop design and illustrate how different components can be tuned to allow for experiments with different cardiac outputs or other clinical parameters while still matching physiological values.

2.3.1 Working Fluid

The working fluid for all experiments was a blood analog consisting of 60% water and 40% glycerin, with a density of 1.1 g/cm^3 and a viscosity of 3.9 centipoise at room temperature in the magnet room. Gadolinium was added to the blood-analog fluid to increase the signal contrast during the 4D flow MRI scan. The fluid was filtered before each experiment to remove debris.

The density and viscosity of the fluid were measured for each experiment. The density was calculated by weighing a 2 liter volume, measured in a graduated cylinder, of the working fluid and dividing the weight by the volume. The viscosity was measured using a glass viscometer. The viscometer was charged with the working fluid using a vacuum pump and the efflux time for the fluid to drain from the test section of the viscometer was measured. The efflux time multiplied by the fluid density and given viscometer constant yields the viscosity of the fluid. Occasionally, the density and viscosity would increase slightly between experiments, due to the fluid laying in storage over time. In these cases, water was added to return the fluid to the original values, so that the working fluid had the same properties for all experiments.

2.3.2 Initial Experimental Design

In our initial experiment design, we produced pulsatile flow using a cylindrical piston pump. This pump was programmable, allowing us to input any initial flow waveform and adjust the heart rate, flow rate, and percentage of the cycle experiencing forward flow. We used a physiological waveform for pulmonary blood flow in healthy patients to drive the pump (Cheng et al., 2005). However, the cylindrical piston pump included ferromagnetic components, so it had to be located approximately 12 feet from the magnet to avoid damage to the equipment and artifacts in the data collected. To accommodate this distance, we ran 1 inch diameter, semi-flexible tubing from the cylindrical piston pump to a 2 inch diameter rigid tube that sat on the magnet table and fed into the original RVOT model. This rigid tube was approximately 3 feet long and connected to a 3D printed component representing the RV outlet, which in turn was connected to the valve-holder and downstream PA anatomy.

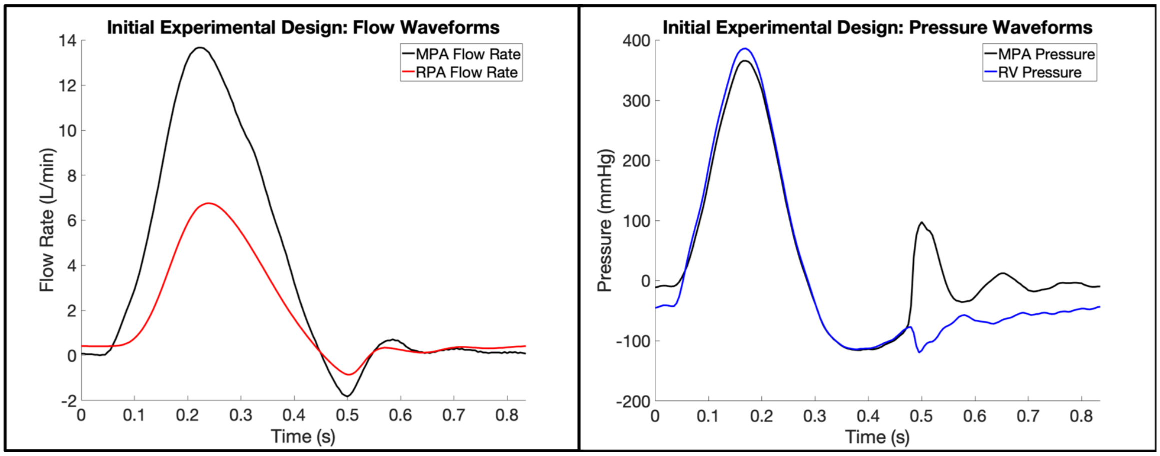

Figure 2.5: Flow rate (left) and pressure (right) waveforms for our initial experimental flow loop design. The MPA and RPA flow rate waveforms are realistic, but the RV and MPA pressures are much higher than physiological values.

With this flow loop, we were able to achieve our target cardiac output and observe the valve opening and closing. Specific details on our targets for physiological flows and pressures are discussed in Section 2.3.5. The flow rate waveforms had generally the correct shape and values. However, the pressure in this initial system was drastically outside of physiological values, with peak systolic pressures nearing 400 mmHg when they should be 30 mmHg (Figure 2.5). We determined that these high pressures were due to a water hammer effect. Since the cylindrical piston pump had to be distanced from the magnet, we were pulsing all of the fluid between the pump and RVOT model. We concluded that in order to achieve physiological pressures, we had to initiate the pulsatile flow much closer to the model. This led to our design of a pneumatic right ventricle, which became our final flow loop setup after iteration on various components.

2.3.3 Pneumatic Right Ventricle Model

We developed an MRI compatible RV model so that the mechanism driving the pulsatile flow could be inside the magnet bore, thus eliminating the need to pulse the large volume of fluid which led to the water hammer effect. The custom designed ventricle box was inspired by pulsatile ventricular assist devices, such as the Berlin Heart

EXCOR (The Woodlands, TX). The ventricle box is a two-component piece. The RV is modeled as a cylindrical cavity within a 101.6mm by 101.6mm by 107.95mm box separated in the center by a thin silicone rubber membrane (0.01 inches thick). One half of the ventricle box contains the working fluid with a 27mm trileaflet bioprosthetic valve at the inlet, acting as the tricuspid valve, and an exit that contracts from 72.6mm diameter to 25mm diameter, which models the RVOT and connects to the valve-holder.

The other half of the ventricle box is an air chamber supplied with pulsatile pressurized air. This air supply is controlled by a programmable proportional pressure regulating valve (Parker Hoerbiger Origa, Richland, MI; model PS120006-020-035) and a binary solenoid valve. A constant air pressure source is fed through the programmable valve that outputs the air as a sine squared wave. This pulsatile air supply pushes the membrane in the ventricle box to create systole and diastole. The solenoid valve provides venting from the ventricle box to replicate the relaxation of the RV during diastole. The digital trigger signal governing the pneumatic ventricle box, thus producing the pulsatile flow, was connected to the ECG converter and trigger on the MRI system to signal the start of each cardiac cycle, allowing us to collect gated phase-locked data. The amplitude, frequency, and duration of the air supply sine squared wave, as well as the timing of the venting during the cardiac cycle, are all tunable parameters. Changing these parameters allows us to achieve a range of cardiac outputs and gives us control over the shape of the pressure waveform to reach nearly physiological conditions.

The ventricle box is one of the 3D printed components of the RVOT model. The close connection between the pneumatic system and the RVOT model greatly improved our control over the flow rate and pressure waveforms. This box is the key component that drives the full flow loop to replicate right heart circulation and pulmonary physiology, shown in the schematic in Figure 2.6. The flow loop also includes an upstream inlet tank fed by a steady centrifugal pump from a supply reservoir. This connects to a flexible bag that acts as a right atrium. The centrifugal pump contains ferromagnetic components and must remain 12 feet away from the magnet. However, the role of the pump is simply to keep the inlet tank supplied, so

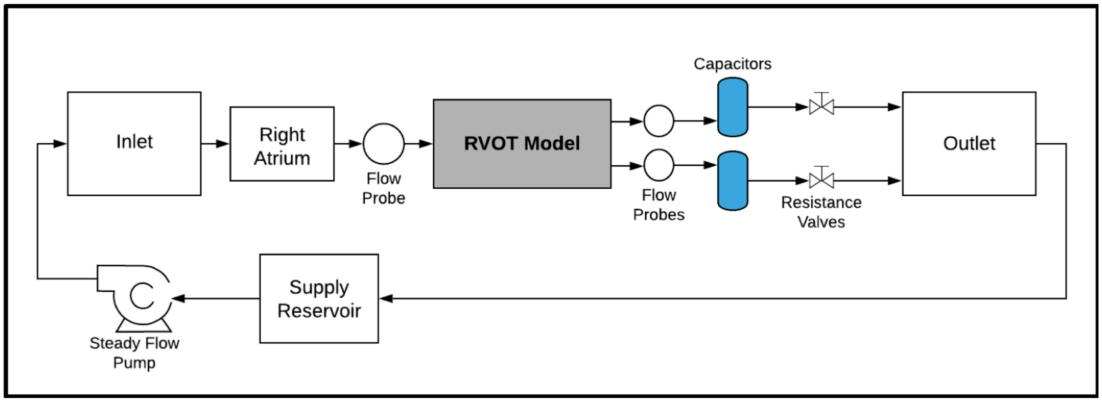

Figure 2.6: Schematic of the experimental flow loop.

the large amount of water moving steadily through the tubing connecting the pump and the tank does not affect the RVOT model itself. The atrium proxy feeds the ventricle box through the 27mm bioprosthetic tricuspid valve.

2.3.4 Downstream Flow Loop Elements

The flow loop elements downstream of the printed RVOT were a major source of iteration in order to produce physiological flow and pressure waveforms. In our design of these components, we drew on the experience of Professor R. Figliola (Clemson University, SC) and collaborators, who have developed a successful system of physical resistance and capacitance elements that can accurately capture a variety of cardiovascular conditions (Figliola et al., 2010; Gohean et al., 2006; Biglino et al., 2013a; Camp et al., 2007; Hang et al., 2016; Vukicevic et al., 2014). Similar concepts were utilized in our flow loop.

The outlets of the model connect to flexible tubing, which in turn connect to capacitor elements. The capacitor elements exit into another segment of flexible tubing which runs to the outlet tank of the flow loop. The two segments of flexible tubing and the capacitor on each outlet branch replicate a resistor-capacitor-resistor Windkessel model that can be tuned to change the outlet boundary conditions for the test section. These elements are the building blocks of lumped parameter networks (LPN), which leverage electric circuit analogies to represent flow loops. LPNs have been used in a wide variety of clinical studies to provide low-order models for *in vitro* and *in vivo* studies (Kung and Taylor, 2011; Kung et al., 2011a,b; Migliavacca et al., 2001; Shi et al., 2011). In addition to resistors and capacitors, inductors are used to represent the amount of inertia in the flow. Using Poiseuille's Law, the resistance R and inductance l of a cylindrical tube can be defined as

$$R = \frac{8\mu L}{\pi r^4}\,, \tag{2.3}$$

$$l = \frac{\rho L}{A}\,, \tag{2.4}$$

where L, r, and A are the length, radius, and cross-sectional area of the tube, respectively, and where μ and ρ are the dynamic viscosity and density of the fluid, respectively. The capacitance of a fluid system is defined as

$$C = \frac{\Delta V}{\Delta P}\,. \tag{2.5}$$

The capacitor that we designed for this experimental flow loop is a column of air in a closed tube that sits above the working fluid. For this configuration, Kung et al. (2011b) showed that the capacitance of the air, when the changes in air volume are small relative to the reference volume, is

$$C_{air} = \frac{V_{air}}{P}\,. \tag{2.6}$$

With these equations, it is possible to estimate the resistance, capacitance, and inductance of a given fluid system and use the resulting LPN equations to predict the flows and pressures in the system. Due to the nature of our 3D printed model and the numerous connection pieces in the experiment flow loop, which can have sharp contractions and expansions, it was not possible to generate a fully accurate LPN for our setup. However, the LPN did allow us to confirm that lowering the amount of inductance, or inertia, in our system would reduce the overall pressure and prevent highly negative pressures after valve closure. This supported our design change to have the pulsatile flow generated close to the model and to use the inlet tank and atrium proxy to decouple the system from the long inlet supply tube from the steady pump. The decrease in inertia provided the largest improvement in our pressure waveforms.

Iteration with our setup, aided by insight from LPN concepts, revealed that the proximal resistance to the model also played a large role in lowering the pressures and affected the timing of valve closure. We therefore changed the tubing at the LPA and RPA outlets of the model to flexible Tygon 15.88mm diameter tubing, up from 12.7mm diameter tubing, taking advantage of the relationship between tubing radius and resistance demonstrated in Equation 2.3 to drastically lower the resistance. The capacitors are made of capped 101.6mm diameter PVC pipe, which stand at 241.3mm, based on designs by Figliola et al. (2010). The capacitors can be tuned to contain different volumes of the working fluid and of air. Increasing the volume of air introduces additional compliance to the flow loop. The amount of capacitance gave us control over the timing of valve closure, which was a key component in achieving physiological pressure differences during diastole. Flexible silicone 12.7mm diameter tubing connects the capacitor outlets to an outlet tank, which drains back to the supply reservoir that feeds the pump. We used an external pinch valve on one of the distal tubing branches to tune the left-right flow split as necessary. The height of the outlet tank was adjusted to replicate the desired downstream pulmonary vascular resistance, which influences the downstream pressure during diastole.

2.3.5 Physiological Flow and Pressure Waveforms

For reference physiological flow waveforms, we used the MPA and branch PA flow rates from the study by Cheng et al. (2005) on proximal pulmonary blood flow in healthy patients, scaled to match our standard cardiac output of 3.5 L/min. For reference pressure waveforms, we used the right heart catherization data from the study by Bangalore and Bhatt (2011). The relevant waveforms from both studies are reproduced in Figure 2.7. Our goal in matching the flow rate conditions was to reach reasonable peak MPA flow of 12-14 L/min and peak branch PA flow of 6-8 L/min, with waveforms with a rounded peak during systole and settling back down

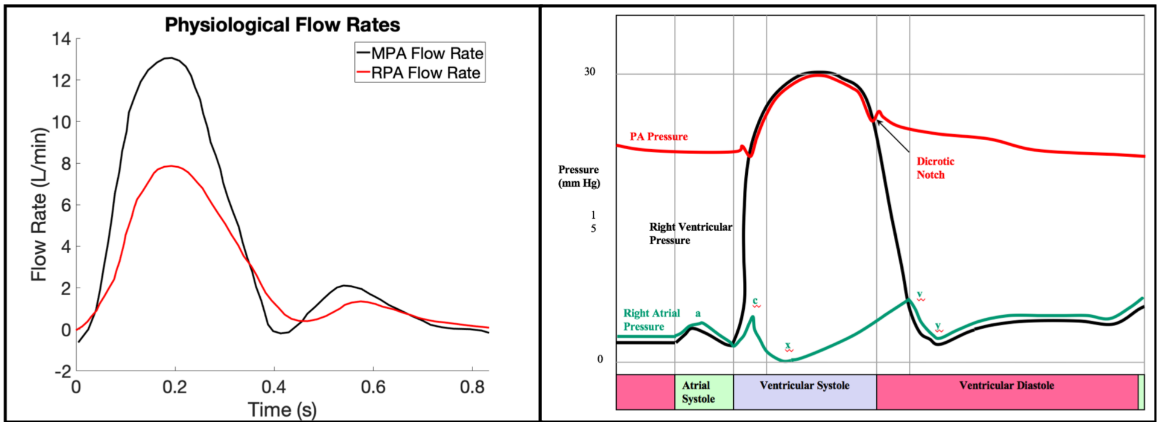

Figure 2.7: Physiological flow rate waveforms in the MPA and RPA (left) and physiological pressure waveforms in the RV and MPA (right). Flow rate data were plotted based on data and figures in Cheng et al. (2005). The pressure waveform on the right is directly reproduced from Bangalore and Bhatt (2011).

to zero flow during diastole. Our goal in matching the pressure conditions was 20-30 mmHG for systolic pressure with the RV pressure dropping to 5-10 mmHG during diastole, creating a pressure difference of 10-20 mmHg between the RV and the MPA at diastole. The pressure waveforms should also have a rounded peak during systole, similar to the flow rates. In terms of timing, the pressure should lead the flow rate and systole should be approximately 40% of the cardiac cycle.

All of the experimental flow loop components were tuned so that the pressure and flow rate waveforms in the experimental model reasonably matched physiological conditions. The pressures were measured with Millar (Houston, Texas) SPR-350 pressure transducer catheters inserted in the model through sealed ports. The RV pressure was measured directly upstream of the valve while the MPA pressure was taken immediately downstream of valve; both catheters were centered in the vessel. The branch flow measurement was collected using a Transonic Systems (Ithaca, NY) ultrasonic flow probe placed around each branch PA. The locations of these flow probes, and the one placed upstream of the model to monitor the cardiac output are seen in Figure 2.6. We ran all experiments at a heart rate of 72 beats per minute and targeted a 50-50 split for flow in the LPA and RPA.

The physiological pressure and flow rate waveforms in the healthy control model

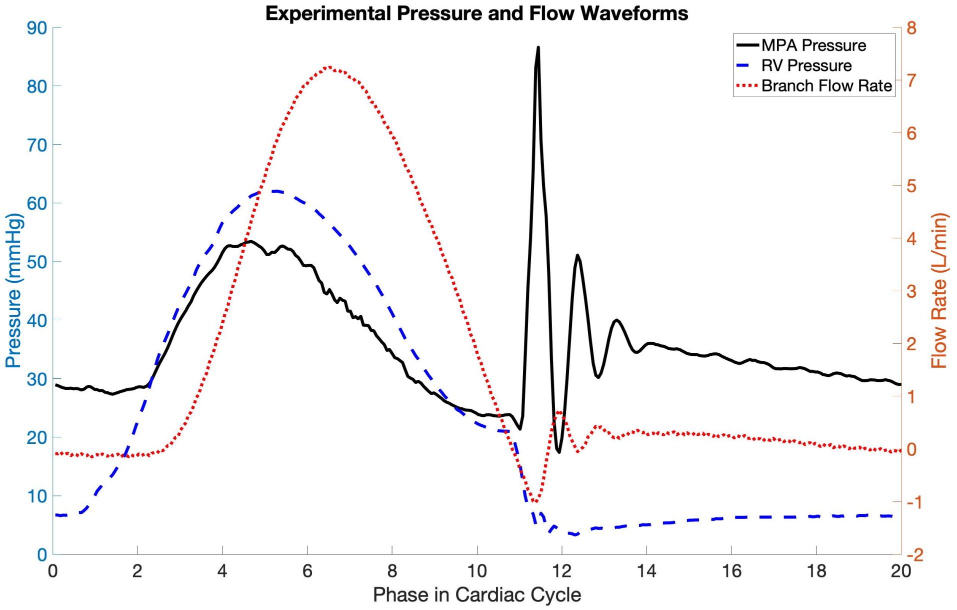

Figure 2.8: Experimental pressure and flow rate waveforms in the healthy control model. MPA and RV pressures (plotted against the left axis) were measured by catheters. The flow in the outlet branch (plotted against the right axis) was measured by an ultrasonic flow probe. Data for all waveforms were taken simultaneously.

are shown in Figure 2.8; the flows in the branch arteries were similar, so only one is displayed here. The flow rate waveform matches our target very well in both shape and peak systolic value. The RV and MPA pressures are higher than our target of 30 mmHg, but given the constraints of a rigid model and how much we had improved the pressure waveform compared to our original design, we determined these systolic pressures to be acceptable. The oscillations in the RV pressure waveform were likely due to wave reflections in the rigid models and resonance in the flow. These oscillations had a limited, but noticeable effect on the branch flow rate waveforms measured by the probes. However, they did not affect the flow rate measured from the 4D flow MRI data or prevent proper valve closure. The adjustable capacitance governed the pressure amplitude and waveform characteristics, while the programmable air supply waveform that controls the ventricle box allowed for adjustments to the waveform and the systolic duration of the cardiac cycle.

Chapter 3

Effects of RVOT Anatomy

This chapter contains large portions of the following paper: N. K. Schiavone, C. J. Elkins, D. B. McElhinney, J. K. Eaton, and A. L. Marsden. In Vitro Assessment of Right Ventricular Outflow Tract Anatomy and Valve Orientation Effects on Bioprosthetic Pulmonary Valve Hemodynamics. *Cardiovascular Engineering and Technology*, 12(2):215-231, April 2021. (Schiavone et al., 2021)

3.1 Background

Tetralogy of Fallot (ToF) is a congenital heart defect occurring in 1 in 2500 newborns annually in the US. Patients with ToF require surgical repair, involving closure of the ventricular septal defect and reconstruction of the malformed right ventricular outflow tract (RVOT), typically within the first few months of life. This repair often leaves patients without a functioning pulmonary valve and reintervention to insert an artificial pulmonary valve is typically necessary in late childhood, adolescence, or early adulthood. In many cases, multiple pulmonary valve replacement (PVR) procedures are required over a lifetime.

Xenograft bioprosthetic valves, along with allograft or xenograft valved conduits, are the most commonly used prostheses for RVOT reconstruction in patients with

ToF and other forms of congenital heart disease in which PVR is necessary (Batlivala et al., 2012; Chen et al., 2012; Babu-Narayan et al., 2014; Zubairi et al., 2011; Lee et al., 2012). While mechanical valves are more durable, they require long-term anti-coagulation therapy, which poses high risks in children (Siddiqui et al., 2009). The main disadvantage of bioprosthetic valves, however, is that most are subject to structural degeneration and dysfunction over time, often within 10-15 years of implantation depending on patient age, size, and other factors (McElhinney et al., 2011; Siddiqui et al., 2009; Vongpatanasin et al., 1996). Despite extensive clinical experience with bioprosthetic valves in the RVOT, these valves fail early and unpredictably in as many as 30% of ToF patients (Oliver et al., 2015; Khanna et al., 2015). Valve degeneration and dysfunction, and interventions to treat them, are important causes of morbidity in these patients. At present, it is not possible to predict which patients will develop accelerated valve dysfunction and there are no surgical or clinical measures proven to extend bioprosthetic pulmonary valve longevity. There are also no clinical guidelines for valve placement or sizing during surgery beyond normative dimensions.

Valve dysfunction after PVR typically occurs as pulmonary regurgitation, pulmonary stenosis, or a combination of both (Batlivala et al., 2012; Lee et al., 2016; Nordmeyer et al., 2009). There are various modes of valve failure that lead to this dysfunction, commonly in the form of calcification, which can produce regurgitation or stenosis, or other types of tissue degeneration such as cusp tears (Siddiqui et al., 2009). However, factors contributing to the degeneration and dysfunction of bioprosthetic valves in the RVOT remain poorly understood. For young patients, valve failure may be partially a function of somatic growth, as the valve cannot accommodate the increasing cardiac output as a patient grows. However, oversizing the valve at placement has not been shown to improve valve lifetime in clinical studies and some studies suggest that oversizing may actually predispose valves to earlier dysfunction (Wells et al., 2002; Karamlou et al., 2005; Chen et al., 2012; Kwak et al., 2016). Additionally, immunologic factors may contribute to dysfunction when valved homograft conduits are placed during PVR (Christenson et al., 2004; Baskett et al., 2003). Beyond these factors, it remains unknown why the trajectory of bioprosthetic valve failure varies so extensively in the RVOT.

Within the ToF patient population, clinical observation reveals a wide range of RVOT anatomies, with significant variations in vessel dilation, radius of curvature, RVOT angle as it extends from the right ventricle (RV), and angle at the first pulmonary artery bifurcation (Schievano et al., 2007). These anatomic variations, particularly after PVR procedures, alter the hemodynamic and biomechanical characteristics of the right heart compared to normal anatomies, leading to adverse effects on RV function (DiLorenzo et al., 2018; Lee et al., 2013; Das et al., 2010; van Straten et al., 2004). In the ToF patient population, one of the most common variations is a dilation in the main pulmonary artery (MPA), local to where prosthetic valves are placed during surgery (Schievano et al., 2007). Previous studies and reviews of prosthetic valves demonstrate their impact on hemodynamics in producing flow patterns not seen in native heart valves (Yoganathan et al., 2004, 2005; Sotiropoulos et al., 2016; Sacks and Yoganathan, 2007; Sacks et al., 2009; Dasi et al., 2009). The complex hemodynamic features in prosthetic valves, including recirculation and stagnation, have been linked to clinical complications (Raghav et al., 2018; Yoganathan et al., 2005; Sotiropoulos et al., 2016; Nordmeyer et al., 2009). Reversed flow is also a key feature for valve performance as some literature suggests some reversed flow may aid the valve during closure, but other studies indicate that too much reversed flow produces regions where hemolysis can occur (Yoganathan et al., 2005; Sotiropoulos et al., 2016). While these previous studies provide a wealth of knowledge on the general features of ToF and valve hemodynamics, there has been limited work examining the role of specific anatomic variations or the impact of valve placement during surgery, particularly in the pulmonary position (Schievano et al., 2011; Biglino et al., 2013b; Vismara et al., 2009; Louvelle et al., 2019). We hypothesize that the gross morphology of the RVOT in ToF, such as a dilation in the MPA, and the placement of the bioprosthetic valves within that diseased anatomy, can significantly change the blood flow patterns in the RVOT and MPA, impacting the hemodynamic environment of the valve.

An overview of experimental techniques for examining the flow fields of prosthetic valves by Raghav et al. highlights a variety of *in vivo* and *in vitro* techniques (Raghav et al., 2018). The most common experimental technique is particle image velocimetry

(PIV), which requires optical access to measure the flow field (Raghav et al., 2018; Nguyen et al., 2017; Lim et al., 2001; Raghav et al., 2019; López-Zazueta et al., 2011; Sotiropoulos et al., 2016). While PIV can provide high spatial and temporal resolution data, it is often limited to capturing 2D slices of the test geometry, and even when 3D PIV techniques are used, idealized geometries frequently are necessary to provide the required optical access (Raghav et al., 2019; López-Zazueta et al., 2011). Durability tests done by valve manufacturers also rely on idealized or standard geometries, without accounting for the variations seen in ToF (Dasi et al., 2009; Palacios-Morales et al., 2018).

Unlike PIV and other experimental methods that require optical access, 4D flow MRI, also called 4D phase contrast MRI or magnetic resonance velocimetry, can obtain full 3D, three-component, phase-averaged velocity fields in complex, opaque models (Elkins et al., 2003; Elkins and Alley, 2007; Markl et al., 2003, 2012). 4D flow MRI is used in various clinical contexts for assessing flow behavior (Stankovic et al., 2014; Lawley et al., 2017; Bächler et al., 2013; Reiter et al., 2008; Barker et al., 2015; Hess et al., 2013; Schäfer et al., 2018). Previous studies have analyzed clinical 4D flow MRI data to quantify flow patterns in ToF, but have not yet examined the role of valve placement and anatomic variability (François et al., 2012; Jeong et al., 2015). We note that 4D flow MRI is limited to measuring mean velocity fields and thus it cannot provide instantaneous flow behavior. 4D flow MRI also presents tradeoffs between spatial resolution, temporal resolution, and scan time, with higher resolutions resulting in longer scans. While studying experimental models allows for more flexibility in scan time than *in vivo* settings, the spatial and temporal resolutions of 4D flow MRI data are typically lower than PIV data. Comparison studies have described the quantitative similarities between 4D flow MRI and PIV data, despite the differences in resolutions between the two techniques (Medero et al., 2018, 2020).

For *in vitro* studies, it is necessary to develop a flow loop that replicates physiological conditions. Professor R. Figliola (Clemson University, SC) and collaborators have developed a successful system of physical resistance and capacitance elements which can accurately capture a variety of cardiovascular conditions (Figliola et al., 2010; Gohean et al., 2006; Biglino et al., 2013a; Camp et al., 2007; Hang et al., 2016;

Vukicevic et al., 2014). Similar concepts were utilized in this study. Due to the complex geometries seen in ToF and the 3D nature of the flow produced by bioprosthetic valves, we aim to study these complex geometries with varied valve placements to examine their impact on the hemodynamic environment of the valve using 4D flow MRI. Understanding how valve placement changes the flow patterns in an anatomy can be leveraged for future clinical decision-making during PVR surgery.

3.2 Experimental Details

This chapter analyzes the flow fields in two RVOT models. The first is the healthy control model described in Section 2.2. The second model is a generalized diseased case for ToF representing a vessel dilation in the MPA which is frequently observed in the clinic. Immediately after the valve annulus, the vessel diameter increases by 150% to 37.5mm and then tapers along the MPA and branch arteries. Both models have the same centerline path and bifurcation angles, such that this diameter increase is the only difference between them (Figure 3.1).

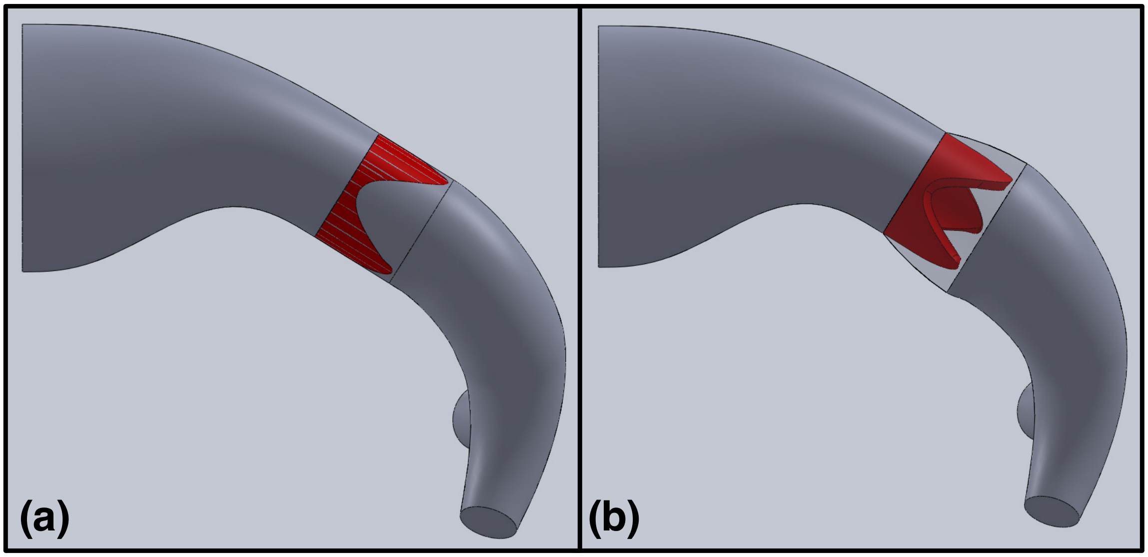

Figure 3.1: The SolidWorks designs for the healthy RVOT model (a) and the diseased RVOT model (b). A mock valve (not to scale) is included in red to demonstrate its placement.

Both models were manufactured using stereolithography (SLA) with DSM Somos WaterShed XC 11122 resin at the W.M. Keck Center at the University of Texas, El Paso. The model design is modular to allow for adjustments in valve placement and in the overall geometry. The downstream piece consists of the MPA, LPA, and RPA. It is connected upstream to a two-piece valve-holder, which is the same for both models and designed to hold a 25mm St. Jude Medical Epic porcine trileaflet surgical valve. The valve-holder components each have a groove that clamps around the sewing ring of the valve. The valve-holder can rotate independently of the other components, allowing for experiments to be run with the valve in different rotational orientations (Figure 3.2). All components of models and the valve itself are fully MR compatible.

Upstream of the valve-holder is a two-component piece that consists of the RVOT and a box that acts as an analog for RV, used for both models. The custom designed, MR compatible ventricle box was inspired by pulsatile ventricular assist devices, such as the Berlin Heart EXCOR (The Woodlands, TX). The RV is modeled as a cylindrical cavity within a 102mm by 102mm by 108mm box separated in the center by a thin silicone rubber membrane. One half of the ventricle box contains the working fluid with a 27mm trileaflet bioprosthetic valve at the inlet, acting as the tricuspid valve, and an exit that contracts from 72.6mm diameter to 25mm diameter, which models the RVOT and connects to the valve-holder. The other half of the ventricle box is an air chamber supplied with pulsatile pressurized air. Thus, the ventricle box pneumatically drives the pulsatile flow in the physiological models.

The experimental flow loop replicates the right heart circulation and pulmonary physiology, as shown in the schematic in Figure 3.3. An upstream inlet tank, fed by a steady centrifugal pump from a supply reservoir, connects to a flexible bag that acts as a right atrium. The atrium proxy feeds the ventricle box through the 27mm bioprosthetic tricuspid valve. The ventricle box is pneumatically driven by an air supply controlled by a programmable proportional pressure regulating valve (Parker Hoerbiger Origa, Richland, MI; model PS120006-020-035) and a binary solenoid valve. A constant air pressure source is fed through the programmable valve that outputs the air as a half sine wave. This pulsatile air supply pushes the membrane in the ventricle box to create systole and diastole. The solenoid valve provides venting from

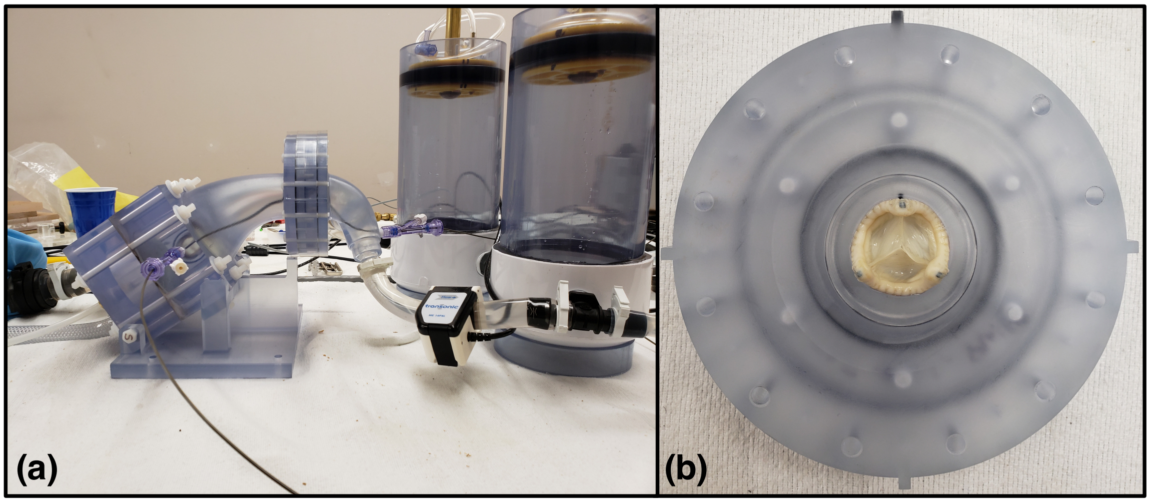

Figure 3.2: The 3D printed model of the RVOT connected to the ventricle-analog box upstream and capacitors downstream (a) and the surgical valve clamped in the model (b).

the ventricle box to replicate the relaxation of the RV during diastole. Thus, pulsatile flow leaves the ventricle box to flow through the 3D printed model of the RVOT and PAs.

The outlets of the model at the LPA and RPA connect to flexible Tygon 16mm diameter tubing, which in turn connect to capacitors made of capped 102mm diameter PVC pipe, based on designs by Figliola et al. (2010). The capacitors can be tuned to contain different volumes of the working fluid and of air, where the volume of air introduces additional compliance to the flow loop. Flexible silicone tubing connects the capacitor outlets to an outlet tank, which drains back to the supply reservoir that feeds the pump. The two segments of flexible tubing and the capacitor on each outlet branch replicate a resistor-capacitor-resistor Windkessel model that can be tuned to change the outlet boundary conditions for the test section. The height of the outlet reservoir can be adjusted to replicate the desired downstream pulmonary vascular resistance.

These components were tuned so that the pressure and flow rate waveforms in the experimental model matched physiological conditions, compared to previously reported pressure data and flow rate waveforms at rest conditions scaled to the target cardiac output (Cheng et al., 2005; Bangalore and Bhatt, 2011). The pressures were measured with Millar (Houston, Texas) SPR-350 pressure transducer catheters inserted into the model through sealed ports. The RV pressure was measured directly upstream of the valve while the MPA pressure was taken immediately downstream of valve; both catheters were centered in the vessel. The branch flow measurement was collected using a Transonic Systems (Ithaca, NY) ultrasonic flow probe placed around each branch PA. The physiological pressure and flow rate waveforms in the model are shown in Figure 3.4; the flows in the branch arteries were characteristically similar, so only one is displayed here. The oscillations in the RV pressure waveform were due to wave reflections in the rigid models and resonance in the flow. These oscillations had a limited, but noticeable effect on the branch flow rate waveforms measured by the probes. However, they did not affect the flow rate measured from the 4D flow MRI data or prevent proper valve closure. The adjustable capacitance governs the pressure amplitude and waveform characteristics, while the programmable air supply waveform that controls the ventricle box allows for adjustments to the waveform and the systolic duration of the cardiac cycle. The cardiac output for the experiments in this chapter was 3.5 liters/min, a mid-range cardiac output for pediatric patients, with a heart rate of 72 beats per minute and a systolic duration of approximately 40%.

The velocity data were measured using a 4D flow MRI sequence developed for *in vitro* settings as described by Elkins et al. (2003) using the data acquisition technique described by Pelc et al. (1994). Using 4D flow MRI to acquire the velocity data has two key benefits. First, this method uses a 4D phase contrast MRI sequence that is nearly identical to those used in clinical scans, allowing for future comparison to *in vivo* data. Second, 4D flow MRI captures the full mean velocity fields throughout the model without the need for optical access that is required by other methods, such as PIV, allowing for interrogation of complex geometries that are 3D printed with opaque materials. The experiments were conducted in a whole body, 3 Tesla General Electric MRI scanner at the Richard M. Lucas Center for Imaging at Stanford University. The main test section was passed through the bore of the magnet (Figure

3.3). The working fluid for the flow loop was a blood analog fluid of 60% water and 40% glycerin, with a density of 1.1 g/cm^3 and a viscosity of 3.9 centipoise at room temperature in the magnet room. Gadolinium was added to the blood-analog fluid to increase the signal contrast during the 4D flow MRI scan.

This chapter includes four cases: the healthy model and the diseased ToF model, each with two different valve orientations. One orientation is the native position of the pulmonary valve in a healthy heart, with one of the valve commissures aligned with the posterior, inner curve of the MPA; surgeons generally aim to replicate this configuration during the PVR procedure. The second orientation was rotated 180 degrees from the native orientation, so that one of the valve commissures was aligned with the anterior, outer curve of the MPA. For all experiments, the slice direction for the MRI scan was sagittal, with a spatial resolution of 0.9mm in the sagittal, axial, and coronal directions. Each scan was approximately 21 minutes long. For each case, we conducted four scans with the flow pump on and three scans with the pump off. The pump-off scans were averaged and subtracted from the pump-on scans to reduce various sources of error, including eddy current effects (Elkins and Alley, 2007). The pump-on scans were then averaged to improve the signal to noise ratio (SNR) of the velocity data. Each scan was phase-locked, allowing for measurements at different points throughout the cardiac cycle. The digital trigger signal governing the pneumatic ventricle box producing the pulsatile flow was connected to the ECG converter and trigger on the MRI system to signal the start of each cardiac cycle. The temporal resolution was 0.077 seconds, which allowed for direct measurement of 10 phases; these data were used to interpolate to 20 total phases in the cardiac cycle. Thus, for each scan, we report phase-locked, 3D, three-component, time-averaged velocity fields for 20 phases of the cardiac cycle.

The expected uncertainty of 4D flow MRI velocity measurements is given by

$$\delta_u = \frac{\sqrt{2}}{\pi}\frac{\mathrm{VENC}}{\mathrm{SNR}} \tag{3.1}$$

where SNR is the signal to noise ratio and VENC is the velocity encoding value, an MRI scanner parameter that sets the maximum velocity measured during the scan without aliasing. For 4D flow MRI scans, the VENC must be set high enough to prevent velocity aliasing during the scan, but still low enough to allow for sufficient resolution at low velocities. For all experiments, the VENC was set at 250 cm/s in the sagittal, axial, and coronal directions. The average SNR across all scans was 21. The resulting uncertainty was 6.3% of the mean velocity through the valve opening at systole.

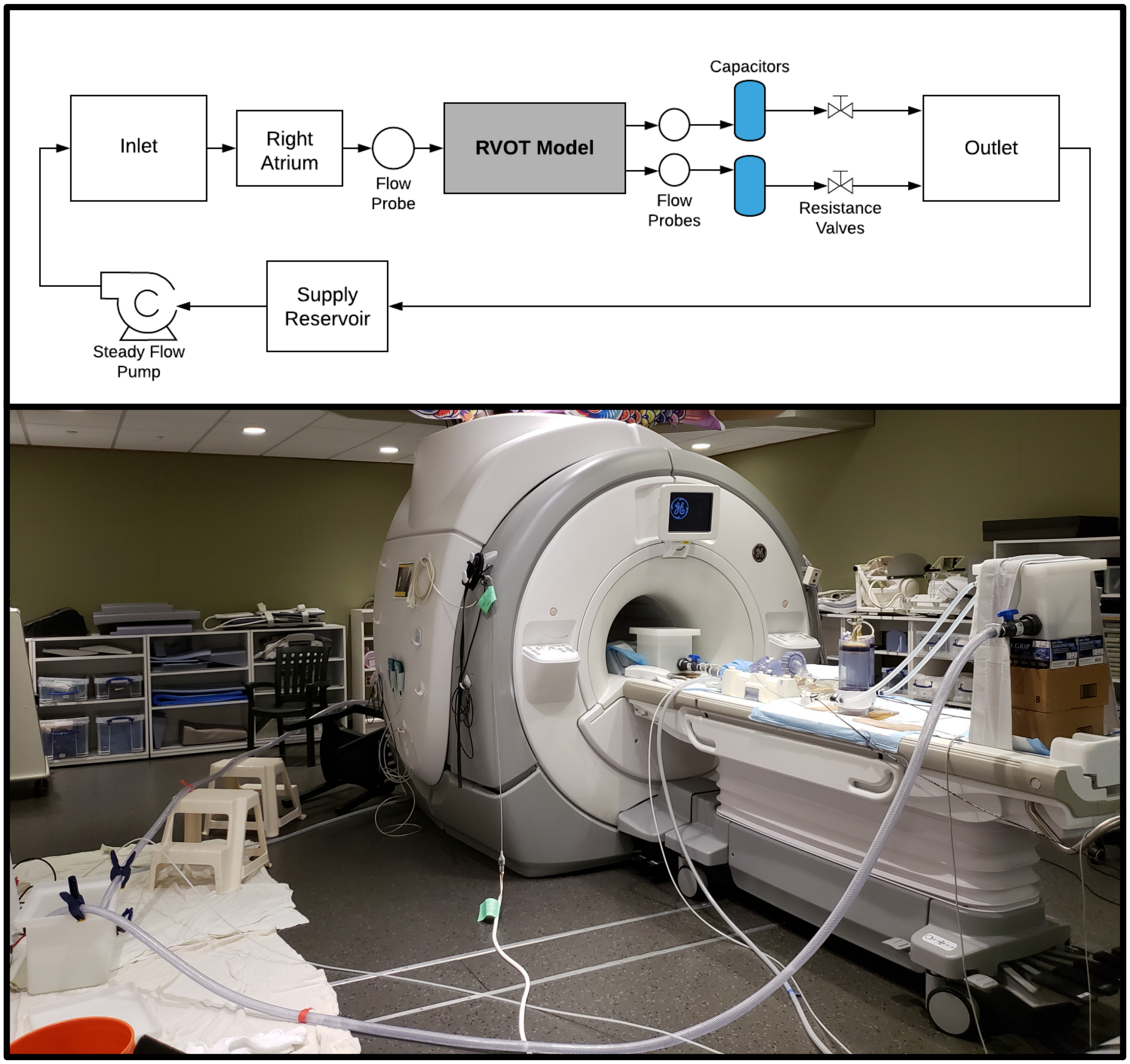

Figure 3.3: A schematic of the experimental flow loop (top) and the setup on the MRI magnet table (bottom).

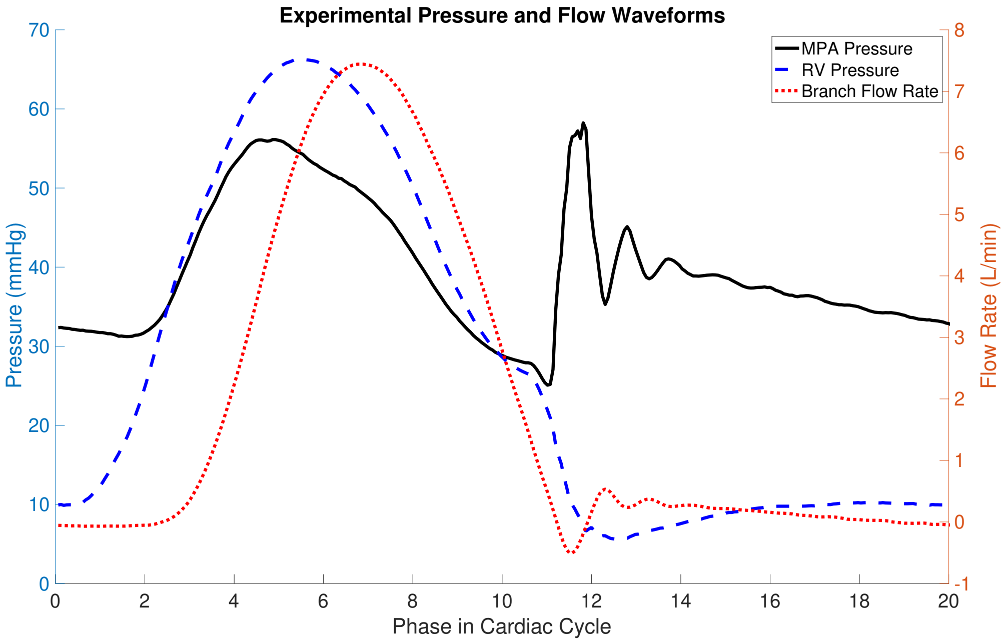

Figure 3.4: Experimental pressure and flow rate waveforms in the dilated MPA model. MPA and RV pressures (plotted against left axis) were measured by catheters. The flow in the outlet branch (plotted against right axis) was measured by an ultrasonic flow probe. Data for all waveforms were taken simultaneously.

3.2.1 Analysis and Metrics

Post-processing of the 4D flow MRI data was done in MATLAB (Natick, MA) and in Tecplot (Bellevue, WA). All flow visualization was done in Tecplot. To allow for direct comparison, the velocity fields for each case were normalized by the peak velocity upstream of the valve in the RVOT; differences between these velocities in each case were within 3%. These normalized velocity fields were used for all visualization and for calculating additional flow quantities and metrics. Vorticity was calculated and visualized in Tecplot, using median filtered velocity fields to reduce noise in the derivatives.

In addition to general analysis of the velocity fields, we utilized two integral parameters that have been proposed previously to analyze 4D flow MRI data in the human airways to quantify the variability of the streamwise and transverse velocity components at key locations in the flow (Banko et al., 2016):

$$I_1 = \left(\frac{\iint \left(\mathbf{u} \cdot \hat{\mathbf{n}}\right)^2 dA}{U_{ref}^2 A} \right)^{\frac{1}{2}} \tag{3.2}$$

$$I_2 = \left(\frac{\iint \|\mathbf{u} - \left(\mathbf{u} \cdot \hat{\mathbf{n}}\right) \hat{\mathbf{n}}\|^2 dA}{U_{ref}^2 A} \right)^{\frac{1}{2}} \tag{3.3}$$

where u is the velocity vector, $\hat{n}$ is the unit vector normal to the cross-section, and U_{ref} is the mean speed in the RVOT immediately upstream of the valve at peak systole, which was approximately equal for all cases. A is the local cross-sectional area of the geometry at the plane where the equations are evaluated. I_1 is a measure of the relative streamwise flow momentum flux: a value of 1 indicates a uniform flow across the cross-section while values above 1.5 indicate high momentum flow. Secondary flows are defined as fluid motions in the plane perpendicular to the normal flow direction. I_2 is a ratio of the total kinetic energy in the secondary flows at a given plane to the kinetic energy in the main flow direction.

3.3 Results

Results are presented for the four experimental cases described above, each including a full 3D phase-averaged velocity field at 20 time points over the cardiac cycle at over 1.6 million points on a uniform Cartesian grid. We first qualitatively compare the overall flow patterns in each case, and then quantify differences in reversed flow and integral metrics.

3.3.1 Qualitative Effect of RVOT Anatomy and Valve Orientation

Examining the full 4D velocity field, several features drastically differed between all cases. The shape and direction of the jet through the valve and the size and strength of reversed and secondary flows were impacted by the RVOT and MPA anatomy and the valve orientation. To provide a clear picture of key flow patterns, we compared normalized streamwise velocity contours at peak systole in an axial slice immediately downstream of the valve support structure and in a sagittal slice through the center of the MPA (Figure 3.5). The support structures of the valve are located at the three valve commissures, as labeled on the valve image in Figure 3.5. For the two cases with the same orientation, the shape and magnitude of the forward streamwise velocity through the valve was very similar, indicating that the larger MPA diameter in the diseased geometry did not strongly affect the forward momentum through the valve opening. However, the RVOT dilation caused the flow patterns surrounding the jet to develop differently. In the healthy geometry, for both orientations, three regions of reversed flow developed directly downstream of the supports at the valve commissures, as seen in the axial slice. However, in the diseased geometry cases, only two large regions of reversed flow formed outside of the jet. As seen in the sagittal slice, the reversed flow was carried back towards the valve leaflets as they closed. Thus, the flow impacted the downstream side of the valve at different locations for all cases. In addition, in the rotated case for the healthy geometry, the pattern of the reversed flow regions rotated 180 degrees just like the valve orientation. However, the reversed flow regions did not directly rotate with valve orientation in the diseased geometry. This revealed a compound effect of geometry and orientation; a trend that was observed for both two valve orientations in one geometry was not guaranteed to occur in a different geometry.

The in-plane vectors on the axial slices reveal secondary flows (Figure 3.5). Due to the larger diameter in the diseased case, the vortices in the jet shear layer had more room to develop and were more coherent, particularly shedding off the bottom left leaflet for the native orientation and the top right leaflet for the rotated orientation (Figure 3.5). This showed the presence of strong recirculation in the diseased geometry for both orientations. The diseased case with the rotated orientation also contained a strong sweeping secondary flow counterclockwise along the posterior curve of the MPA. Thus, the amount and location of recirculating flow in the diseased geometry depended strongly on the valve orientation.

In the sagittal slices, as in the axial slices, the forward flow jet coming out of the valve behaved similarly in each of the four cases. The only substantial change was the direction of the jet. With the native orientation, the jet impacted the anterior curve of the MPA while with the rotated orientation, the jet was directed along the MPA and slightly towards the posterior curve. This change in the jet direction led to differences in the amount and location of reversed flow in each case. With the native orientation, a reversed flow region formed along the posterior curve of the MPA in both geometries. With the rotated orientation, this same location experienced mostly stagnant flow in the healthy geometry but reversed flow persisted in the diseased geometry. Both geometries with the rotated orientation also had reversed flow along the anterior curve that was not present in either native orientation case. The distance between the valve and the reversed flow regions also varied in all four cases. In the healthy geometry with the native orientation, the reversed flow along the posterior curve was close enough to the valve annulus to impact the valve leaflets. However, in the diseased geometry with the same orientation, the separation was located further downstream and stagnant flow surrounded the valve leaflets instead. In contrast, when the valve orientation was rotated in the diseased geometry, the reversed flow along the posterior curves was located close to the valve annulus and leaflets, similar to

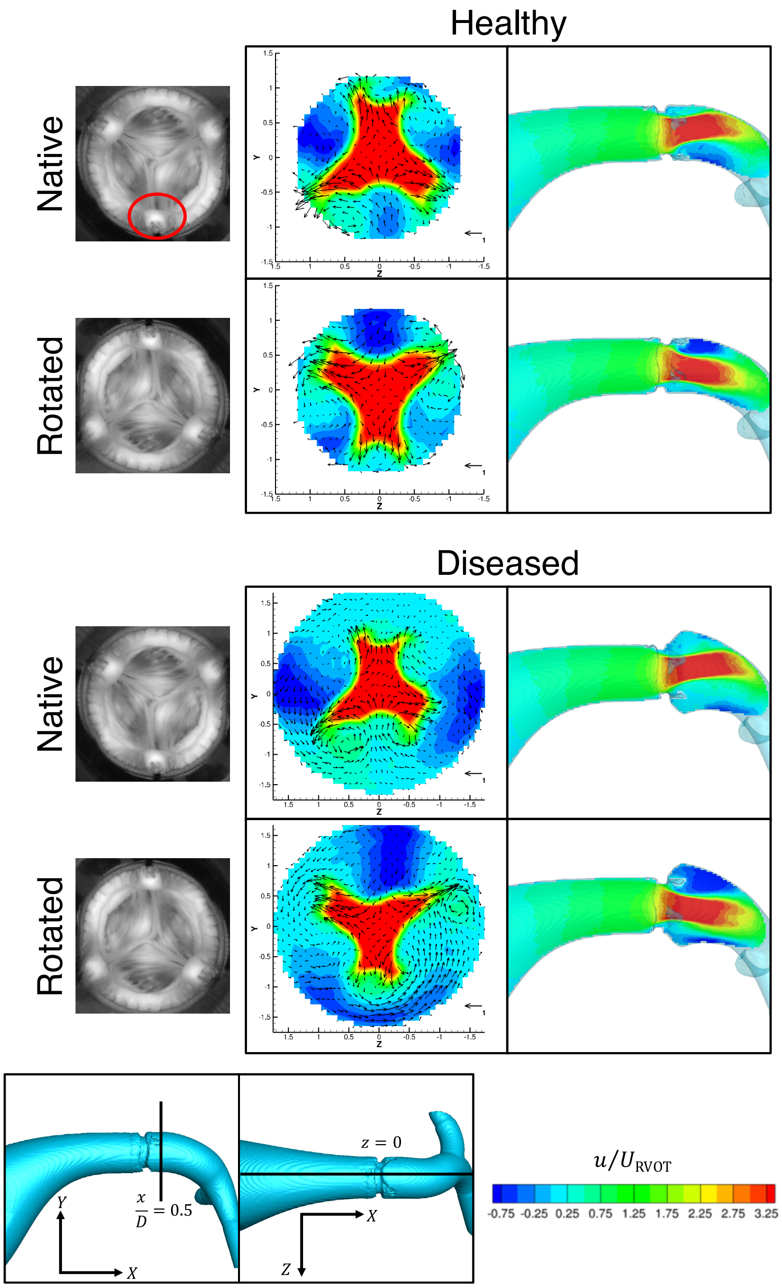

Figure 3.5: X-component of velocity contours normalized by the peak speed in the RVOT upstream of the valve shown at axial slice x/D = 0.5 and sagittal slice z = 0 at peak systole. In-plane velocity vectors are shown on the axial slice with a reference vector representing a normalized velocity of 1. On the left, images of the closed valve show the leaflets in the native and rotated orientation. One of the valve commissures is circled in red in the top image.

the healthy native case. This demonstrated that valve orientation can be leveraged to create flow patterns in a diseased case that mimic those of the healthy case. However, it is worth noting that in this case, it came at the cost of a large separation region along the anterior curve of the MPA which was not present in the healthy native case.

Over the cardiac cycle, the velocity through the valve generally decreased and the reversed flow regions diminished as well, such that the streamwise flow normal to the valve annulus in the MPA returned to zero for most of diastole. The reversed flow regions that occurred along the curves of the vessels shifted their position over the cardiac cycle. The flow began to reverse in the MPA at peak systole in the locations shown in Figure 3.5. As the flow through the valve decelerated, the reversed flow moved back towards the valve annulus, and, in the diseased geometry cases, all of the flow around the valve was reversed. The reversed flow persisted slightly longer than the forward flow through the valve before the flow became still in the MPA for diastole.

While the streamwise flow stagnated in all cases, this did not hold for the radial velocities. The radial velocity in an axial plane just downstream of the valve annulus illustrates the flow patterns close to the valve leaflet surfaces (Figure 3.6). At systole, the two geometries had similar flow patterns. Between the open edges of the leaflets, the flow moved toward the center of the vessel as seen in the blue radial flow contours that correspond with the commissure locations. As the valve opened, the surface of the leaflets pushed the flow outward towards the vessel walls, generating the red radial flow contours on the outside of the opened leaflets at peak systole. However, during diastole, the two geometries produced substantially different flow patterns. In the healthy geometry, the flow was stagnant during diastole. In the diseased geometry however, we observed strong flow moving towards the center of the vessel. This flow washed directly over the closed bottom right leaflet during diastole. This persistent radial velocity was likely caused by the excess flow in the dilated vessel that was not present in the healthy MPA. In both geometries, as the valve closed, the flow along the walls of the MPA moved back towards the valve. In the diseased geometry only, this flow continued to sweep over the leaflets after the valve closed, as seen in the radial flow contours.

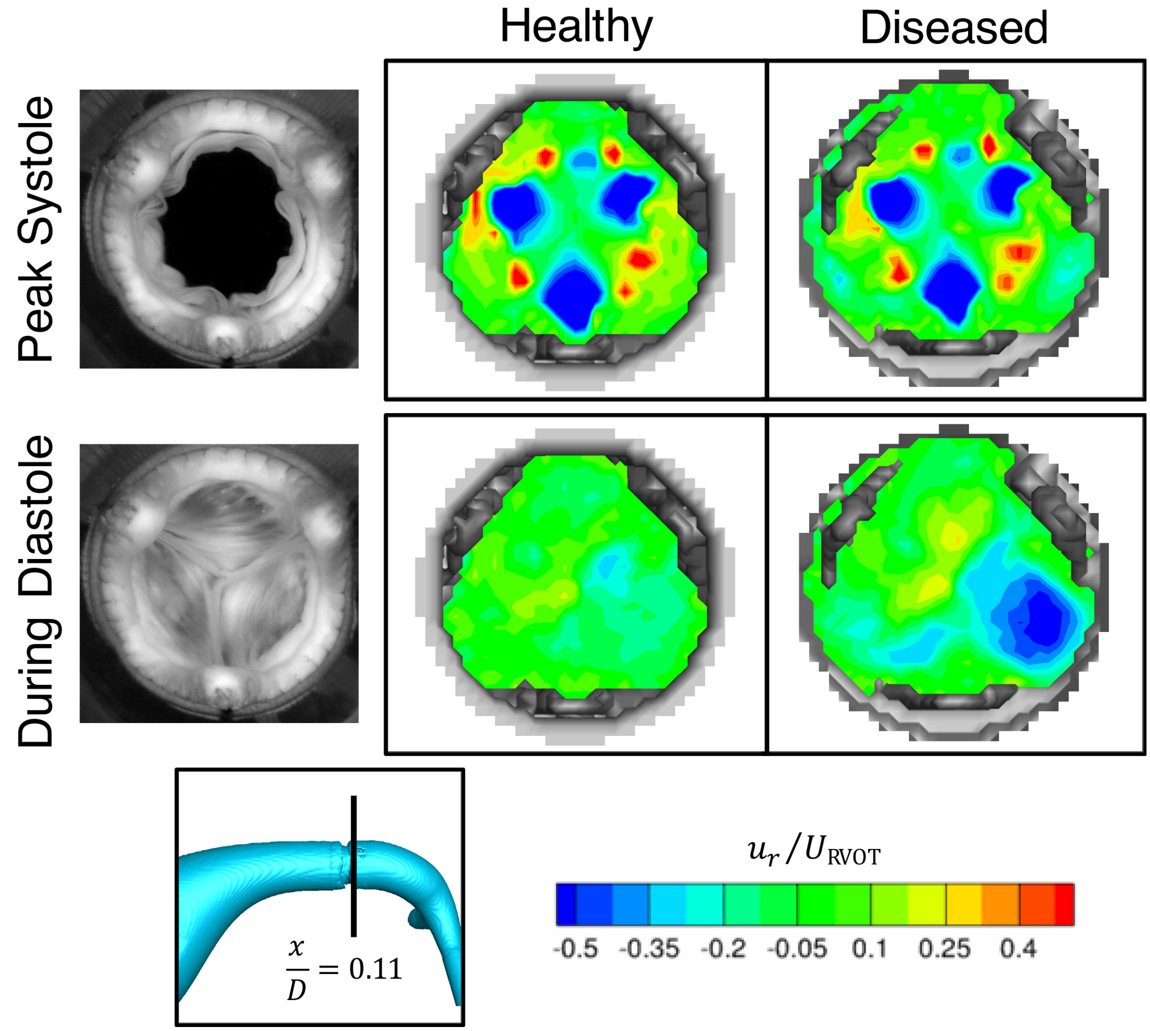

Figure 3.6: Radial velocity contours computed from the normalized velocity components local to the valve annulus (x/D = 0.11) during systole and diastole. On the left, images of the valve show the leaflet positions during systole and diastole.

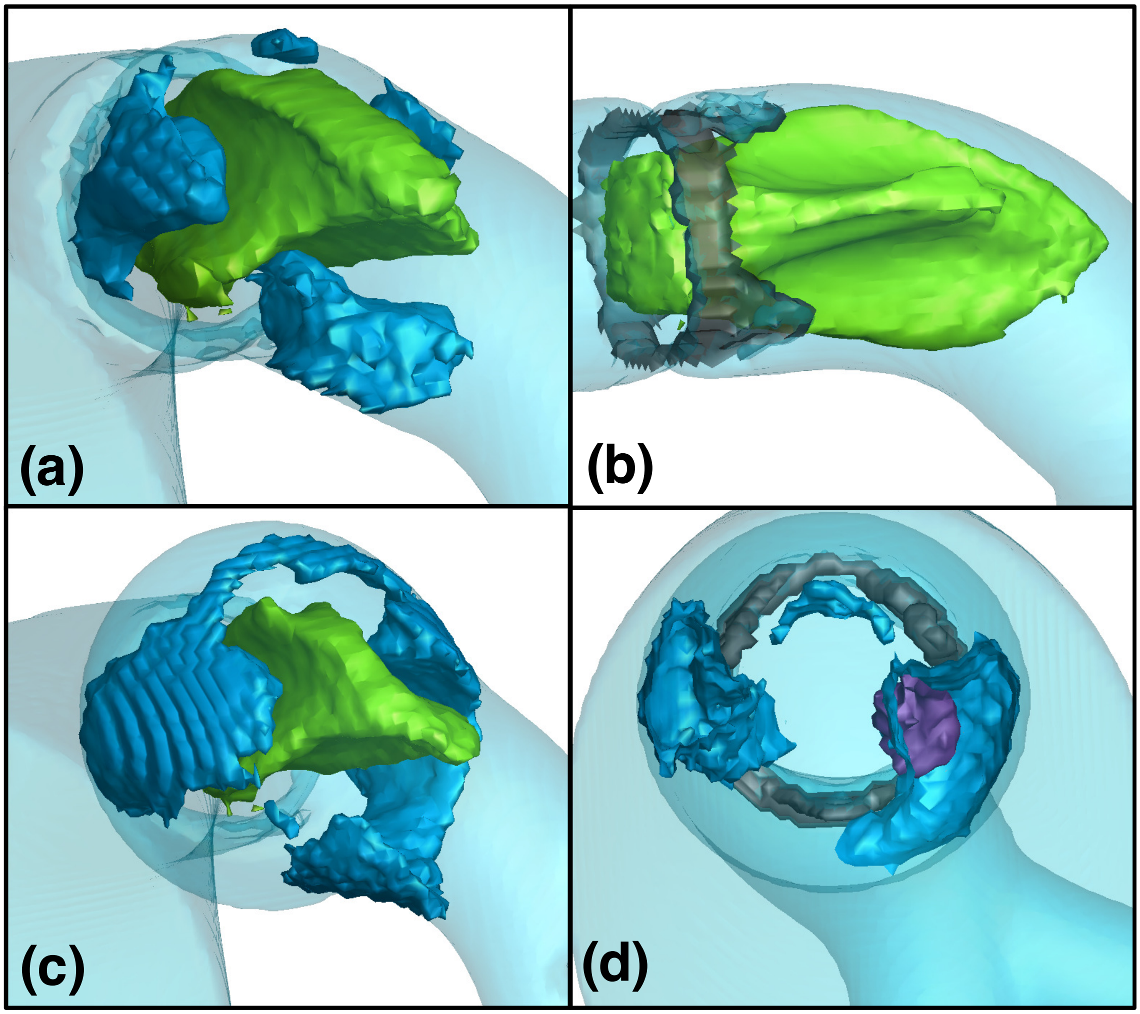

Figure 3.7: Velocity isosurfaces in the healthy geometry at peak systole (a, b), the diseased geometry at peak systole (c), and the diseased geometry during diastole (d). In the healthy geometry and the diseased geometry at systole, green and blue represent x-component of velocity isosurfaces at $u/U_{RVOT} = 2$ and $u/U_{RVOT} =$ -0.125 respectively. For the healthy geometry, two angles are provided, with (a) illustrating both forward and reversed flow and (b) highlighting the shape of the forward jet through the open valve. In the diseased geometry during diastole (d), blue still represents an x-component of velocity isosurface at $u/U_{RVOT} =$ -0.125 and purple represents a radial velocity isosurface at $u_r/U_{RVOT} =$ -0.36. The structure of the valve is shown in gray in (b) and (d).

The full 3D features of the flow can be observed with isosurfaces of the x-component of velocity, which is normal to the valve annulus (Figure 3.7). While the valve orifice had an almost circular shape, the jet through the valve was impacted by the leaflets and support structure,resulting in a more triangular shape in the flow downstream (Figure 3.7b). The three points of the jet formed along the opened leaflets while the deficits occurred where the support scaffolding of the valve extends from each commissure. The reversed flow was generated by the flow moving through the open valve geometry, as seen in both the healthy and diseased geometry (Figure 3.7a,c). In the diseased geometry, additional flow moved back towards the valve annulus through the open space between the leaflets and the vessel wall. While the shape and size of these reversed flow regions changed with the geometry and orientation, the general pattern of a triangular jet surrounded by reversed flow held true across all cases. The 3D nature of the flow also shed insight on the formation of the radial flows seen in Figure 3.6. In the diseased geometry, the isosurfaces revealed that as the reversed streamwise flow persisted in diastole, radial flow towards the center of the vessel was generated within this flow as it impacted the valve annulus (Figure 3.7d). Thus, the radial flow was fed by the reversed streamwise flow in the diseased case. The reversed streamwise flow was not strong enough to persist in the healthy geometry and so could not generate the radial flows seen in the diseased geometry.

Analyzing the x-component of vorticity reveals additional features of the flow, particularly around the valve leaflets during systole (Figure 3.8). Longitudinal vorticity forms along the open valve leaflets, resulting in opposite sign vortices on each edge of the leaflet. For example, as the two leaflets in the center of Figure 3.8 open, positive x vorticity develops on the right edge of the leftmost leaflet. Conversely, negative x vorticity develops on the left edge of the rightmost leaflet. This pattern is repeated for all three valve leaflets along each of the openings and is present in both geometries and valve orientations. The vorticity isosurfaces align with the vortices shown by in-plane velocity vectors, similar to those seen in Figure 3.5. The axial slice clearly shows that the vorticity streaks correspond to actual vortices, comprising flow rotating around an easily identified center. Although the overall pattern is similar between both geometries, there are some key differences. In the diseased geometry, the vortex structures emanating from the valve leaflet openings are slightly smaller than in the healthy geometry, particularly along the leaflet on the outer curve of the vessel. However, the diseased geometry also has additional structures outside of the valve scaffolding, as seen in the top right and top left of Figure 3.8c. These differences reveal how variations in geometry can affect the complex 3D flow through the valve. It should be noted that other transient vortices may be present, but are not resolved by the current measurements. Vortex ring structures, for example, would translate too rapidly to be captured at the present temporal resolution in the MRV data.

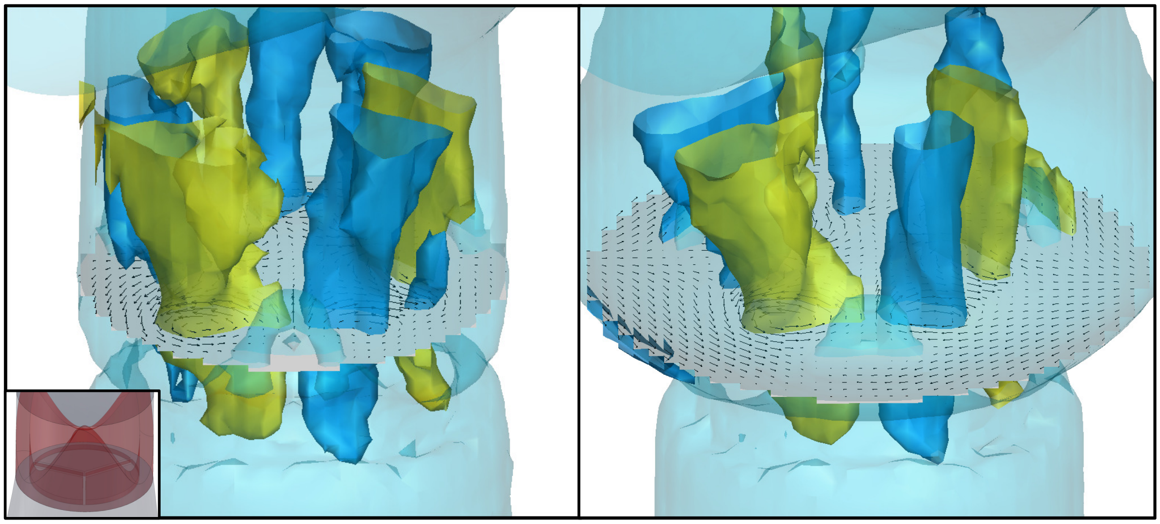

Figure 3.8: Isosurfaces of the x component of vorticity (ω_x) for the healthy geometry (left) and the diseased geometry (right), both with the native orientation at peak systole. The orientation is shown (inset on left), demonstrating the location of valve leaflet openings; the opening in the center is along the inner curve of the MPA. An axial slice at x/D = 0.25 is shown in gray with in-plane velocity vectors; the x direction is normal to this plane. Isosurfaces are displayed for ω_x = -2 in blue and ω_x = 2 in yellow, and are truncated at x/D = 0.75.

3.3.2 Quantitative Metrics

To quantitatively assess the differences in flow among all four cases, we examined the volume and asymmetry of the reversed flow regions as well as integrated quantities for the streamwise momentum and secondary flow strength.

Reversed Flow Regions

The reversed flow in the RVOT may have an impact on valve behavior as the flow decelerates and the leaflets close. For each case, the volume of reversed streamwise flow was computed for the section of the MPA immediately downstream of the valve annulus extending just beyond the valve support scaffolding (Figure 3.9). For all cases, the percentage of the total volume experiencing reversed flow increased during the flow acceleration part of systole. After this acceleration however, sometime between phases 5 and 6 of the cardiac cycle, the healthy geometry and diseased geometry diverged. While the percentage of reversed flow in the healthy geometry was fairly steady through the rest of systole for both orientations, the percentage of reversed flow in the diseased geometries continued to increase. Both orientations for the diseased geometry followed this trend, though the rotated orientation had more reversed flow throughout all of systole.

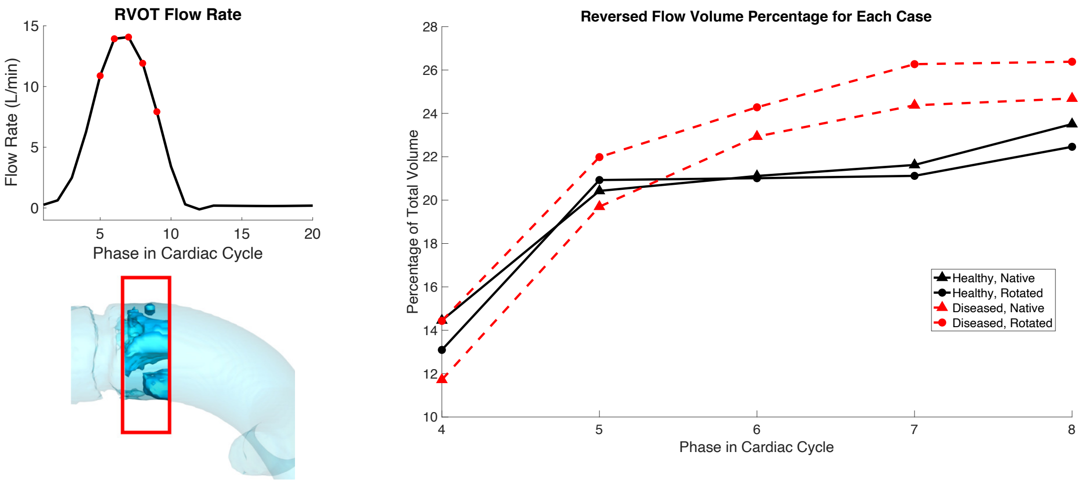

Figure 3.9: Percentage of the total volume downstream of the valve that contained reversed flow during systole for each of the four cases (right). The flow rate waveform calculated from the 4D flow MRI data is shown in the top left, with points indicating the phases of systole corresponding to the plot on the right. The volume downstream of the valve used for the calculations is shown in the bottom left.

While the overall percentage of reversed flow volume likely impacted the valve, it did not affect each leaflet equally. Both the native and the rotated orientation were divided into three sections that correspond to each of the leaflets (Figure 3.10). The volume of reversed flow was summed in each section over the phases of systole to determine how much of the reversed flow impacted each leaflet. The reversed flow downstream of the valve was highly asymmetric with respect to the leaflets and this asymmetry varied depending on the geometry and the valve orientation (Figure 3.10). For both geometries with the native valve orientation, the bottom left leaflet experienced the most reversed flow while the top leaflet experienced the least. This was particularly pronounced in the diseased geometry where hardly any of the reversed flow impacted the top leaflet. In the rotated orientation for the healthy geometry, the top left leaflet experienced the most reversed flow instead, while the other two leaflets were approximately equally affected. However, this trend did not hold in the diseased geometry with the rotated orientation, where the bottom leaflet experienced the highest volume of reversed flow. The geometry and orientation had a compound effect on the asymmetry of the reversed flow, where the diseased rotated case produced features entirely distinct from the other three cases. Additionally, the reversed flow in the native orientation cases was noticeably more asymmetric than the rotated orientation. This may be a product of the jet through the valve being more aligned with the vessel in the rotated cases as opposed to being directed towards the outer curve in the native cases (Figure 3.5).

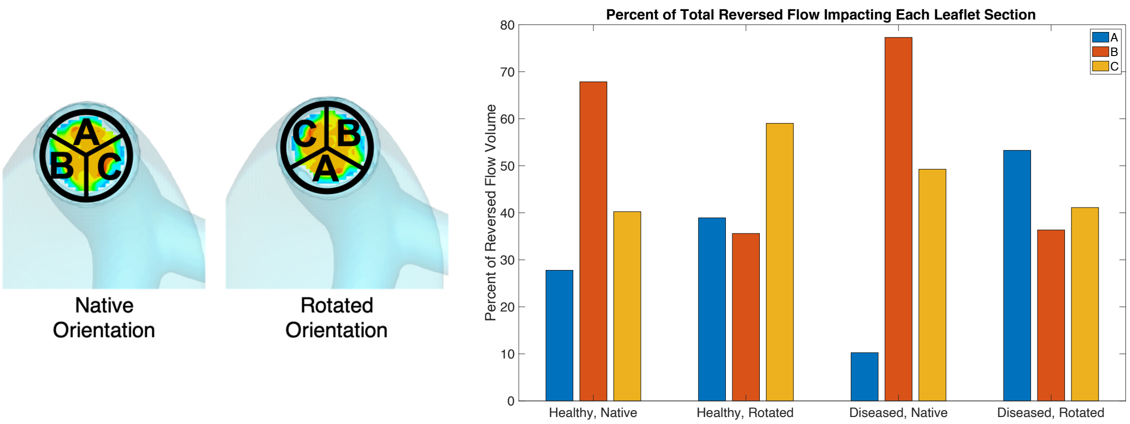

Figure 3.10: Percentage of the volume of the reversed flow that occurred in each individual leaflet section during systole for each of the four cases (right). The definition of the leaflet sections for each orientation is shown on the left.

Integral Metrics

To quantify the variability of the streamwise and transverse velocity components at key locations in the flow, we calculated the integral parameters in Equations 3.2 and 3.3 from the 4D flow MRI data for all four cases in the MPA, downstream from the valve annulus at x/D = 0.5 (Figure 3.11). The streamwise momentum (I_1) for the diseased case for both valve orientations was noticeably lower than in the healthy cases. This was expected due to the larger vessel area in the diseased geometry experiencing the same inlet flow as the non-dilated healthy geometry. The valve orientation did not affect I_1 within the same geometry, demonstrating that the streamwise momentum of the flow through the valve was independent of orientation. In both geometries, I_1 exceeded 1 during peak systole, representing the high momentum flow through the fully opened valve. The secondary flow strength, I_2, was also lower for the diseased cases than the healthy cases, which was also a result from approximately the same reference flow rate going through a larger diameter vessel. However, while I_2 was approximately the same for both orientations in the healthy geometry, this was not true for the diseased geometry. The rotated orientation had stronger secondary flows and the peak strength occurred later in the cardiac cycle. In addition, this increased I_2

was sustained into diastole in the diseased case with the rotated orientation, demonstrating that the secondary flows took longer to dissipate. The increased strength and duration of the secondary flow energy in this case was likely due to the more pronounced swirling flow along the inner curve of the MPA, as seen in Figure 3.5. These differences in I_2 again demonstrated the compound effects of geometry and orientation on the flow.

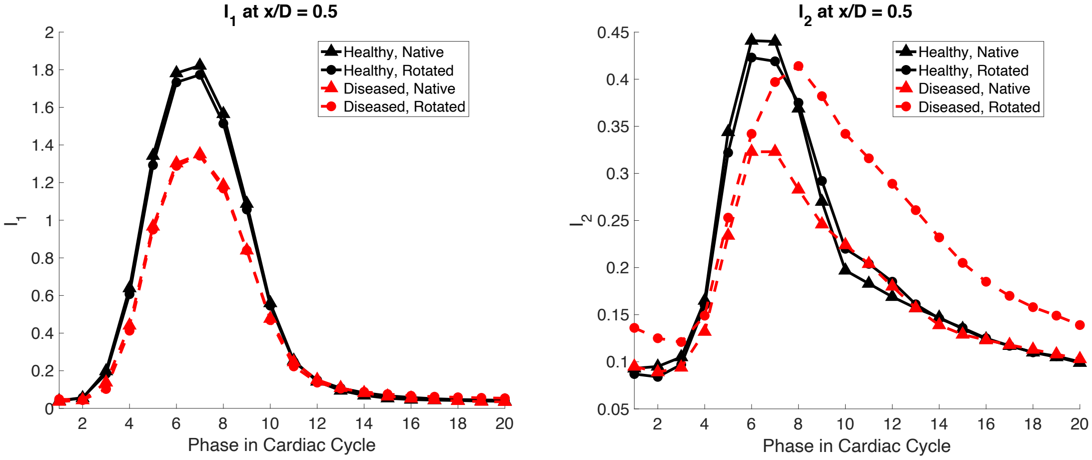

Figure 3.11: Quantitative integral metrics, I_1 (left) and I_2 (right), at axial slice x/D = 0.5.

3.4 Discussion

The analysis of the full 4D flow fields in each of these four cases demonstrated how geometry and valve orientation can drastically impact the hemodynamics in the MPA and local to the bioprosthetic pulmonary valve. Due to the nature of the four cases studied, we can observe the independent effects of geometry by comparing cases with the same valve orientation and the effects of orientation by comparing cases with the same geometry. All four cases together provide insights on how geometry and orientation together might lead to different flow patterns than expected when viewing them in isolation. While the forward flow through the valve had similar features and streamwise momentum in all cases, the reversed and stagnant flow patterns, asymmetry, and strength of secondary flows differed substantially across the cases. In addition, the size and location of vortical structures varied between the two geometries, revealing the complex 3D impact of changing geometry on the flow. Significantly, compound effects of geometry and orientation were observed in the overall flow features, the asymmetry of the reversed flow, and quantitative metrics of secondary flow strengths. Trends that were produced by changing the valve orientation in the healthy geometry were not replicated in the diseased geometry. This indicates that the most favorable placement of the bioprosthetic valve during surgery is likely dependent on the patient's particular anatomy and that a general rule, such as always placing the valve with a specific orientation in every patient, may not lead to optimal outcomes.

While these experiments were performed *in vitro* with generalized geometries, the results provide insight on how valve performance may be impacted by patient anatomy and valve orientation. In particular, the location and volume of reversed flow local to the valve during systole and as it closes likely impact the valve's long-term performance. It has been shown that backward flow towards the valve helps the leaflets close properly (Sacks and Yoganathan, 2007). As noted in 3.3.1, changing the valve orientation in the diseased geometry affected the amount of reversed flow directly impacting the valve leaflets near the annulus. This demonstrates that simply changing the valve orientation during surgery could reproduce potentially favorable flow features in a diseased anatomy.

The asymmetry in the radial velocities in the diseased case and the reversed flow volume in all cases may have an adverse effect on valve leaflet fatigue. In the diseased geometry, there was a strong radial flow over only one of the leaflets during diastole, which may impact that specific leaflet's performance over time in contrast to the other two. If one leaflet is fatigued more than the others, it may lead to incomplete closure and regurgitation or degenerative changes in the valve over time. The reversed flow may also affect leaflet fatigue during closure, but the volume of reversed flow was not the same for all leaflets. In addition, strong reversed flow may lead to regions of recirculation which can lead to clinical complications such as calcification (Sotiropoulos et al., 2016). The rotated orientation, for both geometries, had less asymmetry in the reversed flow than the native orientation (Figure 3.10) which may actually lead to more favorable conditions for long-term valve performance. The flow was not completely symmetric in these rotated orientation cases, however, and the leaflet that was impacted by a larger percentage of the reversed flow varied between the healthy and diseased geometry. In contrast, the healthy and diseased geometry with the native orientation had the same patterns of asymmetry, with bottom left leaflet experiencing a significantly higher volume of the reversed flow than the other two leaflets.

3.4.1 Limitations

While the work in this chapter provides high quality 4D flow data in realistic anatomies under a controlled setting, clinical studies are necessary to determine what flow features in the RVOT and MPA are correlated with early valve dysfunction. Clinical studies to evaluate associations between flow features derived from an imaging technique, such as 4D flow MRI, and long-term outcomes could provide insight into anatomic and flow characteristics that impact bioprosthetic pulmonary valve performance. The analysis used in this work, particularly the integral metrics, could be directly translated to quantify *in vivo* 4D flow MRI data and could ultimately help inform the clinical decision-making process for valve placement.

Additionally, the same 25mm St. Jude Medical Epic bioprosthetic valve was used for all cases in this work. While this allowed for consistency, it did not account for possible variability between different valves of the same model or between different models. Thus, it is possible that some flow features and leaflet behaviors are unique to this particular valve. Also, due to the nature of the experimental set up, this work does not examine the effect of valve fatigue over many heartbeats, which can contribute to long-term valve dysfunction. Future studies should analyze the effects of valve variability on leaflet behavior and flow features in physiological anatomies, as well as how the valve behavior may change due to fatigue over long-term time frames.

While the rigid nature of the 3D printed models allows for easier control of the experiment during 4D flow MRI scanning, this is a significant difference from the material properties of native vessels, which are compliant and flexible. The compliant environment and the movement of the vessels during the cardiac cycle likely impact the flow fields local to the valve. However, the velocities measured in the rigid models still captured key features of the flow and, as both models are made from the same material, the comparisons between them provided valuable insights on the effects of anatomy and valve orientation. We also note that compliance effects are captured by the downstream capacitors in the flow loop, producing physiologic pressure waveforms.

3.5 Conclusions

The flow fields through a bioprosthetic pulmonary valve were analyzed in two generalized physiological geometries of the RVOT and MPA, one healthy and one diseased, with two different valve orientations. Three-component phase-averaged velocity fields were obtained in the 3D printed models using 4D flow MRI. The flow fields for the four cases were qualitatively and quantitatively analyzed to demonstrate compound effects of geometry and valve orientations on hemodynamics that can impact long-term valve performance.

Qualitatively, the additional volume around the valve in the diseased geometry allowed for longer lasting regions of reversed flow, which contributed to strong radial flows across the valve persisting during diastole that could potentially impact the valve leaflets during closure and while they were closed. Changing to the rotated orientation in the diseased geometry made the location of the reversed flow region along the posterior curve of the MPA more similar to the healthy geometry with the native orientation. However, it produced an additional reversed flow region along the anterior curve, illustrating the complicated impact of valve orientation on the full flow field. Quantifying the volume of the reversed flow by individual leaflets demonstrated the asymmetry of the flow. In each case, one leaflet was impacted by a larger percentage of reversed flow than the others, which could result in uneven leaflet fatigue over time. Integral metrics demonstrated that the secondary flow strength was significantly impacted by both geometry and valve orientation. The rotated orientation for the diseased geometry had substantially higher secondary flow strength, indicating more recirculation was present in this case.

There are currently no specific guidelines for the geometric placement of bioprosthetic valves during PVR in ToF based on patient-specific anatomy. However, this experimental work demonstrates the drastic impact that anatomy and valve orientation can both have on valve hemodynamics. The variations in the flow features, asymmetry, streamwise momentum, and secondary flow strength between the two geometries in this chapter illustrate the need for a better understanding of the clinical implications of anatomy-related flow differences, and potentially suggested guidelines, as the same valve placement in different anatomies resulted in significantly different hemodynamics. While these four cases are somewhat generalized and do not encompass the range of geometric features of the RVOT in patients with repaired ToF, it is crucial to understand how patient anatomy and valve placement can substantially affect hemodynamics, which in turn may impact the long-term performance of bioprosthetic pulmonary valves.

Chapter 4

Effects of Cardiac Output

4.1 Background

Pulmonary valve replacements (PVR) are a common reintervention procedure in patients with repaired Tetralogy of Fallot (ToF), typically indicated by pulmonary regurgitation (PR) or pulmonary insufficiency (PI). For ToF patients, the first PVR usually is necessary in adolescence, with multiple reinterventions often needed over a patient's lifetime (Mitropoulos et al., 2017; Kanter et al., 2002; Fuller, 2014). After PVR, most patients experience significant improvements in right ventricle (RV) volume and function and the amount of PR and PI is drastically reduced or eliminated entirely (Bigdelian et al., 2015; Kleinveld et al., 2006; Vliegen et al., 2002).

Bioprosthetic valves are among the most commonly used prostheses for PVR in ToF, since mechanical valves require long-term anti-coagulation therapy, which poses significant risks in children (Batlivala et al., 2012; Chen et al., 2012; Zubairi et al., 2011; Siddiqui et al., 2009). However, most bioprosthetic valves experience structural deterioration and dysfunction over time, often within 15 years of implantation (Siddiqui et al., 2009; McElhinney et al., 2011). In ToF patients, these valves can fail early and unpredictably in as many as 30% of patients (Oliver et al., 2015; Khanna et al., 2015). Some factors that may predispose bioprosthetic valves to early dysfunction and failure in the right ventricular outflow tract (RVOT) have been identified, but they remain poorly understood. Several studies have noted that younger age at the time of PVR can be a predictor of shorter longevity in both bioprosthetic valves and valved conduits (Batlivala et al., 2012; Chen et al., 2012; Zubairi et al., 2011; Oliver et al., 2015; Kwak et al., 2016; Maeda et al., 2021). However, within this younger cohort, it is currently not possible to predict which patients will experience earlier valve dysfunction. In addition, there are no standard surgical techniques proven to prolong bioprosthetic pulmonary valve durability.

Clinical observation reveals a wide range of RVOT anatomies within the ToF patient population (Schievano et al., 2007; Arana et al., 2021). In particular, one of the most common variations is a large dilation in the main pulmonary artery (MPA) local to the valve, as well as other variations in vessel length and angles (Schievano et al., 2007). Previous studies have shown that these anatomic features, as well as the placement of prosthetic valves, alter the hemodynamics of the RV and pulmonary arteries (PAs) from expected flow patterns seen in healthy anatomies (Dasi et al., 2009; Sacks and Yoganathan, 2007; Sacks et al., 2009; Schiavone et al., 2021; Sotiropoulos et al., 2016; Yoganathan et al., 2004, 2005). Thus, understanding how bioprosthetic valve placement in ToF anatomies impacts the hemodynamics local to the valve may provide insights into valve function over time.

Various *in vivo* and *in vitro* techniques are used to measure and analyze flow fields surrounding prosthetic valves. Clinical 4D flow MRI, which uses phase-contrast imaging to obtain velocity fields, has been used in numerous studies examining flow in a range of cardiovascular diseases (Stankovic et al., 2014; Barker et al., 2015; Lawley et al., 2017; Sundareswaran et al., 2012; Schäfer et al., 2018; Sjöberg et al., 2018; Hussaini et al., 2017). This medical imaging technique has been adapted for experimental studies and has been used in both clinical and non-clinical contexts (Elkins and Alley, 2007; Markl et al., 2003; Medero et al., 2018). A review of various experimental techniques, including 4D flow MRI and standard, stereo, and tomographic particle image velocimetry (PIV), in an analysis of flow in an intracranial aneurysm found that all methods captured the global flow structures (Roloff et al., 2019). The use of 4D flow MRI has been validated against PIV and clinical data in various studies (Medero et al., 2018, 2020; Roldán-Alzate et al., 2015; Stankovic et al., 2014; Markl et al., 2012). Previous experimental and clinical studies have used 4D flow MRI to access flow patterns in ToF, but have not specifically examined the effects of valve placement or sizing (François et al., 2012; Jeong et al., 2015; Vliegen et al., 2002; Sjöberg et al., 2018). For assessing valve performance, it is often useful to capture the motion of the valve leaflets in addition to quantifying the surrounding velocity fields. High-speed imaging has been used frequently to visualize the valve leaflets over the cardiac cycle and to calculate various performance metrics including the effective orifice area and leaflet bending stress (Stanová et al., 2020; Hatoum et al., 2018; Salaun et al., 2016). However, high-speed imaging studies have not often been done in conjunction with 3D flow field measurements. We used both methodologies for the studies in this chapter and will demonstrate the benefits of obtaining both velocity fields and high-speed imaging data for the same set of experiments.

4.1.1 Valve Sizing in PVR

Valve sizing is a critical decision during surgery, especially in younger ToF patients undergoing PVR. It is possible that early valve failure may be due to somatic growth, which leads some surgeons to oversize the valve, placing a larger valve than necessitated by the patient's native RVOT size. This open question of valve sizing also arises in the aortic position, where there are widespread variations in the surgeon's choice of valve size (Hatoum et al., 2020; Deeb et al., 2016; Durko et al., 2019). However, the effects of valve oversizing are not fully understood. Clinical studies on both bioprosthetic pulmonary valves and RV to PA valved conduits have found that valve oversizing decreases longevity and is associated with shorter freedom from dysfunction (Batlivala et al., 2012; Chen et al., 2012; Askovich et al., 2007). In addition, a computational study examining three different sizes of valved conduits virtually placed in a healthy pediatric PA found that mean wall shear stress, an indicator for stenosis in these prostheses, was 40% higher at the anastomosis in simulation with the oversized conduit (Sonntag et al., 2015). In studies with stentless aortic valves, valves that were matched with the true patient internal diameter had higher efficiency (Hatoum et al., 2020; Bapat et al., 2014). However, recent studies have demonstrated that large diameter bioprosthetic valves perform well in patients, with valve oversizing not associated with any significant change in time to dysfunction or reintervention (Kwak et al., 2016; Maeda et al., 2021; Karamlou et al., 2005). Therefore, it is still an open clinical question if valve oversizing is helpful for offsetting the effects of somatic growth or if it is actually predisposing bioprosthetic valves to early dysfunction and failure. Despite this, there have been few studies quantifying the flow fields resulting from different choices in valve sizing (Sonntag et al., 2015).

4.2 Experimental Details

All experiments reported in this chapter used the same 25mm valve described in Chapter 3. By changing the cardiac output through the same size valve, these studies correspond to the clinical question of valve sizing. Cardiac output widely varies over the pediatric patient population and generally aligns with patient size: smaller patients have lower cardiac outputs. Thus, when a surgeon places a large valve in a smaller patient, they are generally placing the valve in an environment with lower flow than if it had been placed in an appropriately sized patient. The flow loop was tuned to three different cardiac outputs: 2 L/min, 3.5 L/min, and 5 L/min. The 3.5 L/min case represents the typical flow for a patient with an appropriately sized 25mm valve. The 2 L/min case has lower flow going through the same size valve, which corresponds to valve oversizing in a clinical setting. Similarly, the 5 L/min case has higher flow going through the same size valve, which corresponds to valve undersizing. Though valve undersizing is not common in clinical practice, we studied a range of flow rates to illustrate the overall effects of cardiac output.

The dilated MPA model with the same valve described in Section 3.2 was used for all studies in this chapter. The model and flow loop were used to obtain velocity data using 4D flow MRI and to capture valve leaflet images using high-speed imaging in separate benchtop experiments.

The cardiac output of the flow loop was measured as the time-averaged flow rate at the inflow to the RV box via an ultrasonic flow probe. Various components of the flow loop were adjusted from the 3.5 L/min baseline to obtain the different cardiac outputs. For the 2 L/min case, the duration of the sine squared waveform driving the pneumatic system was decreased. For the 5 L/min case, both the duration and the amplitude of the sine squared waveform were increased. These changes affected the forward air flow into the RV box, which in turn affected the pulsatile flow rate throughout the flow loop. However, while these changes allowed us to capture the correct net flow rate, they adversely affected the pressure waveforms. To account for these changes, we realigned the venting of the pneumatic box with the sine squared waveform to replicate similar dynamics in the driving system across all cases. In addition, we increased the downstream capacitance for the 5 L/min case and decreased the capacitance for the 2 L/min case. In order to maintain a similar pressure waveform shape across all cases, the length of systole varied slightly depending on the cardiac output. Systole was approximately 33% of the cardiac cycle for the 2 L/min case, 38% of the cardiac for the 3.5 L/min case, and 41% of the cycle for the 5 L/min case. The adjustments to the system resulted in physiological flow and pressure waveforms for each case, as seen in Figure 4.1. Overall, we generated similar dynamics for each cardiac output, allowing for the most direct possible comparison between all three cases.

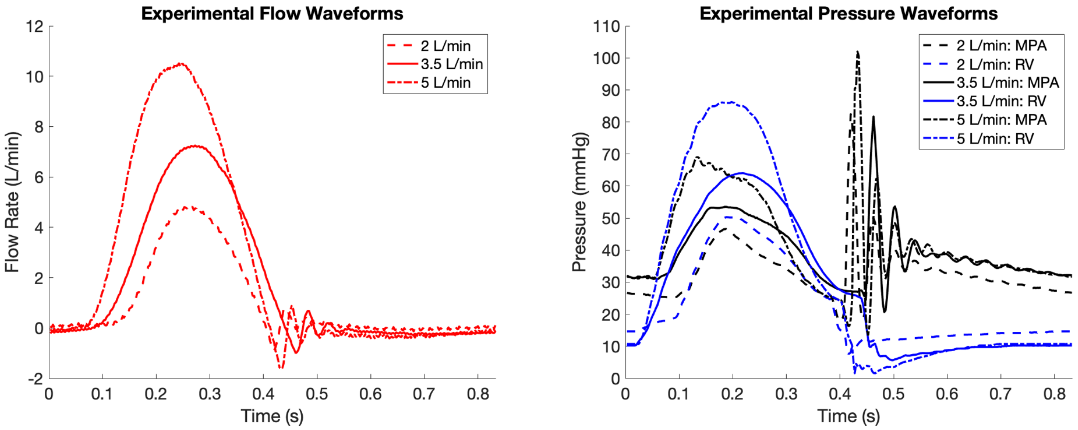

Figure 4.1: Experimental flow (left) and pressure (right) waveforms in the model for each of the three cardiac output cases. Flow waveforms were measured in one of the outlet PA branches. Flow and pressure data were taken simultaneously for each case.

4.2.1 4D Flow MRI Experiments

To analyze the effects of cardiac output and valve orientation, we conducted five different 4D flow MRI experiments. We ran the flow loop with cardiac outputs of 2 L/min, 3.5 L/min, and 5 L/min with the valve in the native orientation. For the rotated orientation, we only ran the 2 L/min and 3.5 L/min cases, since 2 L/min represents the more clinically relevant case of valve oversizing.

The scan procedure and sequence settings for the MRI were nearly identical across all experiments, which are described in Section 2.1.2. The VENC was only parameter that was changed, since changing the cardiac output results in different maximum velocities for all three cases. The VENC in each case was set to the same value in the sagittal, axial, and coronal directions. The VENC was set at 150 cm/s for the 2 L/min case, 250 cm/s for the 3.5 L/min case, and 350 cm/s for the 5 L/min case.

We calculated the SNR and velocity uncertainty for each case. The velocity uncertainty is given as the percent of the mean velocity through the valve opening at peak systole. As reported in Section 3.2, the average SNR for the 3.5 L/min cases was 21, resulting in an uncertainty of 6.3%. For the 5 L/min case, the SNR was 18, resulting in an uncertainty of 7.6%. The average SNR in the two 2 L/min cases was 19.5, resulting in an uncertainty of 6.2%.

4.2.2 High-Speed Imaging Experiments

For the high-speed imaging experiments, the flow loop was assembled on the benchtop exactly as it was in the MRI scanner. Though the high-speed imaging and the 4D flow MRI experiments are not conducted simultaneously, they both use and record the same trigger signal for the pulsatile cardiac cycle. Thus, we can precisely align the data from the two experimental methods. We obtained high-speed images of the valve leaflets for the three cardiac outputs with the valve in the native and rotated orientation for each case.

In order to have clear optical access to the valve, we printed a new downstream component for the MPA and branch PAs of the model. The internal geometry of the model was identical, but we reduced the wall thickness to 2mm and polished the surface to remove distortions due to the printing process. In order to eliminate refraction from the surrounding air to the working fluid in the model, we built an external box to submerge the model. The box was designed to align with outlet angles of the LPA and RPA and was sealed around the model using the tubing extending from these branches and the flange of the 3D printed valve-holder component. During the high-speed imaging experiments, the box was filled with the working fluid, thus submerging the model. This box did not affect any of the working settings of the flow loop and can be seen in Figure 4.2, indicated by the black arrow.

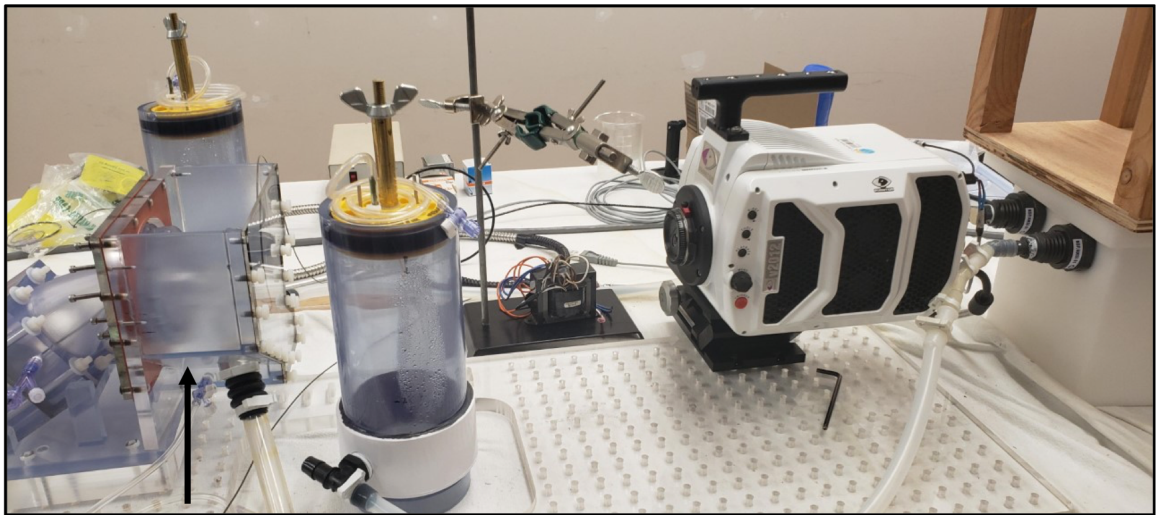

Figure 4.2: The experimental flow loop assembled on the benchtop for high-speed imaging. The Phantom V2012 Ultrahigh-speed camera on the right was aligned head-on with the valve in the model in order to capture images of the leaflet motion. The model was submerged in the working fluid to eliminate refraction effects using the box indicated by the black arrow.

We captured images of the valve leaflets over the cardiac cycle using a Phantom V2012 Ultrahigh-speed camera with a 105mm Nikkor lens. We imaged the valve leaflets head-on from downstream, as seen in Figure 4.2. We took images at a frame rate of 1500 Hertz with a 500 microsecond exposure in order to capture the instantaneous valve leaflet motion. This frame rate resulted in approximately 409 frames during systole for the 2 L/min case, 476 frames during systole for the 3.5 L/min case, and 514 frames during systole for the 5 L/min case. We used an f-stop of 11 to allow for a large enough depth of field to keep the leaflets in focus as they open. A ring light was placed on the outside of the submersion box, positioned with the valve centered in the ring, to provide lighting for high quality imaging.

In order to calibrate the images, we built a calibration target with a grid of 69 evenly spaced points that fit into our model in the valve-holder component. The target was set at the location where the leaflets edges meet in the center of the valve, which we used as our focus point. With the model and the submersion box filled with the working fluid, we focused the lens and took an image of the calibration target, shown in Figure 4.3. Using the known distance of 2.6mm between each point on the calibration target, we calculated a conversion factor for our images of 0.00181mm^2 per pixel. This results in approximately 580 pixels across the diameter of the valve, which allows us to accurately observe small-scale movements in the leaflets. Since the points on the target were in a Cartesian grid, we also used the target to reduce the distortion in the images caused by curved edges of the model with an in-house MATLAB code.

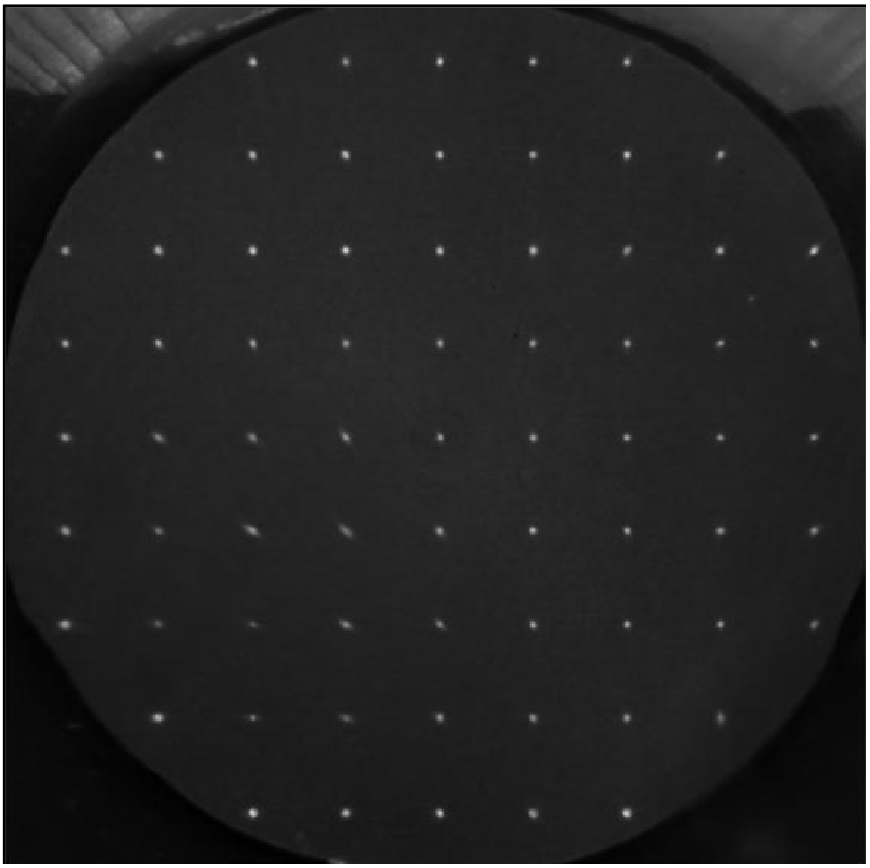

Figure 4.3: An image of the calibration target taken with the Phantom V2012 Ultrahigh-speed camera. The known distance between the grid point was used to calibrate the image pixel locations.

4.3 Results

Results are presented for the three cardiac output cases: 2 L/min, 3.5 L/min, and 5 L/min focusing first on the qualitative and quantitative results from the 4D flow MRI experiments. Then we examine valve leaflet behavior with the high-speed imaging experiments and the relationship between leaflet motion and the full velocity fields.

4.3.1 4D Flow MRI Results

There were a number of similar flow features across the three cardiac outputs with the valve in the native orientation. In all three cases, the forward flow jet through the valve had an almost triangular shape with three tips, which was clearly seen in axial slice x/D = 0.5 at peak systole in Figure 4.4. Axial slice x/D = 0.5 is immediately downstream of the valve support structure. The jet generally followed the same angle and path out of the valve in all cases, as observed in the sagittal slice through the center of the vessel. In addition, the normalized streamwise velocities were similar for each cardiac output, indicating that the relative strength of the jet compared to the inflow upstream of the valve was mostly independent of the actual cardiac output.

However, despite these general similarities, there were key differences in the flow fields for each case. With a trileaflet valve, 120 degree symmetry would be expected in the flow through the valve, but this was not always the case. The forward jet shape was the most symmetric in the 5 L/min case, with each of the jet tips extending approximately the same distance away from the center of the vessel. The 3.5 L/min had more notable asymmetry as each of the jet tips had a unique shape, as observed in the axial slice x/D = 0.5. The jet asymmetry was the most pronounced in the 2 L/min case, as the jet tip in the bottom left was significantly elongated and narrowed. These characteristics were observed in the 3D shape of the forward flow as well as the axial and sagittal slices, as demonstrated in the velocity isosurfaces in Figure 4.5. The three wide dips in the green isosurface between the jet tips indicated where the valve leaflets opened, as the flow passed through them out of the valve annulus.

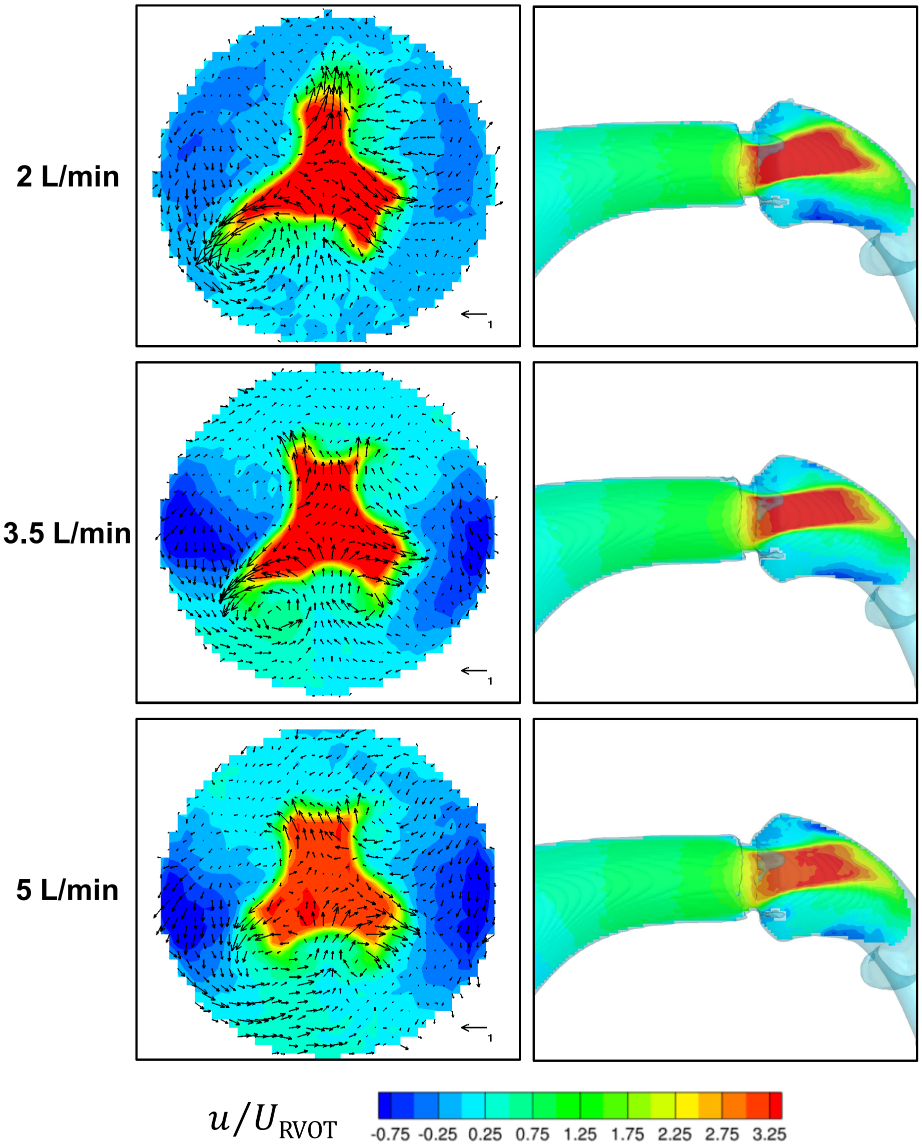

Figure 4.4: For cardiac outputs of 2 L/min (top), 3.5 L/min (middle), and 5 L/min (bottom), X-component of velocity contours normalized by the peak speed in the RVOT upstream of the valve. Contours shown at axial slice x/D = 0.5 (left column) and sagittal slice z = 0 (right column) at peak systole. In-plane velocity vectors are shown on the axial slice with a reference vector representing a normalized velocity of 1.

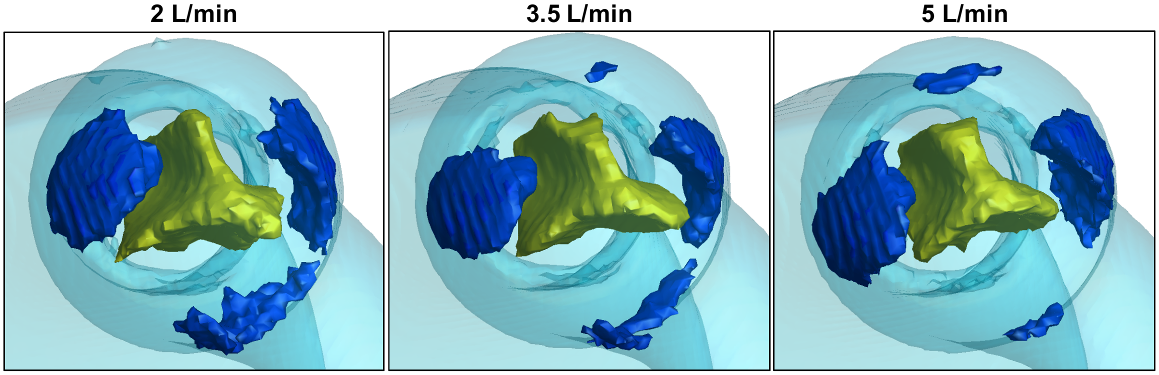

Figure 4.5: Velocity isosurfaces at peak systole for 2 L/min (left), 3.5 L/min (middle), and 5 L/min (right). The green and dark blue represent x-component of velocity isosurfaces at $u/U_{RVOT} = 2.5$ and $u/U_{RVOT} =$ -0.5 respectively. Differences across all 3 cases can be seen in the shape of the forward flow jet and in the size and location of the reversed flow regions.

In the 2 L/min case, a strong vortex shed off the leaflet that bordered the narrowed asymmetric portion of the jet, as seen in the in-plane velocity vectors (Figure 4.4). There was recirculation present in a similar region in the 3.5 L/min case, but it was not as pronounced, and the 5 L/min case only had limited recirculation surrounding the forward jet. The location and size of the reversed flow regions also differed across the three cases. In the sagittal slices, we can see a region of reversed flow along the interior curve in each case. In the 2 L/min case this reversed flow formed fairly close to the valve annulus, while it was located further downstream in the 3.5 L/min and 5 L/min cases. In addition, in both the axial slices and the 3D isosurfaces of reversed velocity, we can see that the total volume of reversed flow was largest in the 2 L/min case. In the 5 L/min case, the reversed flow region along the interior curve of the vessel was noticeably smaller than the other two cases, in addition to being further downstream. However, there was a region of reversed flow above the forward jet in the 5 L/min case, and to a lesser extent in the 3.5 L/min case, that was not present in the 2 L/min. These differences in the flow features depending on cardiac output have clinical relevance, as increased recirculation and reversed flow have both been linked to valve complications such as calcification (Yoganathan et al., 2005; Sotiropoulos et al., 2016).

The x-component of vorticity at peak systole illustrated additional flow features, as seen in contours on an axial slice that includes the valve leaflets and support structures at x/D = 0.25 (Figure 4.6). The x direction aligns with the streamwise flow and is normal to the valve annulus. Opposite sign vortices developed on the edges of each leaflet as the flow passed through. For example, in the axial slices in Figure 4.6, a leaflet sits between the structural valve supports represented by the light blue surfaces. For the leaflet in the bottom left, negative x vorticity developed on one edge of the leaflet and positive x vorticity developed on the other. This pattern was observed on all leaflets in all three cardiac output cases. These vortices aligned with the in-plane velocity vectors in each case. In the 2 L/min case, the stronger recirculation corresponded to a larger region of positive x vorticity. The 5 L/min case had weaker vorticity regions along the leaflets but had stronger vorticity on the outer edge of the valve supports, particularly along the outer curve of the vessel. This may indicate that the faster flow through the valve excited more of the fluid in the dilated anatomy. These variations in x vorticity demonstrate how cardiac output has a substantial impact on complex flow features in the RVOT model.

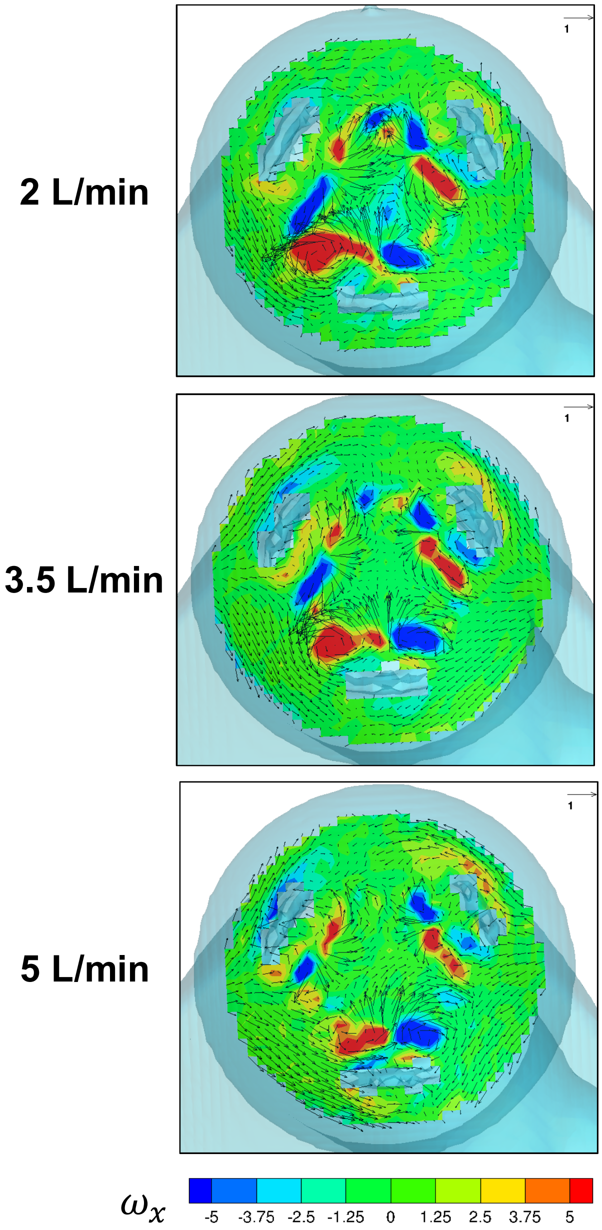

Figure 4.6: Contours of the x-component of vorticity (ω_x) with in-plane velocity vectors at axial slice x/D = 0.25 for the 2 L/min (top), 3.5 L/min (middle), and 5 L/min (bottom) cases with native valve orientation at peak systole. The transparent light blue surface represents the wall of the model and the three structural supports of the valve, which cut through the axial contour slices.

Changing the valve orientation in addition to the cardiac output had compound effects on the hemodynamics. In the rotated orientation, the valve was rotated 180 degrees from the native orientation. The jet shape at systole, as observed in an axial slice, rotated 180 degrees as well which can be seen when comparing the velocity contours for the native orientation in Figure 4.4 and the rotated orientation in Figure 4.7 for the 2 L/min and 3.5 L/min cases. In particular, the 2 L/min case with the rotated orientation still had an asymmetric jet, with strong recirculation along the narrowed jet now in the upper right region of the vessel. However, while the forward flow rotated accordingly with the valve orientation, the reversed flow regions at systole did not. In the native orientation, the large reversed flow regions formed mostly along the sides of the vessel. In the rotated orientation, the reversed flow regions were located along the inner and outer curves of the vessel. The sagittal slices illustrated the likely cause of this shift. In the rotated orientation, the jet through the valve annulus is directed towards the center of the vessel, away from the outer wall (Figure 4.7). This led to a large reversed flow region forming along that outer wall that was not present in the native orientation cases. Thus, changing the valve orientation drastically shifted the location and volume of reversed flow in both the 2 L/min and 3.5 L/min case.

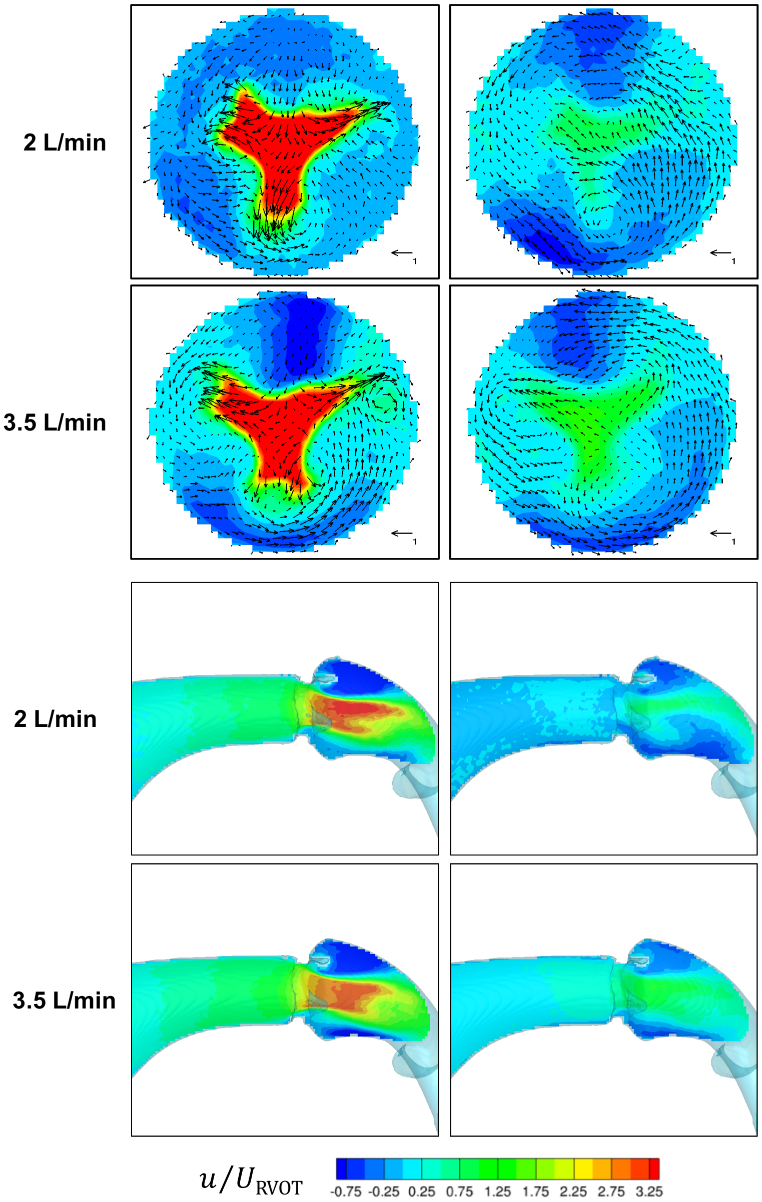

Figure 4.7: Normalized streamwise velocity contours for the 2 L/min (first and third rows) and 3.5 L/min cases (second and fourth rows) in the rotated valve orientation. The top block of four images are velocity contours shown at an axial slice x/D = 0.5 with in-place velocity vectors. The bottom block of four images are velocity contours shown at a sagittal slice z = 0. Velocity contours are shown at peak systole and during diastole as flow is decelerating.

The 2 L/min case with the rotated orientation presented a unique flow feature over the cardiac cycle that was not present in any other experiment in this study. In this case, a strong region of recirculation formed during systole along the inner curve of the vessel at one of the jet tips. This contrasted with the 3.5 L/min rotated case, which did not have this recirculation. Instead, the 3.5 L/min case had a strong counterclockwise swirling flow along the inner curve that persisted into diastole. The recirculation in the 2 L/min case appeared to break up that swirling effect that might have otherwise been present. As a result, the reversed flow along the outer curve, as observed in the sagittal slices, became detached from the wall in diastole for the 2 L/min case. This produced a more complex flow field in the center of the vessel and leaflets, with reversed flow potentially impacting the point of valve closure. Increased recirculation and shifting reversed flow location may produce a hemodynamic environment more prone to leaflet calcification and fatigue that is only present in the 2 L/min case with the rotated orientation.

The radial velocities in the flow field local to the valve directly impact the valve leaflets during opening and closure. Figures 4.8 and 4.9 demonstrate the radial velocities close to the valve leaflets at three different time points during the cycle: peak systole, the middle of diastole as the streamwise flow is decelerating, and towards the end of diastole when the streamwise flow has settled to rest. At systole, all cardiac output and valve orientation cases experienced similar flow structures. Flow moved toward the center of the vessel between the open edges of the valve leaflets, as demonstrated by the blue velocity contours. Simultaneously, the opening surface of the leaflets pushed flow towards the outer wall of the vessel, resulting in the red radial velocity contours. The native and rotated orientations had similar flow structures, with the patterns rotated as they aligned with the location of the valve leaflets. However, after systole, the flows differed depending on both cardiac output and valve orientation. During mid-diastole in the rotated orientation, both the 2 L/min case and 3.5 L/min case had radial flow towards the vessel center mostly across the leaflet on the inner wall (the bottom of the axial slice) (Figure 4.9). This corresponded with the reversed flow regions seen in the axial and sagittal slices during diastole (Figure 4.7). Fluid was flowing back towards the valve annulus along both the inner and outer walls of the vessel. When it encountered the closed valve, it washed over the bottom leaflet towards the center of the vessel as radial flow. The radial flow on the top of the valve had significantly less strength since it was blocked by the valve support structure. Towards the end of diastole, the radial flow became stagnant in both the 2 L/min and 3.5 L/min cases with the rotated valve orientation.

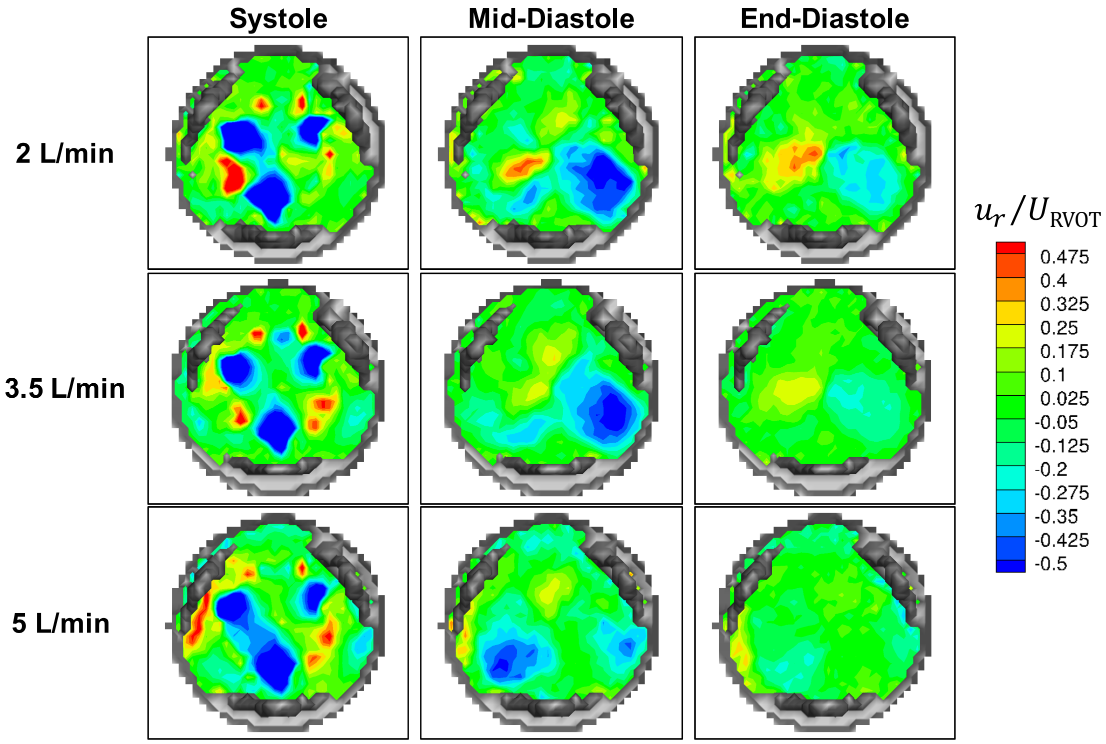

Figure 4.8: Radial velocity contours computed from the normalized velocity components for the native valve orientation for the 2 L/min case (top row), 3.5 L/min case (middle row), and 5 L/min case (bottom row). Contours shown at an axial slice x/D = 0.11, local to the valve annulus for three different time points: peak systole (left column), mid-diastole (middle column), and towards the end of diastole (right column). The structure of the valve is shown in gray.

The radial flow patterns in diastole for the native orientation were substantially different than those for the rotated orientation. In the 2 L/min case at mid-diastole, the radial flow moved across the closed valve from bottom right towards the center of the vessel (blue velocity contour) and then away from the center towards the bottom left region of the vessel (red velocity contour) (Figure 4.8). The flow pattern towards

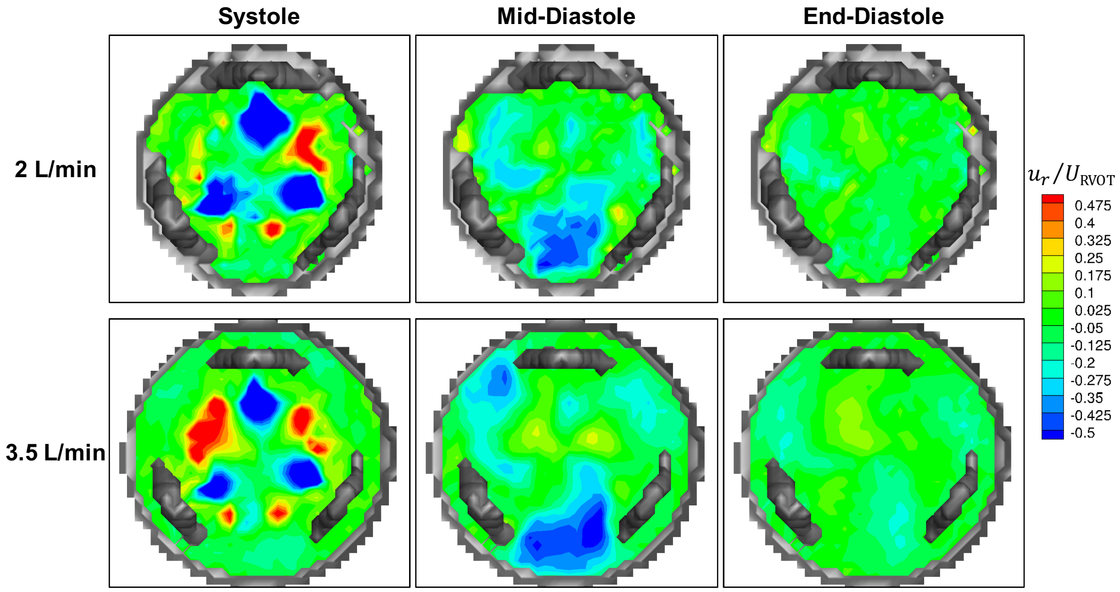

Figure 4.9: Radial velocity contours computed from the normalized velocity components for the rotated valve orientation for the 2 L/min case (top row), and 3.5 L/min case (bottom row). Contours shown at an axial slice x/D = 0.11, local to the valve annulus for three different time points: peak systole (left column), mid-diastole as the streamwise flow is decelerating (middle column), and towards the end of diastole when the streamwise flow has settled to rest (right column). The structure of the valve is shown in gray.

the center of the vessel was also seen in the 3.5 L/min case, though the radially outward flow was significantly weaker. In the 5 L/min case at mid-diastole, flow moved towards the center of the vessel from both the bottom right and bottom left regions. Towards the end of diastole, when the streamwise flow had settled to rest, the radial flow in the 5 L/min case was also stagnant. In the 3.5 L/min case, the flow was nearly stagnant, with some slight remnants of the flow patterns seen at mid-diastole. However, in the 2 L/min case, there was still a notable amount of radial flow washing over the valve leaflets. It is possible that larger volume of reversed flow led to this persistent radial flow throughout diastole, as more fluid flowed back towards the closed valve. This may have an adverse effect on valve performance, as continuous flow impacting the leaflets over the cardiac cycle may increase the rate of fatigue.

To quantify the streamwise momentum and secondary flow strength of the flow fields, we calculated the integral metrics I_1 and I_2 that were introduced in Section 3.2.1 for each of the cardiac output experiments over the cardiac cycle (Figure 4.10). I_1 was calculated using Equation 3.2 for the axial cross-sections at x/D = 0.25 and x/D = 0.5. I_2 was calculated using Equation 3.3 at the same cross-sections. For each case, the average velocity over a cross-section immediately upstream of the valve at peak systole was calculated for the reference area. The cross-sectional area was calculated for each of the axial locations and was the same for all experiments since the same model was used.

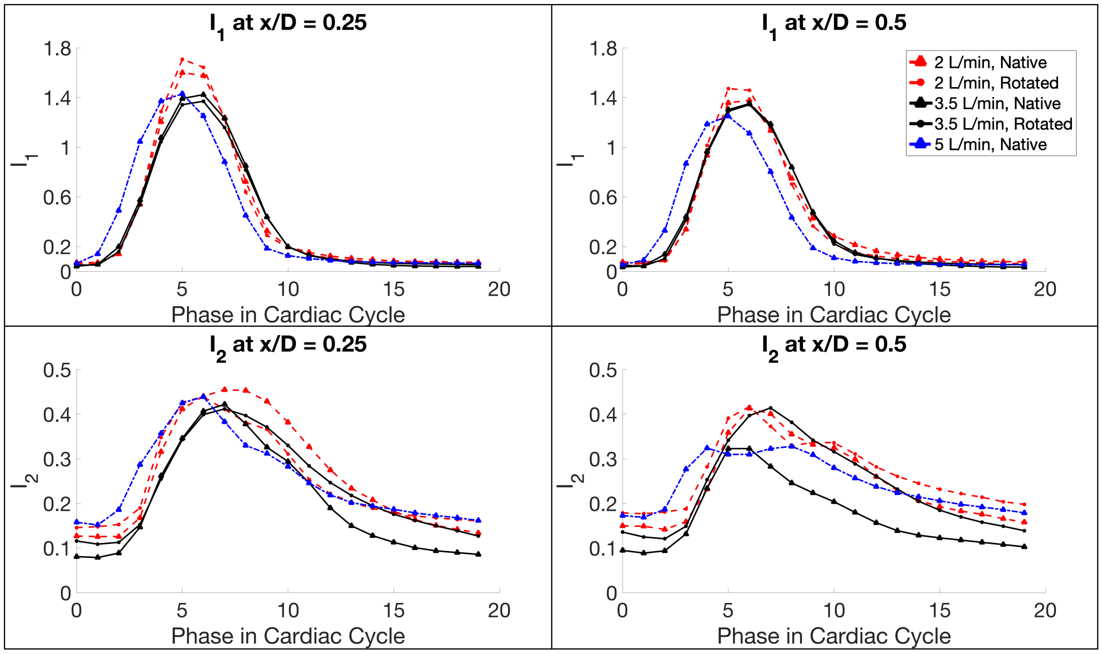

Figure 4.10: Quantitative integral metrics I_1 (top row) and I_2 (bottom row) at two axial slices, x/D = 0.25 (left column) and x/D = 0.5 (right column) for three cardiac outputs. The legend in the top right corner applies to all plots.

The cross-sectional slice x/D = 0.25 is approximately midway along the valve support structures and the valve leaflet edges extend to this point when they are fully open during systole. At this slice, the streamwise momentum I_1 was approximately the same for the 3.5 L/min case with both orientations and the 5 L/min case (Figure 4.10). The streamwise momentum for the 5 L/min case peaked at an earlier phase because that was when peak systole occurred for the 5 L/min case flow rate waveform.

Otherwise, the I_1 values for these cases were very similar, with I_1 exceeding 1 during systole indicating high momentum flow and decreasing to 0 when the streamwise flow stagnates during diastole. The 2 L/min cases for both valve orientations followed a similar pattern over the cardiac cycle, but peaked at a higher value of I_1 during systole. One possible explanation for the higher streamwise momentum in the 2 L/min cases is that the valve leaflets did not open as fully due to the slower cardiac output through the 25mm valve. The flow through the narrowed valve opening would be faster and result in higher relative streamwise momentum in this case. We observed that the valve opening area was less for the 2 L/min cases than the others with the high-speed imaging, as discussed later in Section 4.3.2, indicating that this was likely the cause for the higher streamwise momentum in these cases.

The cross-sectional slice x/D = 0.5 is immediately downstream of the entire valve support structure. At this slice, I_1 had similar patterns and relationships across cases as I_1 at x/D = 0.25 (Figure 4.10). For all cases, I_1 was decreased at x/D = 0.5 due to the flow losing momentum as it moved downstream. I_1 for the 2 L/min cases was still slightly higher than the other cases. For all cases at this slice, the streamwise momentum peaked above 1 during systole and decreased to 0 during diastole. For both x/D = 0.25 and x/D = 0.5, there were only slight differences between the native and the rotated orientation for the 2 L/min and 3.5 L/min cases, indicating that valve orientation had little impact on the streamwise momentum.

For the secondary flow strength I_2 at x/D = 0.25, all of the cases had similar peak values, with the 3.5 L/min cases on the lower side at 0.4 and the 2 L/min native orientation case at the highest value of 0.45 (Figure 4.10). In the 2 L/min native orientation case, I_2 was sustained close to its peak value for longer in the cardiac cycle than the other cases. This higher I_2 value with longer duration corresponded to larger region of x vorticity that occurred in this case (Figure 4.6). For 2 L/min, the native orientation had higher I_2 after systole than the rotated orientation, while the opposite was true for the 3.5 L/min cases. This highlights the compound influence of cardiac output and valve orientation; the effect of changing the valve orientation depends on the flow rate. At x/D = 0.5, both 2 L/min cases and the rotated orientation for the 3.5 L/min case had nearly the same I_2. For the 5 L/min case at x/D = 0.5, there is no clear peak, but rather a consistent secondary flow strength over the entirety of systole. The rotated orientation for the 3.5 L/min case had a strong counterclockwise swirl at this axial location, differentiating it from the native 3.5 L/min case (Figure 4.7). The higher value of secondary flow strength quantified this difference. Both of the 2 L/min cases had strong recirculation regions along the forward flow jet which contributed to the higher I_2 values. It is worth noting that the differences in I_2 at the beginning and end of the cardiac cycle, when the flow is essentially stagnant, are likely due to differences in the noise floors in the secondary flows across cases as opposed to physical differences in the flows.

4.3.2 High-Speed Imaging Results

We analyzed valve leaflet behavior with high-speed imaging experiments for all three cardiac outputs and two valve orientations for each case. From the 2D images of the valve, we calculated the opened area between the valve leaflets, or orifice area, over the cardiac cycle. For each case, we captured images for 48 cardiac cycles, calculated the projected 2D orifice area in each image by counting the pixels inside the leaflet edges, and averaged the area over all cardiac cycles (Figure 4.11). The orientation of the valve did not significantly impact the maximum orifice area during peak systole, though it did have slight effects on the timing of valve opening and closure. The 5 L/min cases had the highest orifice area, indicating that these cases made the most efficient use of the valve. The 3.5 L/min cases had a 4.5% lower orifice area and the 2 L/min cases had a 8.9% lower orifice area than the 5 L/min cases. With the same 25mm valve, the lower cardiac outputs were not sufficient to fully open the leaflets.

The valve leaflets were highly flexible and their free edges fluctuated the entire time they were open. While the leaflet motion varied slightly from cycle to cycle, there were some key features of the leaflet behavior that differentiated the cases. For example, two critical differences between the 2 L/min and 3.5 L/min cases with native valve orientation are highlighted in the white boxes in Figure 4.12. For these regions, the 5 L/min case was qualitatively similar to the 3.5 L/min case. The top white box focuses on an area where the leaflet free edges meet at the commissure. In

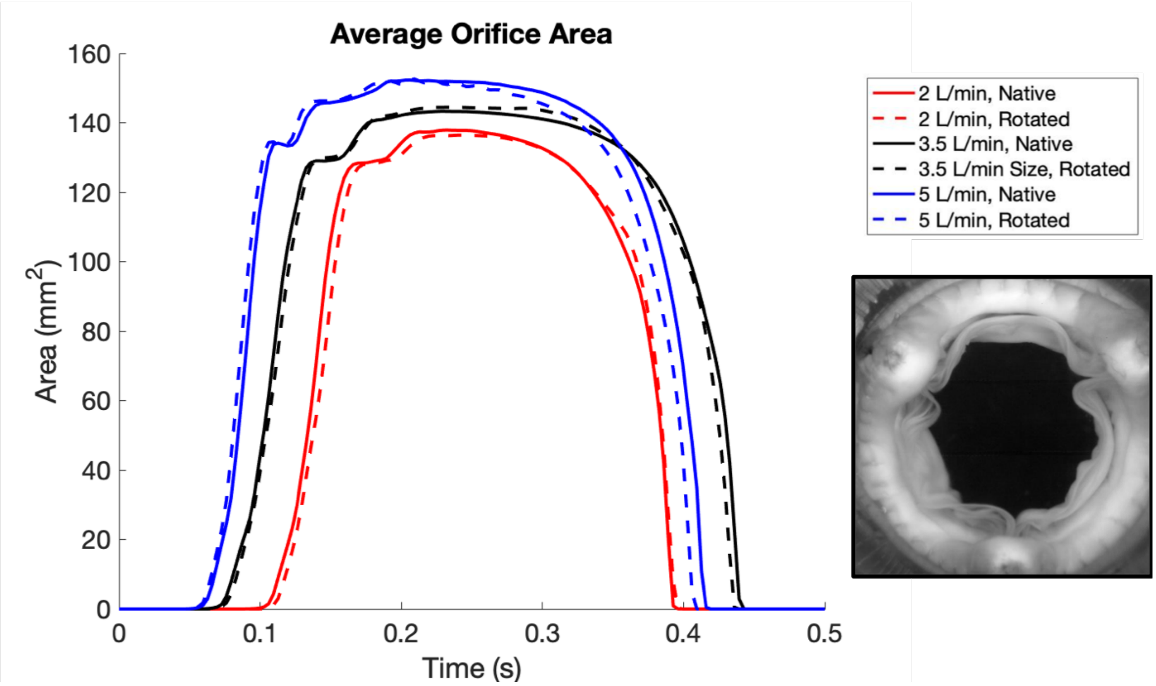

Figure 4.11: Average orifice area for three cardiac outputs and two valve orientations over the systolic portion of the cardiac cycle. Orifice area was calculated as the projected area between the open valve leaflets in the 2D valve image (example shown in bottom right inset).

the 3.5 L/min case, the leaflet edges fully separated, pushed open by the incoming flow. However, in the 2 L/min case, the leaflet edges remained in contact through the cardiac cycle. This contact can adversely affect the valve performance, as leaflet edges close together at the commissure may calcify more easily, leading to valve dysfunction. In the bottom white boxes, we observed a difference in the shape of one of the leaflets. While this section of leaflet did not fully open to the outside of the valve in the 3.5 L/min case, it came closer than it did in the 2 L/min case. With a cardiac output of 2 L/min, this section of leaflet remained in an open bowl-like shape, which obstructed the flow coming through the annulus and provided an area where flow could recirculate and stagnate, even during systole.

These observations of the valve leaflet behavior are useful on their own, as they demonstrate which cases result in valve motion that might be more prone to dysfunction. However, we also can couple the high-speed imaging with our 4D flow MRI

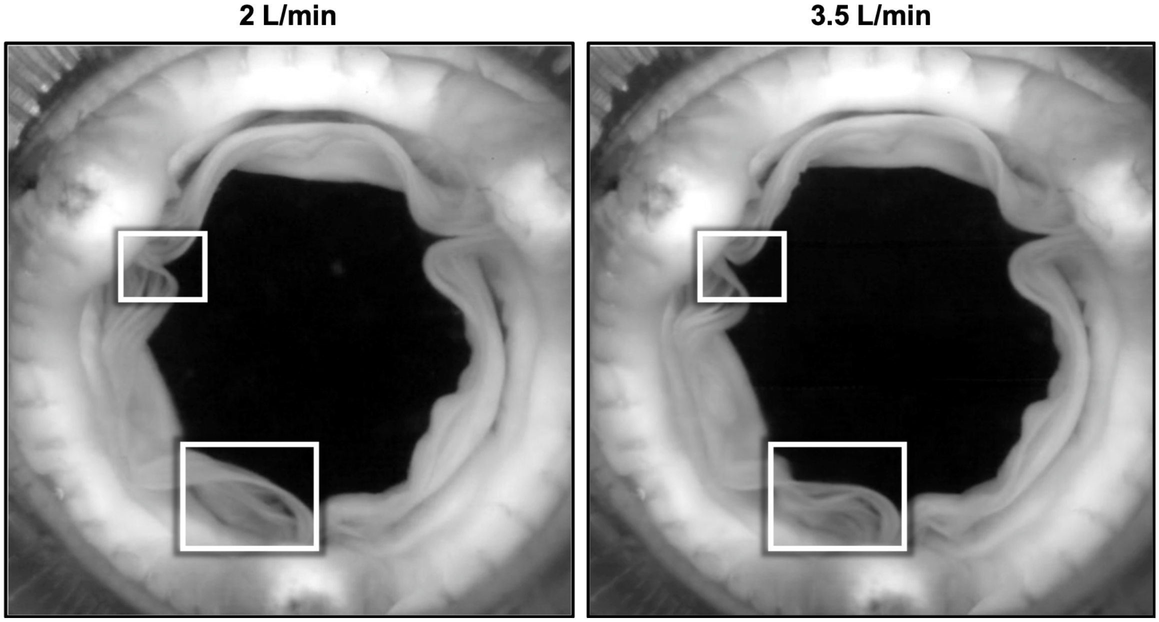

Figure 4.12: Valve leaflet images from the high-speed imaging experiments for the 2 L/min case (left) and the 3.5 L/min case (right). The white boxes highlight differences in leaflet behavior between the two cases.

results to fully examine the relationship between valve behavior and flow patterns. Key examples of this relationship are shown for the 2 L/min case for the native and rotated orientation in Figure 4.13. For the native case, the leaflet that we observed obstructing the flow in Figure 4.12 directly corresponded to the region of strong recirculation in the 4D flow MRI data. The flow from the 2 L/min cardiac output was not fast enough to fully open the leaflet, which led to adverse hemodynamics in the velocity field. This behavior also occurred in the 2 L/min case with the rotated valve orientation. The two white boxes in the bottom row of Figure 4.13 show two areas where valve leaflets did not open fully. This directly corresponded to the narrowed jet region in the velocity data, as well as another region of recirculation. These hemodynamic features can contribute to increased risk of calcification and uneven leaflet fatigue due to asymmetry.

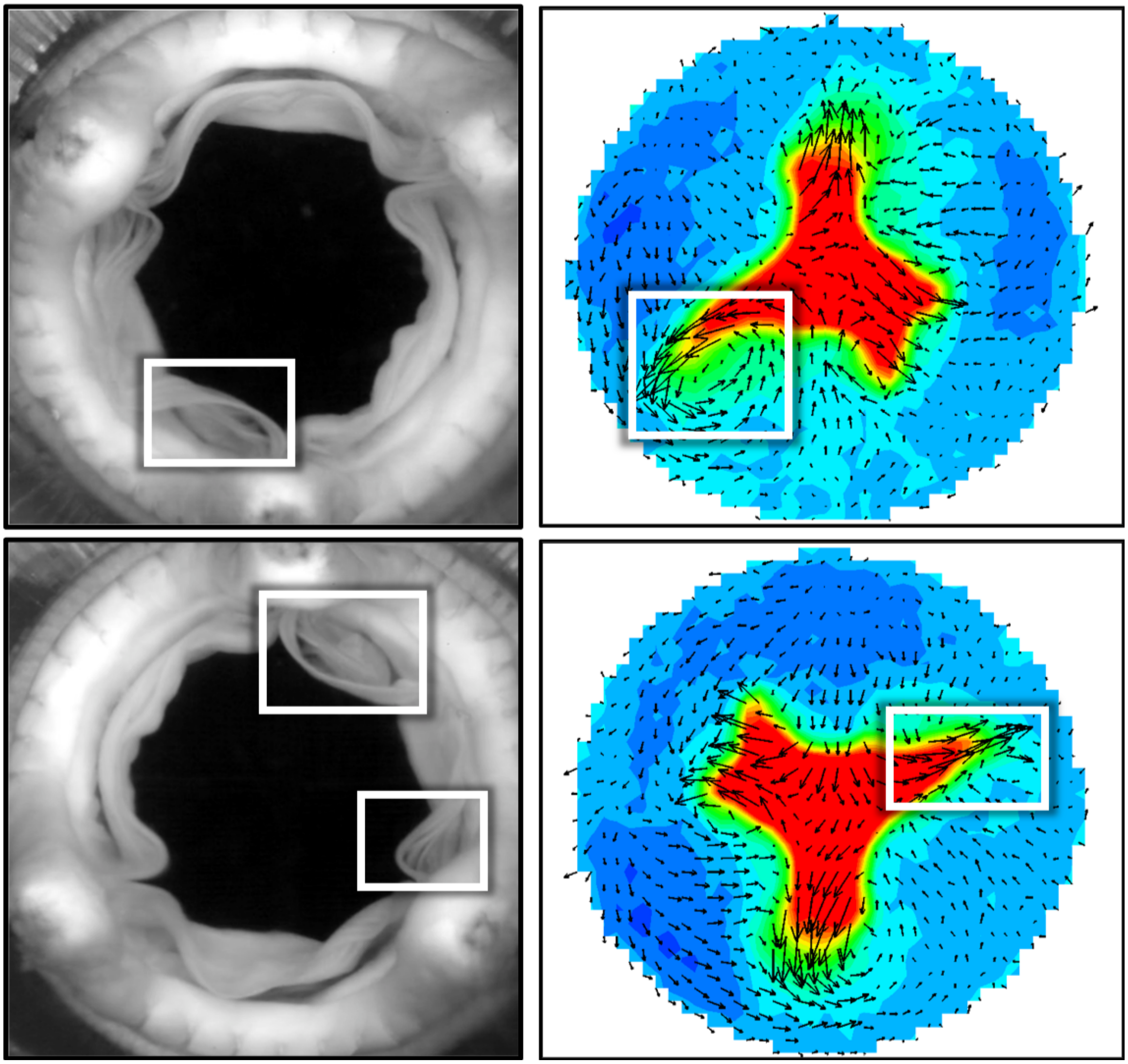

Figure 4.13: Valve leaflet images compared to velocity contours for the 2 L/min case with the native valve orientation (top row) and rotated valve orientation (bottom row). The white boxes highlight regions where the leaflet behavior observed in the high-speed imaging experiments align with strong recirculation in the velocity fields obtained by 4D flow MRI.

4.4 Conclusions

The analysis of full 4D flow fields and instantaneous valve leaflet images demonstrated how both cardiac output and valve orientation can impact hemodynamics in the RVOT and leaflet performance. The general shape of the jet through the valve and the relative velocity of the jet compared to the upstream inflow were similar across cardiac outputs of 2 L/min, 3.5 L/min, and 5 L/min. However, there were key differences in the asymmetry of the jet, the amount of recirculation, and the location and size of reversed flow regions (Figure 4.4). The 5 L/min case had the most symmetric jet and the lowest volume of reversed flow. Conversely, the 2 L/min case had an asymmetric jet with a strong region of recirculation along the narrowed branch of the jet. This recirculation corresponded to a larger region of positive x vorticity in the 2 L/min case, though all three cases had similar vortical structures as two vortices of opposite sign shed off of each valve leaflet (Figure 4.6).

In the 2 L/min and 3.5 L/min cases with the rotated valve orientation, the forward flow jet rotated 180 degrees, following the valve rotation. However,the reversed flow regions drastically differed from the native orientation cases. In particular, the 2 L/min rotated case had increased recirculation along the inner curve of the vessel, which contributed to the reversed flow detaching from the wall and impacting the valve leaflets during diastole. These unique flow features emphasized the compound effect of cardiac output and valve orientation. Both of these factors can have a crucial impact on hemodynamics and trends observed from changing valve orientation in one case were not necessarily replicated with a different cardiac output. These compound effects were also quantified in the integral metric I_2 (Figure 4.10). At axial slice x/D = 0.5, the 2 L/min cases with both the native and rotated orientation had similar secondary flow strengths, while the rotated 3.5 L/min case had substantially higher secondary flow strength than the native 3.5 L/min case. Thus, the effect of valve orientation on secondary flow strength depended on the cardiac output. These results support the similar conclusion on the compound effect of RVOT anatomy and valve orientation discussed in Chapter 3.

High-speed imaging experiments provided insights on the valve leaflet behavior with different cardiac outputs. We used the images to measure the valve orifice area and noted that the 2 L/min cases had 8.9% lower area than the 5 L/min cases. Orifice area is used extensively in clinical settings, particularly with aortic valves, to assess performance of prosthetic valves; lower orifice area indicates a less efficient valve (Bech-Hanssen et al., 2001; Garcia et al., 2004; Shadden et al., 2010). In addition to the orifice area calculations, the combination of our 4D flow MRI and high-speed imaging methods provided a more complete picture of the valve environment. In several instances with the 2 L/min cases, we observed leaflet sections that did not open fully during systole directly corresponded to areas of strong recirculation in the velocity data. These connections, in addition to providing insight on valve performance, indicate that it is possible to infer valve leaflet behavior from flow fields. This relationship would be useful for *in vivo* settings where it is possible to obtain velocity data, but not possible to directly observe leaflet motion.

We found that the 2 L/min cases had numerous adverse features in the flow fields and valve behavior. The 2 L/min cases had strong recirculation, which is associated with calcification, large reversed flow volumes, which may lead to hemolysis, persistent radial flow during diastole, which may contribute to leaflet fatigue, lower valve orifice area, and locations where the valve leaflet edges did not separate, which are more prone to fusion and calcification (Yoganathan et al., 2004, 2005; Sotiropoulos et al., 2016). As discussed earlier in Section 4.2, a cardiac output of 2 L/min through a 25mm valve corresponds to the clinical decision of valve oversizing. While the effects of this practice are still an open question, our results strongly suggest that valve oversizing produces a hemodynamic environment that would predispose the valve for failure. Alternatively, we found that the 5 L/min case, which corresponds to valve undersizing, had fewer adverse flow features and the highest orifice area in our cases. While there are a number of clinical reasons to avoid undersizing the valve, including needing to account for patient growth, our results indicate that the hemodynamics of this configuration are comparable or even favorable to the standard sizing.

While this work in this chapter provided many key insights about the effect of cardiac output and valve orientation on RVOT hemodynamics, clinical studies are necessary to determine how flow features are correlated with adverse outcomes from

PVR surgery. Clinical studies could ascertain the association between flow features, such as recirculation, and long-term outcomes, thus establishing which hemodynamic environments are the most favorable for valve function. In addition, we used the same valve for all of our experiments for consistency. However, it is possible that some of the features we observed, particularly in the high-speed imaging experiments, might be a property of this specific valve as opposed to all bioprosthetic valves.

Overall, the work in this chapter demonstrated the compound effect of cardiac output and valve orientation on RVOT hemodynamics and valve performance. The combination of 4D flow MRI and high-speed imaging allowed us to obtain a full view of the valve environment. In particular, we determined that the 2 L/min case had multiple features in the flow fields and valve leaflet behavior that could adversely effect long-term valve performance.

Chapter 5

Effects of Valve Position

5.1 Background

Due to the wide variation in patient anatomies in ToF, surgeons must determine where to place the surgical valve in native right ventricular outflow tract (RVOT) during pulmonary valve replacement (PVR). Surgeons need to ensure that the valve placement will not obstruct the coronary arteries or other vessels and place the valve to allow for vessel closure with an outflow tract patch (Kogon et al., 2007). Within these constraints and other clinical considerations to ensure the valve functions properly, the surgeon can place the bioprosthetic pulmonary valve anywhere along the vessel between the RV exit and the first PA bifurcation. In general, the valve is placed close to the RV exit, which is where the native pulmonary annulus would occur. In addition, clinical descriptions of PVR procedure indicate that the valve should be aligned with the MPA and pointed towards the downstream PAs (Kogon et al., 2007; Fuller, 2014).

For ToF patients, this valve placement decision is not always straightforward. One of the more common variations seen in ToF is acute curvature between the RV and the MPA (Arana et al., 2021; Luo et al., 2021; Shen et al., 2021; Kirklin et al., 1992). For patients with this acute angle, surgeons must determine where to place the valve along the curvature. The two most common options considered by clinicians are to align the valve with the RV and place it upstream of the curvature or to align the valve with the MPA and place it downstream of the curvature, as illustrated in the sketches in Figure 5.1.

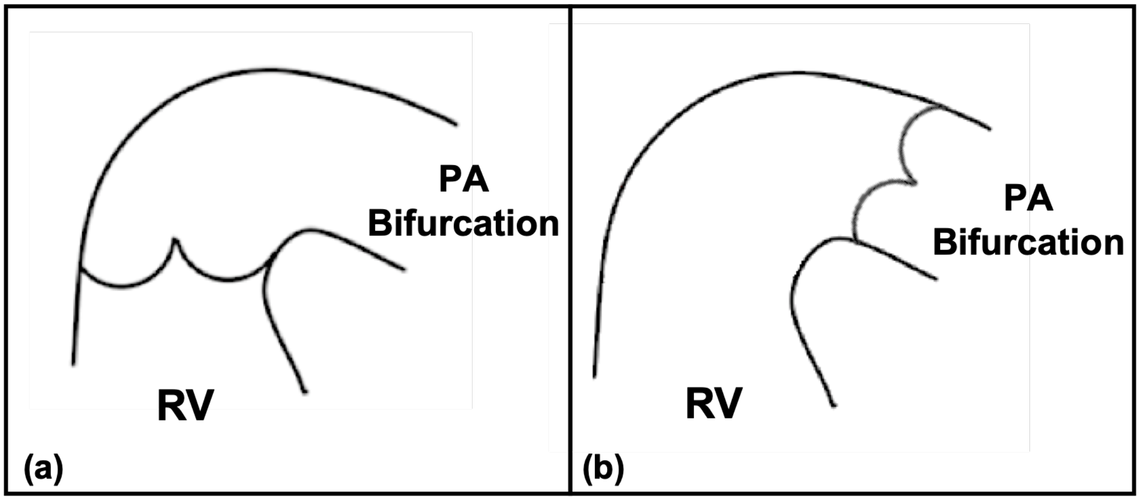

Figure 5.1: Sketches of the two most common options for valve placement in patients with acute curvature in the RVOT. Option (a) aligns the valve with the RV, upstream of the curvature. Option (b) aligns the valve with the MPA, downstream of the curvature. Sketches are based on illustrations provided by Dr. Doff McElhinney.

The decision on valve placement is made by the surgeon for every patient. In these patients with extreme curvature, the choice of how to align the valve will impact the flow patterns in the vessel and overall function of the valve. Fuller (2014) recommends tilting the valve such that the blood flow is not directed towards the anterior vessel wall, as that could lead to the development of a pulmonary artery aneurysm. However it is not clear that this placement option is available in ToF patients with extreme curvature and there are no clinical studies that specifical examine the hemodynamics of different valve placement choices in this patient population.

In this chapter, we discuss the design of two RVOT models with an acute angle between the RV and the MPA, one with the valve aligned with the RV and the other with the valve aligned with the MPA. We conducted four 4D flow MRI studies: both models were run with the valve in the native and the rotated orientation. Qualitative and quantitative comparisons were made across all four cases to examine how valve position and orientation affect the hemodynamics in RVOTs with acute curvature.

5.2 Experimental Details

5.2.1 Valve Alignment Model Design

For the healthy and the dilated models discussed in previous chapters, we used the same vessel centerline for both geometries. This could not be translated to the valve alignment models, since they need to represent a case with a severely acute angle between the RV and the MPA. However, we still used the same ventricle box design to drive the pulsatile flow through the system. From the ventricle box, we adjusted the RV outlet to capture the extreme curvature geometry.

With the assistance of Dr. Doff McElhinney, we developed the centerline for the model with the valve aligned with the RV. This new centerline was designed to represent a generalized version of the extreme curvature cases seen in the clinic. The same curvature was used to design the model with the valve aligned with the MPA, with minor modifications to accommodate design considerations for the valve-holder component and 3D printing restrictions. The same modular design principles were used for these models, which were designed to fit the same 25mm valve used in all previous experiments.

The RV component for the valve aligned with the RV case consists of the ventricle box and the RV exit. This connects to the new valve-holder component, which functions the same as the original valve-holder, but was shortened to accommodate the extra vessel length added to the curvature. The final component consists of the downstream MPA with the acute curvature and the PA bifurcation. The centerline vessel length from RV to bifurcation is 56mm for the valve aligned with RV case.

The RV component for the valve aligned with the MPA case comprises the ventricle box, the RV exit, and the MPA, since the vessel curvature is upstream of the bioprosthetic valve in this case. This RV assembly connects to the same valve-holder as the aligned with RV model. The final component consists of only a short MPA portion before going into the PA bifurcation. For this case, the centerline vessel length from RV to bifurcation is 63mm. For both cases, the bifurcation angle between LPA and RPA and the diameters and centerlines of the branches were identical the healthy and dilated models. These two models represent the options for valve placement in an RVOT anatomy with extreme curvature and still contain modular components to allow for easy changes in valve orientation (Figure 5.2).

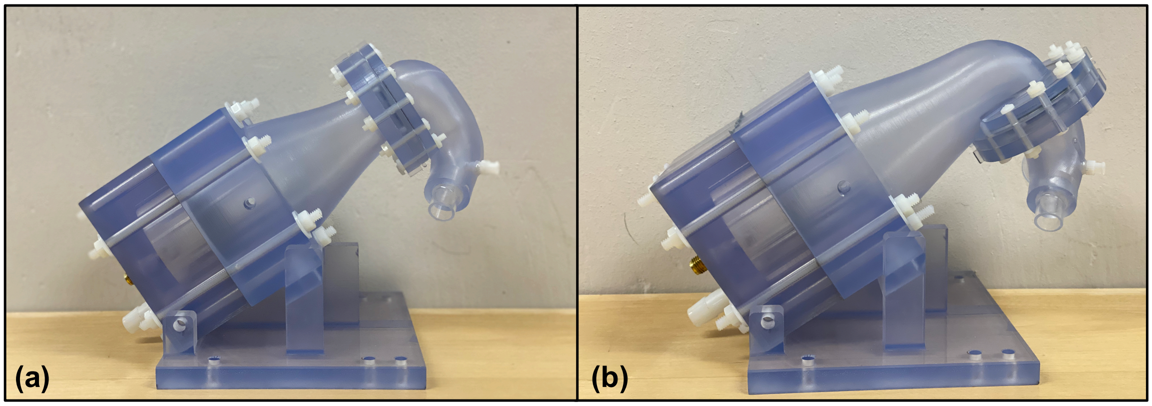

Figure 5.2: The 3D printed model of the RVOT for the valve aligned with RV case (a) and the valve aligned with MPA case (b).

The models were run in the same experimental flow loop as the healthy and the dilated models at 3.5 L/min. The same settings for the pneumatic driving system and the downstream capacitance for model valve alignment models as the other 3.5 L/min cases. Thus, we achieved physiological flow and pressure waveforms in both models, which were similar to the waveforms from previous experiments (Figures 5.3 and 5.4). The flows and pressures were measured by ultrasonic flow probes and catheters, respectively, at the same locations in the flow loop described in Section 2.3.5.

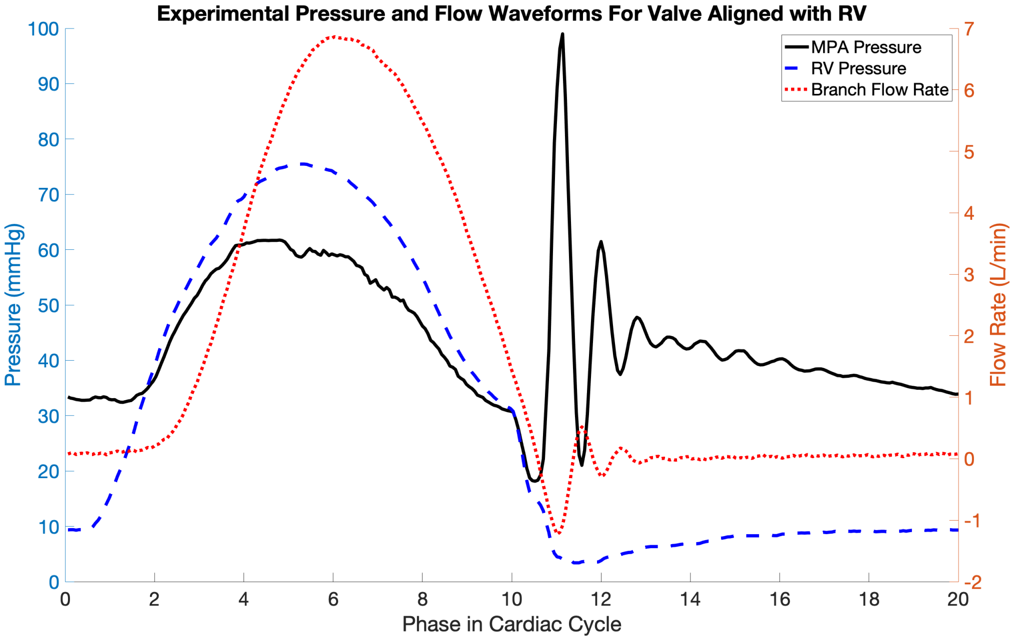

Figure 5.3: Experimental pressure and flow rate waveforms for the model with the valve aligned with RV. MPA and RV pressures are plotted against the left axis and the outlet branch flow waveform is plotted against the right axis.

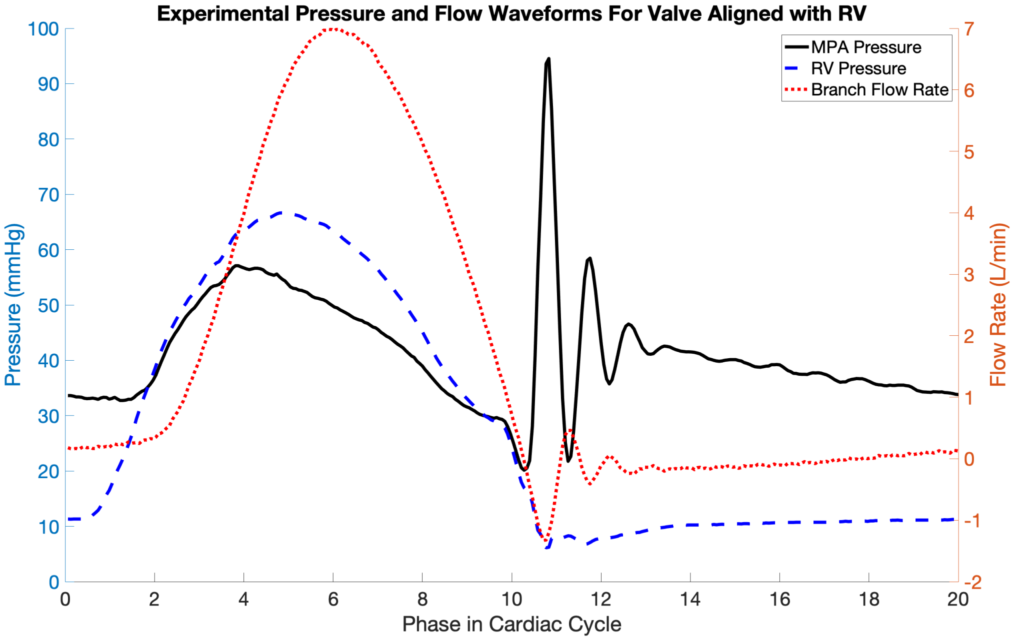

Figure 5.4: Experimental pressure and flow rate waveforms for the model with the valve aligned with MPA. MPA and RV pressures are plotted against the left axis and the outlet branch flow waveform is plotted against the right axis.

5.2.2 4D Flow MRI Experiments

Four 4D flow MRI experiments were conducted for the cases of RVOT anatomy with acute curvature. We scanned the model with the valve aligned with RV with the native and rotated orientation and did the same for the model with the valve aligned with the MPA.

The scan procedure and some of the sequence settings for the MRI match those of previous experiments, as described in Section 2.1.2. However, we had to adjust the FOV in the magnet as the curvature meant the models were at a different angle and position in the magnet bore. The changed parameters for the valve alignment scans are summarized in Table 5.1. Due to the different angles in the model, the streamwise flow direction was not aligned with the magnet coordinate system when the data were collected. We used an in-house MATLAB code to rotate the coordinate system and interpolate the MRI data to set the streamwise flow through the valve annulus to the positive x direction. The rotated data sets were used for all analysis. We set the model coordinate system for each case such that z = 0 is through the center of the vessel and x = 0 is at the valve annulus. This allows us to compare flows at the same location across the two different valve alignment models.

We calculated the SNR and velocity uncertainty for both of the models. The VENC in all cases was 250 cm/s in the sagittal, axial, and coronal directions. The velocity uncertainty is calculated as the percent of the mean velocity through the valve opening at peak systole. This velocity differed between the two cases due to variations in the geometries. The reference velocity was 88 cm/s for the valve aligned

Scan Parameter	Value
Frequency FOV	15.0cm
Phase FOV	0.4
Imagining Matrix	166x166
TE	1376 microseconds
TR	3788 microseconds

Table 5.1: 4D flow MRI scan parameters for valve alignment models

with the MPA cases and was 73 cm/s for the valve aligned with the RV cases. The native and rotated scans for each case had similar SNR values since the scans were conducted on the same night. The average SNR for the valve aligned with MPA cases 17.2, resulting in an uncertainty of 7.5%. The average SNR for the valve aligned with RV cases 17.6, resulting in an uncertainty of 8.8%.

5.3 Results

Despite the large difference in valve position in the two acute angle RVOT models, there were a few similarities across all cases. The jet shape immediately after the valve annulus was qualitatively similar across all cases and the valve orientation determined the angle of the jet in the vessel, similar to behavior seen in previous experiments (Figure 5.5). With the native valve orientation, the jet impinged on the downstream vessel wall for both valve alignments. This behavior may have clinical relevance, as the impact of the jet may lead to vessel dilation and remodeling in the pulmonary arteries. The location of the jet impingement and the effect on the surrounding flow varied significantly for each case. In the valve aligned with the MPA case with native orientation, the jet impacts the vessel wall near the bifurcation, which can be seen in both the velocity contours in sagittal slice z = 0 (Figure 5.5a) and in 3D velocity isosurfaces (Figure 5.6a). Consequently, reversed flow regions formed along both the inner and outer curve of the vessel. In the valve aligned with the RV case with native orientation, the jet impacted the MPA wall opposite the valve annulus (Figure 5.5c). Due to the curvature of the vessel, the flow continued to move towards the bifurcation, resulting in forward flow along the inner curve. However, reversed flow regions formed along the rest of the vessel wall upstream of the curve, resulting in reversed flow nearly surrounding the valve annulus (Figure 5.6c).

In both valve alignments, rotating the valve orientation lessened the severity of the jet impact on the vessel wall. For the valve aligned with the MPA case, the rotated orientation directed the jet down towards the PA branches instead of into the wall before the bifurcation, preventing the strong jet impingement. However, a larger region of reversed flow formed along the outer vessel wall (Figure 5.5b). Flow recirculation towards the valve leaflets occurred in this region, which may adversely affect valve performance, but the reduction of the jet impingement can prevent vessel remodeling. Thus, the choice of valve orientation presented clinical trade-offs that would need be considered along with placement location in the RVOT.

In the valve aligned with the RV position, the rotated orientation had similar effects. The jet through the valve was directed lower on the vessel wall and had less speed at the impact point. However, this led to a large recirculation region of reversed flow above the jet (Figure 5.5d). In addition, a smaller region of reverse flow formed along the inside curve close to the valve annulus. Due to its position on the upstream side of the tight vessel curvature and its proximity to the valve, the recirculation of flow in this region could make the valve more prone to calcification. For both the native and the rotated orientation, aligning the valve with the RV produced significantly more reversed flow than the other valve alignment and many of the other cases studied earlier in this work.

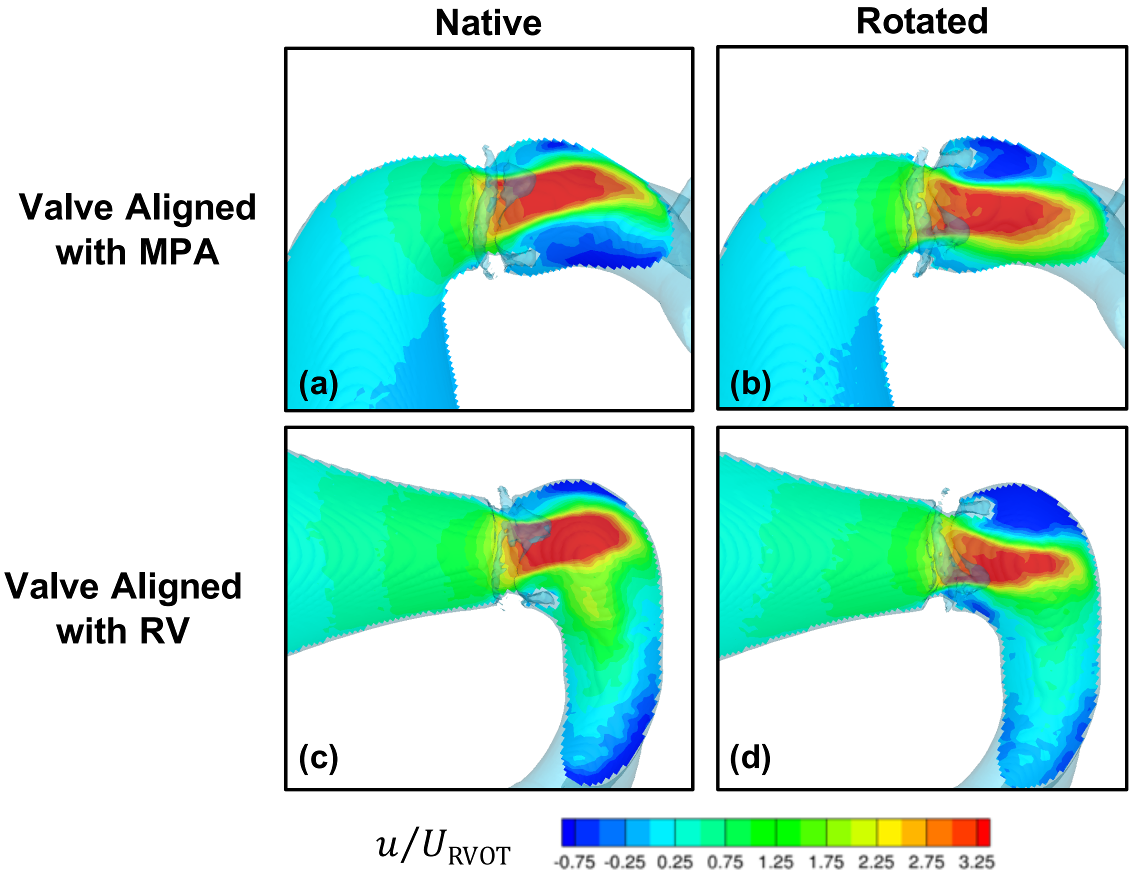

Figure 5.5: X-component of velocity contours normalized by the peak speed upstream of the valve shown at sagittal slice z = 0 at peak systole for the valve aligned with MPA case (top row) and valve aligned with RV case (bottom row) for the two valve orientations.

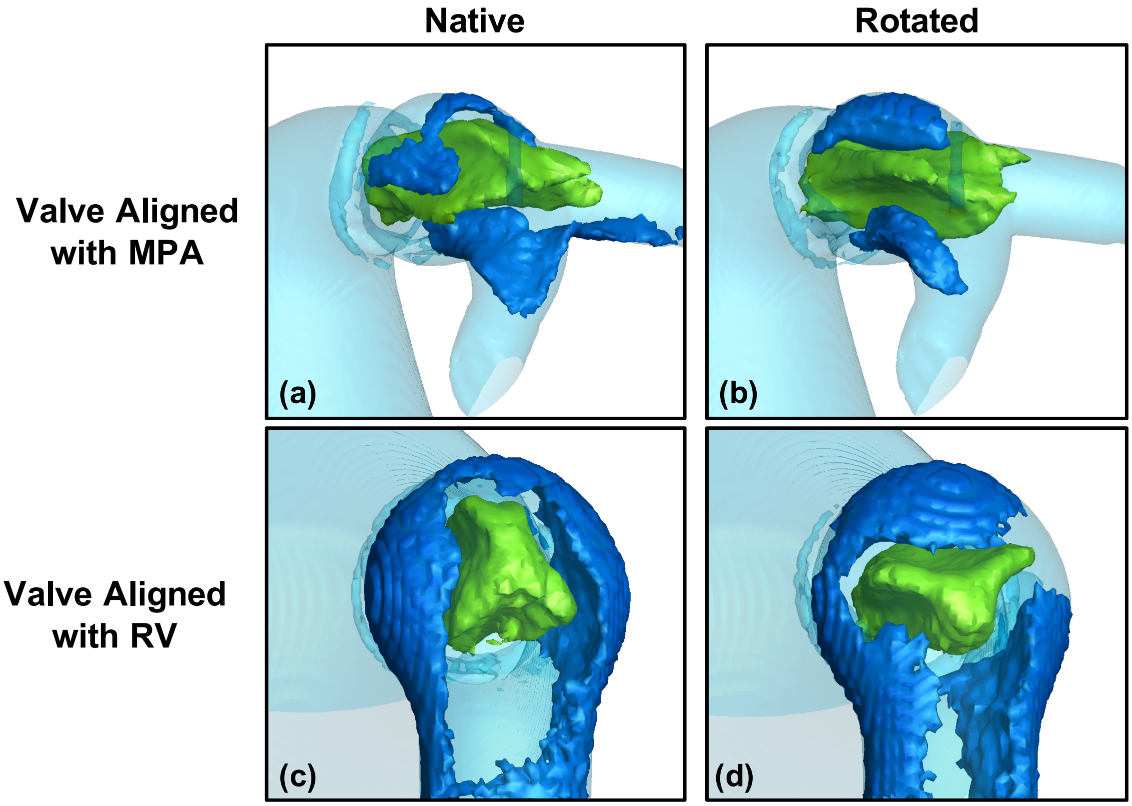

Figure 5.6: Velocity isosurfaces in the valve aligned with MPA model (top row) and valve aligned with RV model (bottom row) at peak systole for the native (left column) and rotated (right column) valve orientations. The green and blue isosurfaces represent u_x/U_{RVOT} = 2 and u_x/U_{RVOT} = -0.3 respectively.

Examining the flow in an axial slice downstream of valve structure over systole revealed additional differences between the valve position cases. For the valve aligned with the MPA, the triangle-like jet formed as the flow was accelerating during phase 4 of the cardiac cycle, peaked in velocity at phase 6, and began to lose speed as the flow decelerated in phase 8 (Figure 5.8). For both the native and orientations, the jet shape was similar to the dilated MPA model with a cardiac output of 3.5 L/min discussed in Chapter 3. Thus, placing the valve at the MPA resulted in similar streamwise flow features to the geometry without acute curvature near the valve.

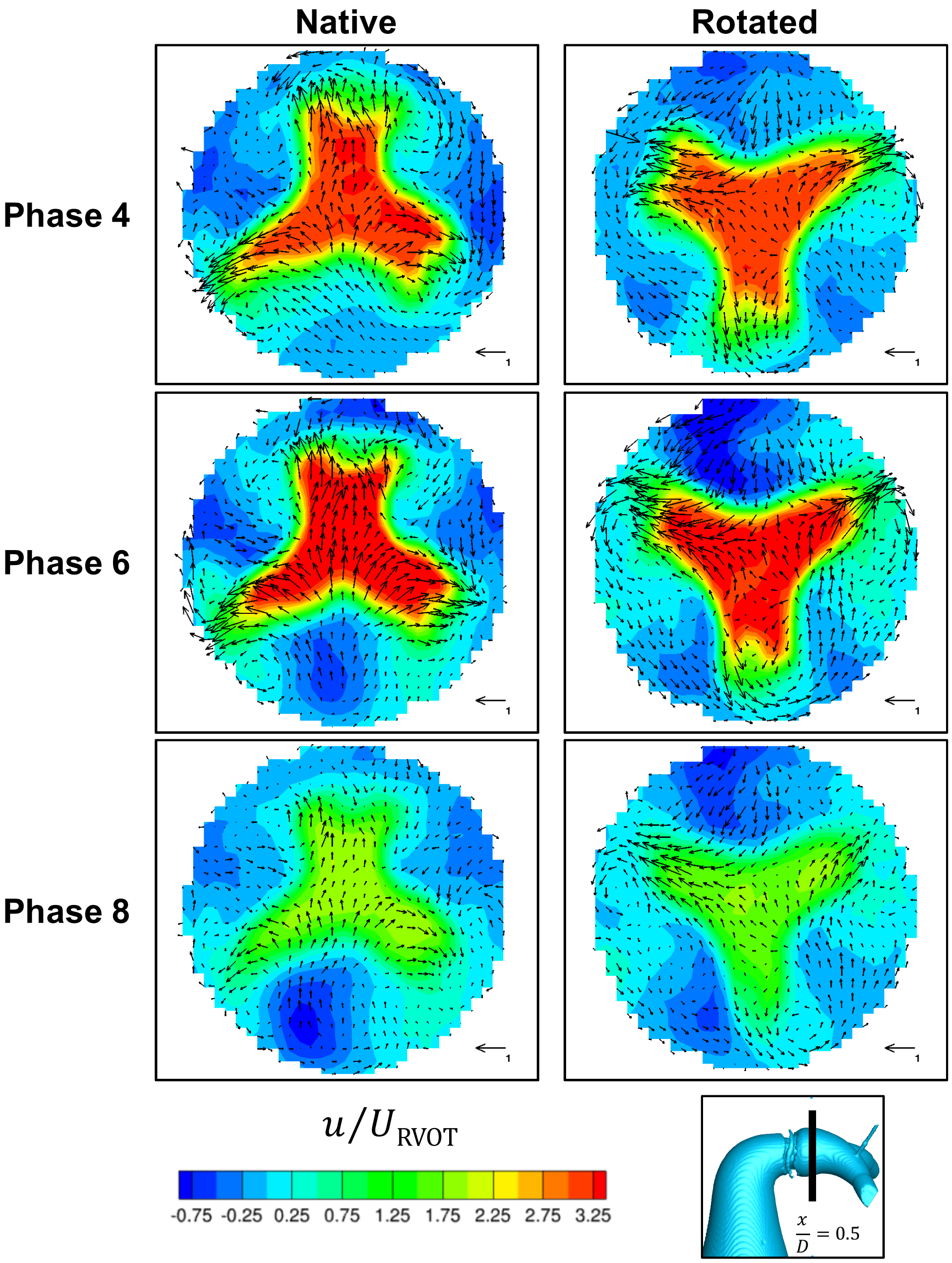

Figure 5.7: Normalized x-component of velocity contours with in-plane velocity vectors for the valve aligned with the MPA case for three different phases during systole at axial slice x/D = 0.5. The location of this slice in the model is shown in the bottom right. The flow is accelerating during phase 4 and decelerating during phase 8; phase 6 is peak systole. Contours are shown for both the native (left) and rotated (right) valve orientation.

However, for the valve aligned with the RV case, the jet shape changed significantly over systole (Figure 5.8). At phase 4, as the flow accelerated in early systole, a version of the triangle-like jet shape formed in both the native and rotated cases. However, as the forward flow continue to move through the vessel curvature, the jet became distorted. In the native case, the combination of the jet impingement and the curving vessel resulted in faster flow along the inside curve, which pushed the core of the jet upwards in the vessel at peak systole. As the flow began to decelerate, the core shape of the jet was no longer present as strong recirculation in the secondary flows developed over the vessel cross-section. The jet shape was also distorted in the rotated orientation at systole, though in this case it was due to the large reversed flow and separation region that developed along the outer curve of the vessel. The triangular structure was completely gone by phase 8, as strong secondary flows moved over the vessel cross-section, similar to the native orientation. The vast differences between the jet behavior for the valve aligned with the MPA versus aligned with the RV illustrated the significant impact that valve position has on hemodynamics in acute angle RVOTs.

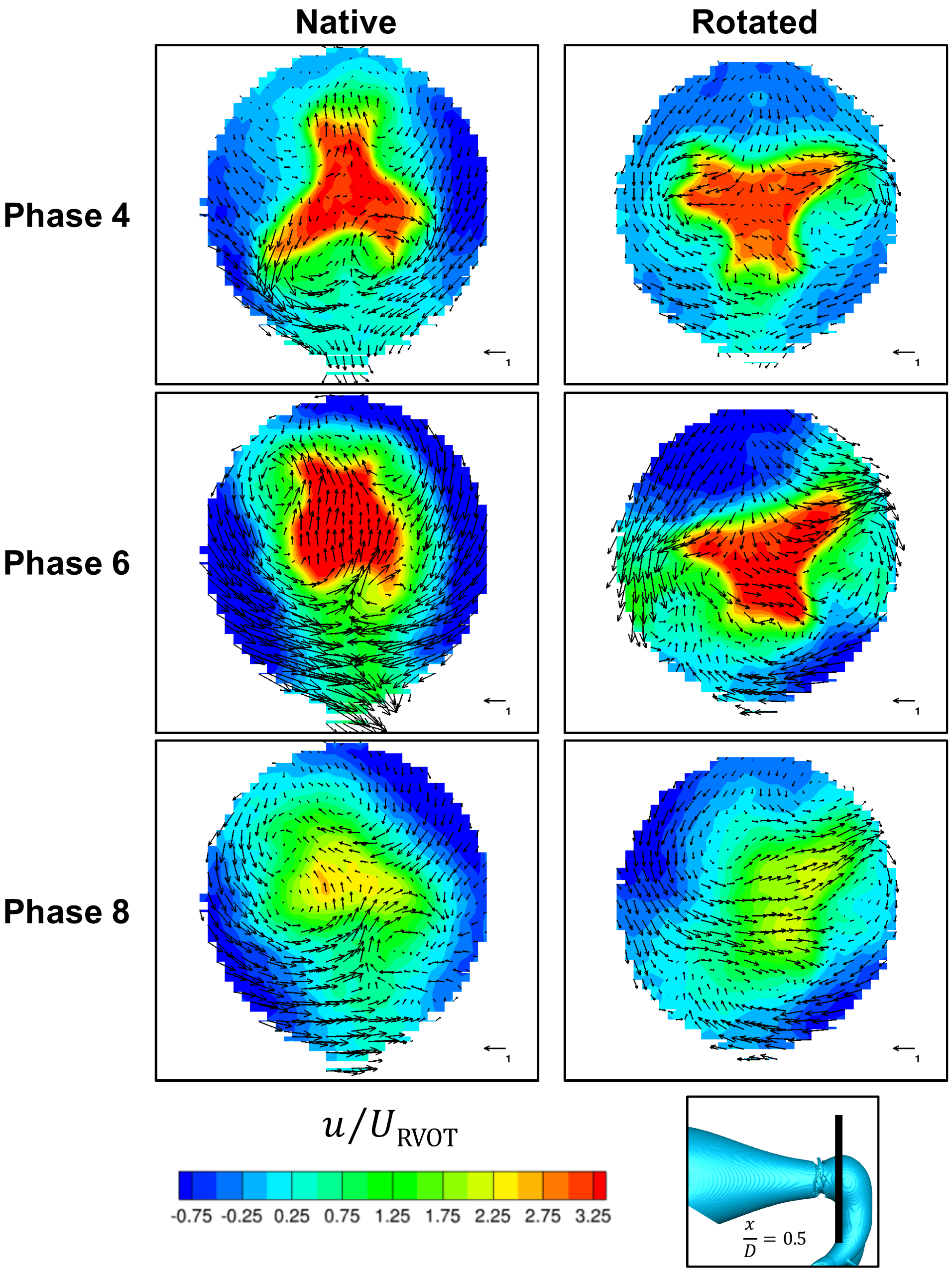

Figure 5.8: Normalized x-component of velocity contours with in-plane velocity vectors for the valve aligned with the RV case for three different phases during systole at axial slice x/D = 0.5. The location of this slice in the model is shown in the bottom right. The flow is accelerating during phase 4 and decelerating during phase 8; phase 6 is peak systole. Contours are shown for both the native (left) and rotated (right) valve orientation.

We quantified the effect of valve position on streamwise momentum and secondary flow strength using the integral metrics introduced in Section 3.3.2. We calculated I_1 and I_2 at two axial slices, x/D = 0.25 and x/D = 0.5, for all four cases (Figure 5.9). The streamwise momentum I_1 was higher for the valve aligned with RV cases at x/D = 0.25, which may be due to increased momentum from the flow moving through the acute curvature of the vessel after exiting the valve at the RV. By x/D = 0.5, these effects have dissipated and all four cases have nearly the same streamwise momentum. As seen in the previous studies, the valve orientation did not effect the streamwise momentum in the models.

In contrast, the secondary flow strength I_2 was significantly higher when the valve was aligned with the RV. For these cases, I_2 reached a maximum just after peak systole, corresponding to the increased recirculation and secondary flows over the entire cross-section as seen in Figure 5.8. The secondary flow strength for the valve aligned with the RV was greater at x/D = 0.5 than at x/D = 0.25. The location x/D = 0.5 is nearly downstream of the acute curvature in this model. Thus, at this location, the flow fields were experiencing the full effect of the faster flow along the inside curve of the vessel, the jet impingement, and the transverse pressure gradient associated with the flow curvature. This contributed to a complex flow field with strong secondary flows, quantified by the higher I_2 value. In addition, the native orientation had higher I_2 than the rotated orientation, indicating that the direction of the jet and strength of the impingement with the native orientation resulted in stronger secondary flows. For the valve aligned with the MPA case, the secondary flows were barely half as strong as the RV aligned case. When the valve was aligned with the MPA, the vessel downstream of the annulus had only slight curvature and there was only a short segment before splitting into the LPA and RPA. This limited the generation of strong secondary flows, as evidenced by relatively weak recirculation in the in-plane vectors in Figure 5.7 and the calculated I_2 values (Figure 5.9).

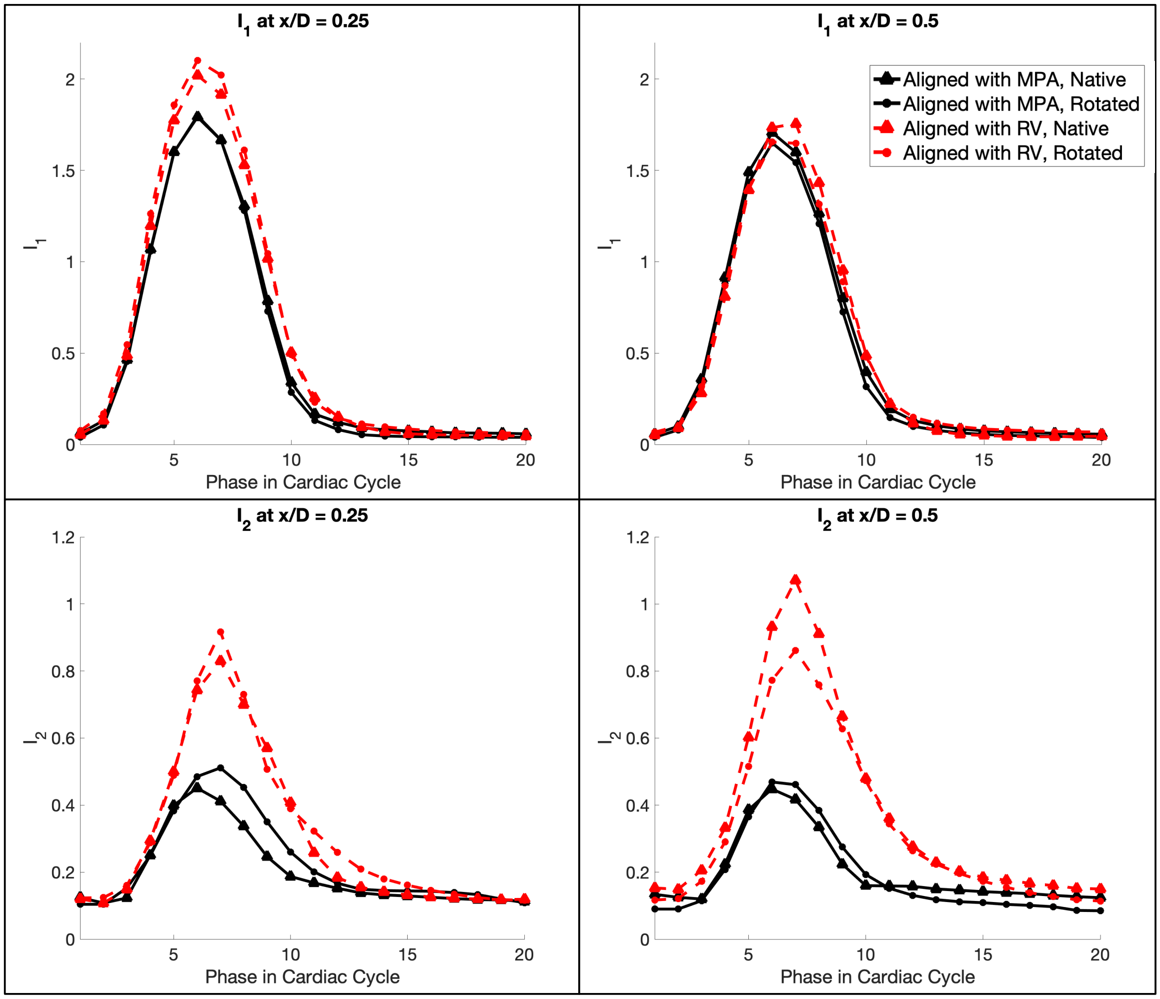

Figure 5.9: Quantitative integral metrics I_1 (top row) and I_2 (bottom row) at two axial slices, x/D = 0.25 (left column) and x/D = 0.5 (right column) for the two valve alignment models. The legend in the top right corner applies to all plots.

5.4 Conclusions

We designed two models to represent the most common clinical choices for how to position the valve in PVR patients with an acute angle between the RV and the MPA. Though we used the same curvature centerline for both models, the placement of the valve aligned with either the RV or the MPA resulted in two different geometric environments for the valve. As expected, this resulted in substantially different flow fields observed in the two cases. For the valve aligned with the MPA, the acute curvature was upstream of the valve annulus. Thus, the flow through the valve had similar features to the healthy and dilated MPA models, which did not have extreme angles. The forward jet had a similar triangle-like shape throughout systole (Figure 5.7). The reversed flow regions formed in the same regions along the vessel walls where the native orientation case produced more reversed flow along the inner curve while the rotated orientation generated reversed flow along the outer wall (Figure 5.6). However, the jet in the valve aligned with the MPA case impinged on the vessel wall above the bifurcation, which did not occur in any previous studies.

The valve aligned with the RV resulted in a variety of flow features that were not observed in any other model. In the native orientation case, there was no reversed flow along the inner wall due to the angle of the jet and the faster flow around the acute curvature. In the rotated orientation case, the only reversed flow along the inner wall was in the small region between the valve support structure and the vessel wall at the most upstream point of the curvature. This region experienced strong recirculation, which would likely contribute to calcification as it was close to the valve leaflets. While no reversed flow developed along the inner curve, it did occur on the rest of the vessel wall, resulting in a large volume of backward flow that essentially encircled the valve (Figures 5.6c and d). Thus, both the native and rotated valve orientations for the valve aligned with the RV case had significantly higher volumes of reversed flow than the valve aligned with the MPA. The valve aligned with RV cases also had stronger secondary flows, likely due to the complex flow patterns produced by the jet impingement and flow around the acute inner curve (Figure 5.9).

For both valve alignments, the valve orientation had a significant impact on the jet impingement on the vessel wall. Changing the valve from the native to the rotated orientation shifted the location of the jet impingement and decreased its severity. Jet impingement is clinically relevant, as flow impacting the vessel wall may lead remodeling and dilation. PVR surgical strategies recommend positioning the valve such that the flow is directed toward the downstream PAs in order to avoid direct jet impact on the vessel wall (Kogon et al., 2007; Fuller, 2014). This recommendation aligns with our valve aligned with the MPA case. However, we observed that the case of acute RVOT curvature, aligning the valve with the MPA with its native orientation resulted in the most severe jet impingement of the four cases we studied. Thus, for patients with anatomies similar to our model, following the guidance of aligning the valve with the MPA may lead directly to the jet impingement environment that surgeons try to avoid.

Placing the valve with the rotated orientation aligned with the MPA significantly reduced the jet impingement. Making an adjustment in valve orientation in patients with acute RVOT angles could prevent adverse remodeling in the vessel. This demonstrated that given a particular anatomy, it is possible to find a combination of valve orientation and position that produces an overall favorable hemodynamic environment.

While these findings are promising, there are still trade-offs in all cases in jet impingement, reversed flow, recirculation, secondary flow strength, and other flow features. Clinical studies connecting hemodynamic features to PVR outcomes are necessary to fully determine the optimal bioprosthetic valve environment. We were also limited by our focus on curvature in the sagittal plane between the RV and the MPA. ToF patients may also have curvature in other planes and between the MPA and the bifurcation. Future studies could examine how additional curvature in the vessel would effect the location of jet impingement and the potential for vessel remodeling.

Chapter 6

Validation of Valve Leaflet Simulations

The work in this chapter is a collaboration between Dr. Alexander Kaiser and myself to use the experimental data obtained in this thesis work to validate the computational valve model developed by Dr. Kaiser. Section 6.1 summarizes Dr. Kaiser's methodology, based on his papers for modeling the aortic valve and the mitral valve (Kaiser et al., 2021, 2019). Sections 6.2 and 6.3 describe our collaborative validation work. I am the author of all of the text in this chapter.

6.1 Simulation Methodology

This section summarizes the aortic valve model developed by Dr. Kaiser in the following paper: A. D. Kaiser, R. Shad, W. Hiesigner, and A. L. Marsden. A Design-Based Model of the Aortic Valve for Fluid-Structure Interaction. *Biomechanics and Modeling in Mechanobiology*, 2021. Accepted, to appear. (Kaiser et al., 2021)

Kaiser et al. (2021) developed a new mechanistic model for the aortic valve based on first principles. The key consideration in the valve model design is that it must support a pressure in its closed configuration. The model assumes that each leaflet of the trileaflet valve model can exert tension in the circumferential and radial directions and that the shear tension is identically zero. The tension in the leaflets must balance the pressure forces acting on the valve, yielding a state of static mechanical equilibrium.

A system of partial different equations is derived from this mechanical equilibrium with the tension and pressure forces acting on the leaflets. The details of this derivation can be found in Kaiser et al. (2021). The solution to these equations yields the predicted loaded configuration for the valve model. This configuration encompasses the full loaded leaflet geometry, the fiber orientations with the valve leaflets, and tensions required to support the pressure load. The loaded valve geometry is then used to develop the constitutive law for the valve and set up the configuration used as the initial condition for fluid-structure interaction (FSI) simulations.

The interaction of the model with blood flow is simulated using FSI with the immersed boundary (IB) method (Peskin, 2002). In the IB method, a Eulerian reference frame is used for the fluid and a Lagrangian reference frame is used for the structure. The fluid interacts with the structure through a body force exerted by the structure. The governing equations for the IB method are the Navier Stokes equations for a viscous, incompressible fluid, conservation of momentum, conservation of volume, interaction equations that couple the Eulerian and Lagrangian frames, and equation to map the configuration of the structure to the body force it exerts on the fluid. This mapping includes the constitutive law developed for the valve leaflet model and any other prescribed forces including those that hold the leaflets in place. Further details on these equations and the IB method are available in Kaiser et al. (2021) and Peskin (2002). The IB equations for FSI simulations were solved with using the software library IBAMR (Griffith, 2021).

The aortic valve model, simulated using the IB method, opens freely during systole and seals completely when closed over multiple cardiac cycles. This model has been tested in a rectangular box test chamber with periodic flow and physiological pressures, and previous work that this methodology was adapted from successfully simulated the mitral valve in similar conditions (Kaiser et al., 2019). However, the model has not yet been validated against experimental or *in vivo* data in a realistic anatomy.

This aortic valve model is a design-based approach where the geometry and material properties are derived and tuned rather than relying on empirical data. Thus, it can be tuned for a given gross morphology and valve annulus geometry, which allows it to be adapted for situations other than the native aortic valve. We took advantage of this feature for our validation work and tuned the model to match the morphology of the bioprosthetic pulmonary valve used in the present ToF experiments in order to validate the valve model and simulation method.

6.2 Modeling the Experimental Geometry

We selected the healthy control model of the RVOT with native valve orientation as the experimental data to validate the valve modeling method. In order to set up the simulation, we needed the geometry of the 3D printed model and the specifications of the bioprosthetic pulmonary valve used in the experimental study. For the vessel geometry, the experimental 4D flow MRI data were thresholded by signal magnitude to isolate the walls of the 3D printed model. Five voxels were trimmed off the edges of the data bounding box to ensure the flow inlet and outlets were planar. The data for the experimental model walls were converted to an STL file, which was imported into the simulation framework. Thus, the experimental data and the simulation used the same wall boundaries for the RVOT geometry. They also used the same coordinate system, allowing for direct comparison at key locations in the flow field.

Both the support scaffold and the leaflets of the 25mm bioprosthetic valve used in the experiment needed to be modeled computationally. We precisely measured the dimensions of the bioprosthetic valve, including the thickness, height, and width of the three support structures at the commissures, free edge length and height of the leaflets, and the position of the valve leaflets within the support scaffold. The measurements of the support scaffold were used to create a functional model of the structure that was attached to the model walls. The measurements of the leaflets were used as inputs to generate the valve leaflets according to the design-based model summarized in Section 6.1. The leaflet parameters for the simulations are summarized

Leaflet Parameter	Simulation Value (cm)
Free Edge Target	2.48
Free Edge Rest Target	2.16
Circumferential Free Edge Loaded Length	2.88
Circumferential Free Edge Rest Length	2.51
Leaflet Height Target	1.40
Leaflet Height Rest Target	0.91
Radial Height Loaded Length	1.40
Radial Height Rest Length	0.91

Table 6.1: Leaflet parameters for valve simulation

in Table 6.1 with targets based on Swanson and Clark (1974).

The boundary conditions on the inlet and outlets were time-dependent prescribed pressures based on the experimental catheter data. The pressures measured in the RV were used for the inlet pressure boundary condition and the pressures measured in the MPA were used for each outlet pressure boundary condition. To generate prescribed pressure waveforms that would operate as simulation boundary conditions, the data taken during the healthy control experiment were linearly interpolated to a time spacing of 5×10^{-6} seconds. The data were also smoothed by a convolution taken with a cosine function. To obtain periodicity, the smoothed, linearly interpolated pressures were represented by a finite Fourier series with 600 frequencies and a fundamental frequency of 1.2 Hertz. Open boundary stabilization was prescribed at both outlets to prevent spurious reverse velocities.

6.3 Validation with Experimental Results

We ran two simulations of the healthy RVOT geometry with the design-based pulmonary valve model: one coarse resolution simulation with a spatial resolution of 0.09cm and a temporal resolution of 3.0×10^{-5} seconds and one fine resolution simulation with a spatial resolution of 0.045cm and temporal resolution at and 7.5×10^{-6} seconds. The simulations were run on Stanford University's Sherlock cluster (24 Intel Xeon Gold 5118 cores per node with a 2.30GHz clock speed). The coarse spatial resolution is the same as the experimental data resolution. To provide a more direct comparison to the experiment data, the simulation velocity field results were averaged in time to recreate the 20 phases over the cardiac cycle that were obtained by the 4D flow MRI sequence.

We first compare the pressure and flow rate waveforms of the fine resolution simulation and experiment (Figure 6.1). The pressure waveforms in the RV and MPA matched well, which was expected due to using the experimental pressures as the prescribed inlet and outlet boundary conditions for the simulation. The pressures plotted for the experimental data in Figure 6.1 are the smoothed and interpolated boundary condition waveforms. The simulation branch flow rate matched the shape of the experiment flow rate waveform, but the peak flow rate in the simulation was lower and occurred later in the cardiac cycle. Both of these issues may be due to the simulation not replicating the resistance and capacitance conditions downstream of the model in the experimental flow loop. As we continue this collaborative work, we plan to implement LPN boundary conditions on the outlets that incorporate these elements as opposed to prescribed pressure conditions.

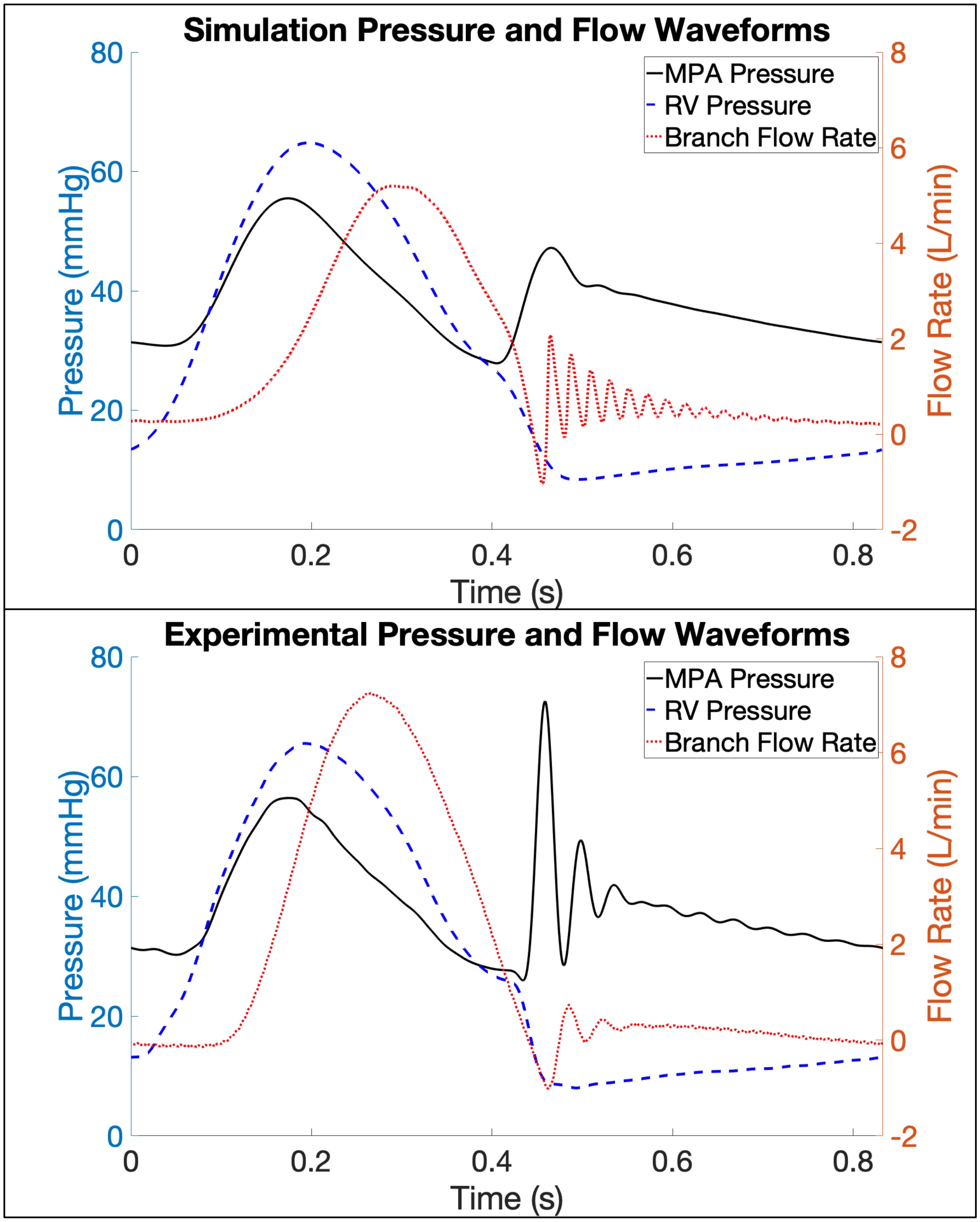

Figure 6.1: The pressure and flow waveforms over the cardiac cycle for the fine resolution simulation (top) and the healthy model experiment (bottom). The pressures plotted for the experiment are the interpolated and smoothed waveforms that were applied as prescribed pressure boundary conditions.

Qualitative comparisons of the computational and experiment velocity fields demonstrate that the valve model was able to produce key flow features seen in the experimental data. The coarse simulation provided a direct comparison to the experimental data, since the velocity fields were produced on the same Cartesian grid. The fine simulation provided additional flow information and the finer mesh resolution captured the valve scaffolding geometry more accurately. All comparisons used absolute velocity values, demonstrating that we captured the physics of the experiment in the simulation. For the qualitative comparisons in this section, we will focus on three phases during the cardiac cycle: phase 4, phase 6, and phase 9. Figure 6.2 shows these phases on a flow rate waveform from the 4D flow MRI data to highlight when they occur during the cardiac cycle. At phase 4, the valve was open and the flow began accelerating. Phase 6 was close to peak systole where the flow through the valve was at its peak. Phase 9 was at the end of systole, when the valve was closing and flow was decelerating throughout the vessel.

The velocity fields in the sagittal slice through the center of the vessel demonstrated how well the simulations captured the shape and angle of the jet through the valve leaflets and the location of reversed flows over the cardiac cycle (Figures 6.3, 6.4, and 6.5). At phase 4, the jet had just extended beyond the valve leaflets; the length of the jet core at this phase was well matched between the simulation and the experiment. Both the coarse and fine simulations had a slightly lower velocity in the core of the jet, but the angle through the valve leaflets was almost identical. As a result, the simulations also capture the reversed flow that developed on the inner edge of the RVOT near the valve annulus.

At peak systole, the jet angle was again nearly identical in the simulations and the experiment (Figure 6.4). The maximum velocity in the core of the jet was better matched than at phase 4. However, the reversed flow regions were not captured as well by the simulations. The reversed flow in the simulations, particularly for the coarse resolution, was further downstream than in the experiment. While some reversed flow did develop in the region along the inner curve close to the valve annulus, it was at a much slower velocity than in the experiment.

The flow deceleration in the vessel occurred in the same way in the experiment

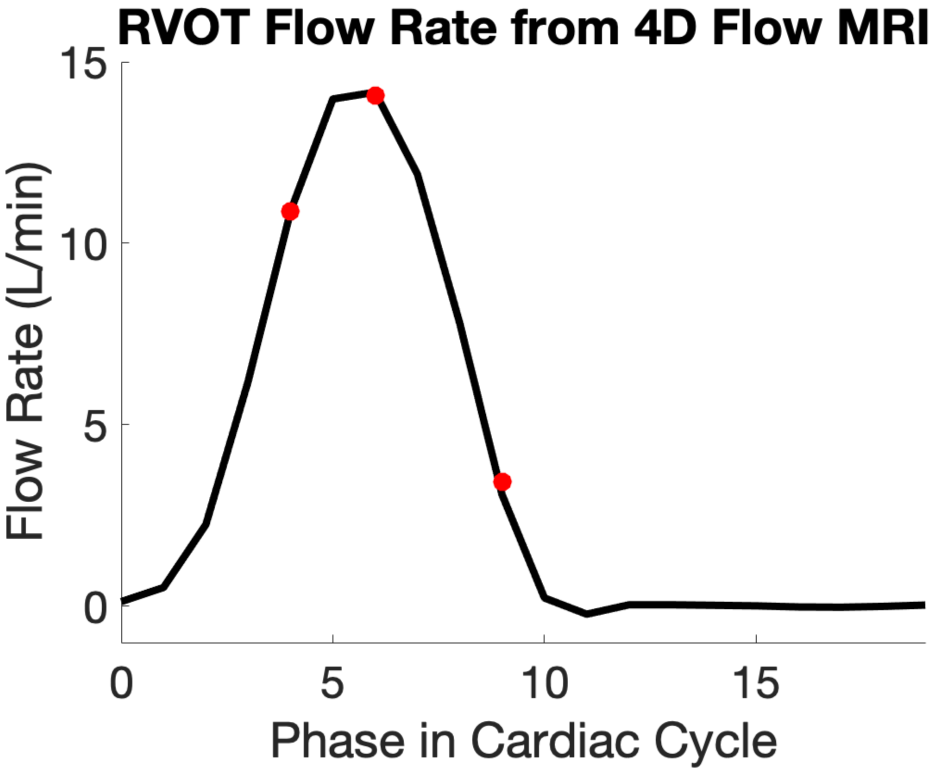

Figure 6.2: Flow rate from the 4D flow MRI experiment, with phases 4, 6, and 9 denoted.

and the simulations (Figure 6.5). The jet angle was maintained and the flow slowed down to approximately the same velocity in both cases at phase 9. In addition, the reversed flow regions were improved for this phase. Though they were not quite at the same velocity in the simulations and the experiment, in both cases the reversed flow volume was along the inner curve and in the bottom portion of the vessel.

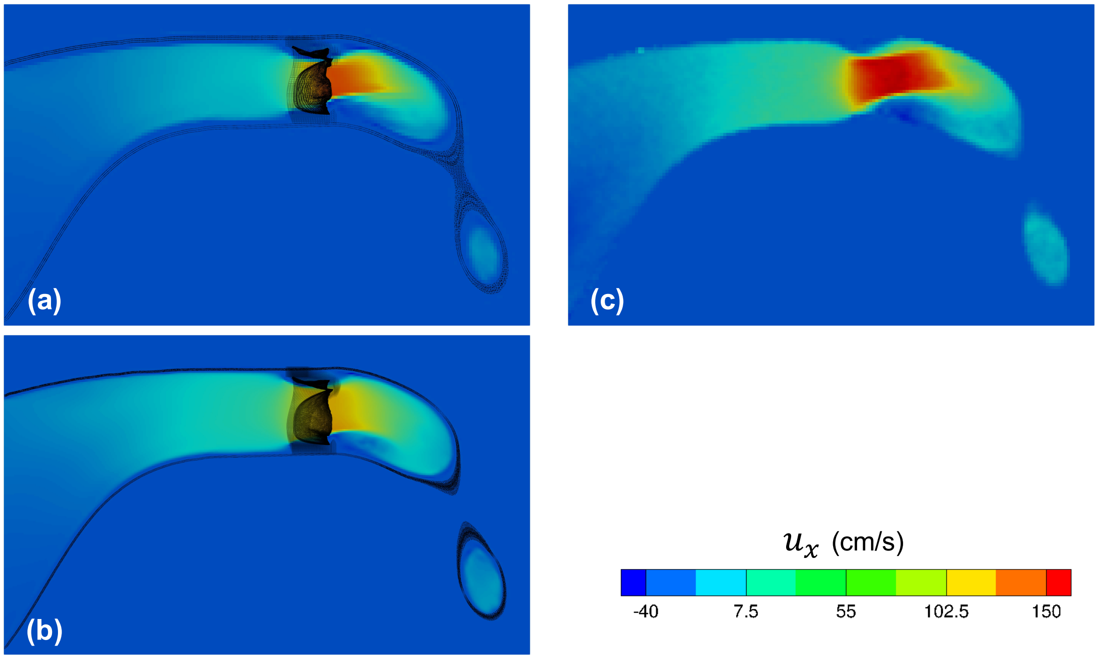

Figure 6.3: Contours of the x-component of velocity in the coarse resolution simulation (a), fine resolution simulation (b), and experiment (c) at phase 4 in the cardiac cycle at sagittal slice z = 0.

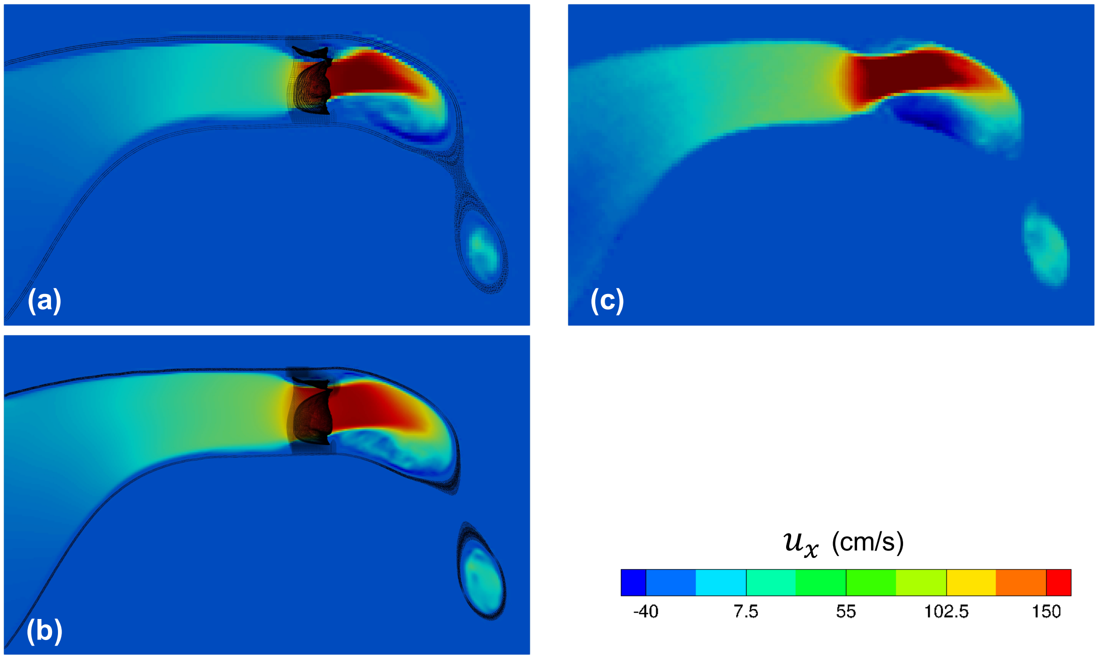

Figure 6.4: Contours of the x-component of velocity in the coarse resolution simulation (a), fine resolution simulation (b), and experiment (c) at phase 6 in the cardiac cycle at sagittal slice z = 0.

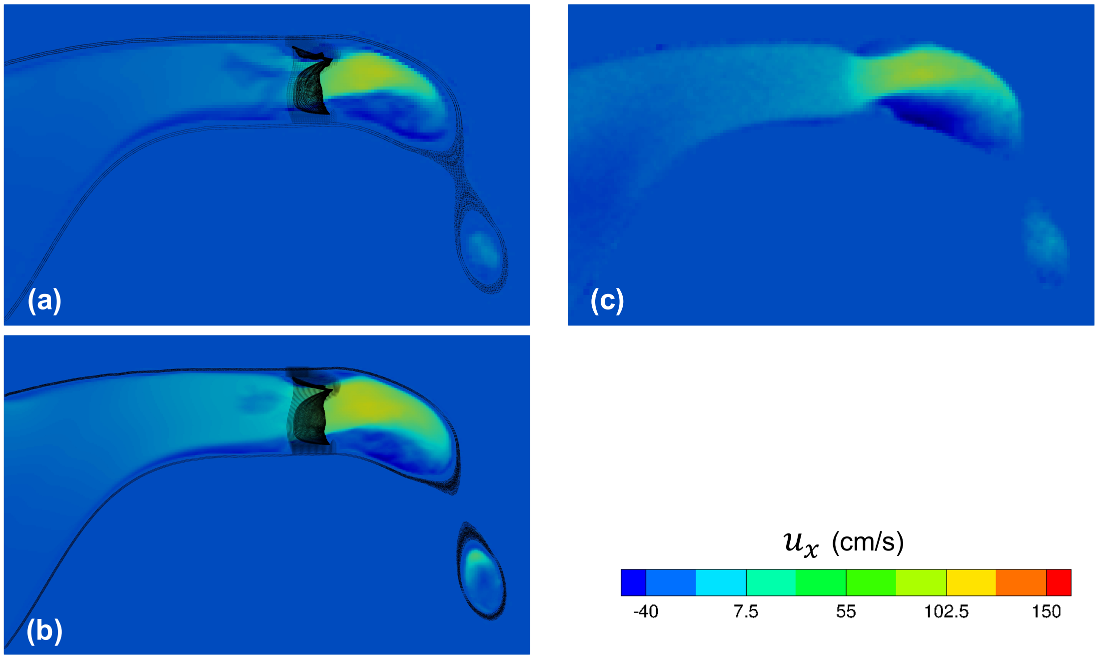

Figure 6.5: Contours of the x-component of velocity in the coarse resolution simulation (a), fine resolution simulation (b), and experiment (c) at phase 9 in the cardiac cycle at sagittal slice z = 0.

The sagittal slices demonstrated that the simulations were able to produce similar velocities, jet angle, and reversed flow regions over the cardiac cycle. Though there was room for improvement, the valve model and surrounding fluid were clearly capturing the physics of the bioprosthetic valve and experimental flows. Axial slices at various locations in the vessel provide a more complete view of the jet shape and velocity over the cardiac cycle (Figures 6.6, 6.7, and 6.8).

Axial slice x = 0 is at the valve annulus. At this location, the simulations captured the flow through the valve, but underestimated the velocity of the jet (Figure 6.6). The fine simulation came closer to the experimental velocity than the coarse simulation, due to the fact that the finer mesh more accurately represents the geometry of the valve scaffolding. The support structures of the valve clearly influenced the shape of the forward flow jet. In the experiment, the jet had a slight triangular shape even at the valve annulus. This feature was not captured by the simulations. This could be improved by making adjustments to the valve scaffold geometry. In addition, developing boundary conditions that are more tuned to the downstream conditions of the experiment could also increase the flow rate through the valve. Though the simulations underestimated the velocity during peak systole at the valve annulus, they did capture the decelerating flow in phase 9.

The simulation velocities came closer to matching the experiment at axial slice x/D = 0.25, which cuts through the valve leaflets and support structure (Figure 6.7). At phases 4 and 6, the simulations produced high velocity flow through the valve, though not quite at the same magnitude as the experiment. The velocities in phase 9 as the flow decelerated were very similar. However, the shape of the jet was mostly circular in the simulations, while the jet at this location in the experiment had started to develop the triangular shape seen in all the present experimental studies. The flow fields at axial slice x/D = 0.5 had similar features as the x/D = 0.25 slice (Figure 6.8). The velocities were well matched, particularly at phases 6 and 9, which corresponded to the sagittal view of the jet. However, the simulations did not capture the three tips of the jet that occurred in the experiment. The fine simulation jet formed a triangle, but was missing the indents in the shape between the leaflets. The axial slices demonstrated that the general flow features were captured by the simulations but highlighted a key area for future improvements in better replicating the shape of the jet through the valve.

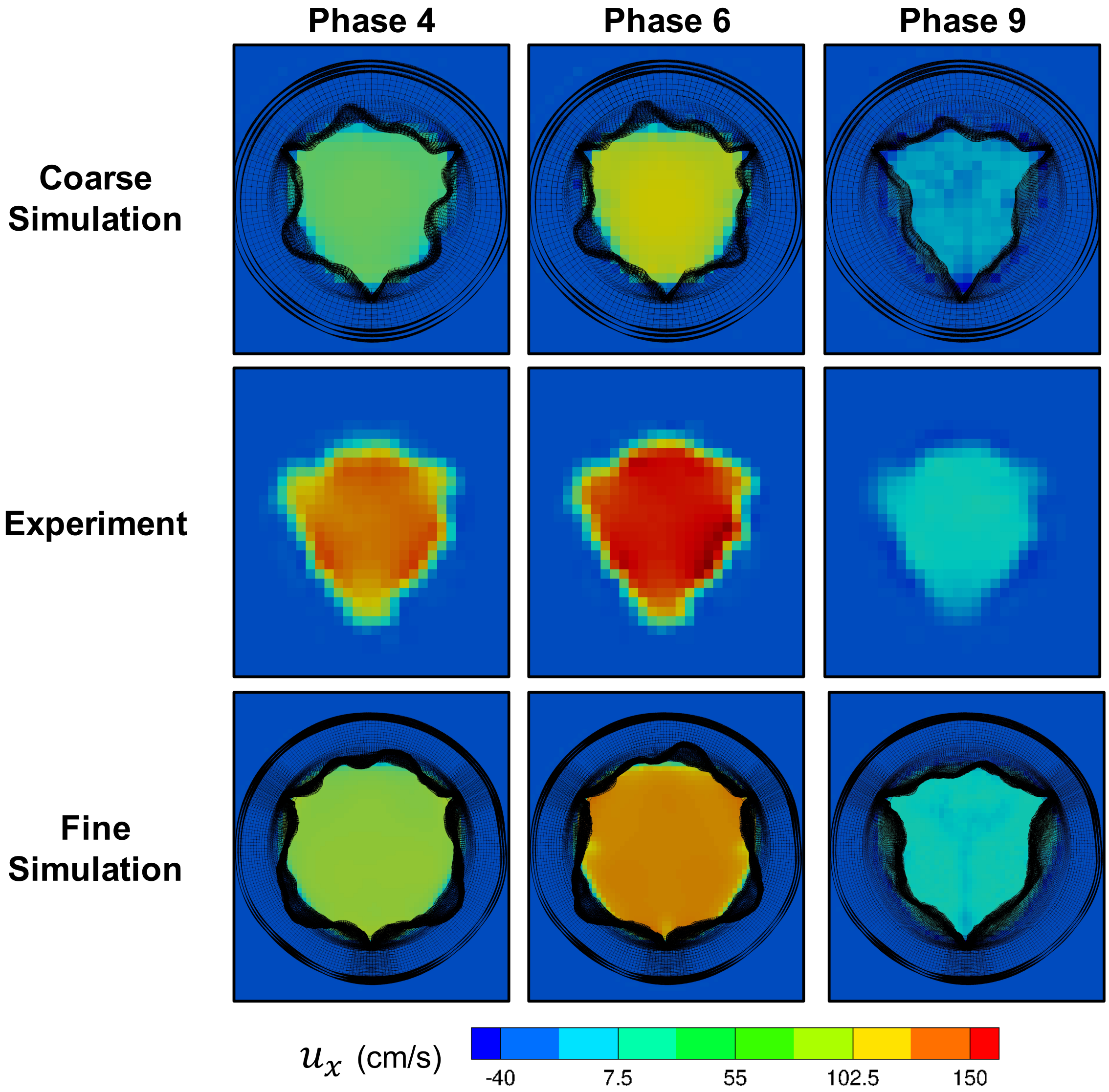

Figure 6.6: Contours of the x-component of velocity in the coarse resolution simulation (top row), experiment (middle row), and fine resolution simulation (bottom row) at axial slice x = 0 for phases 4, 6, and 9 of the cardiac cycle.

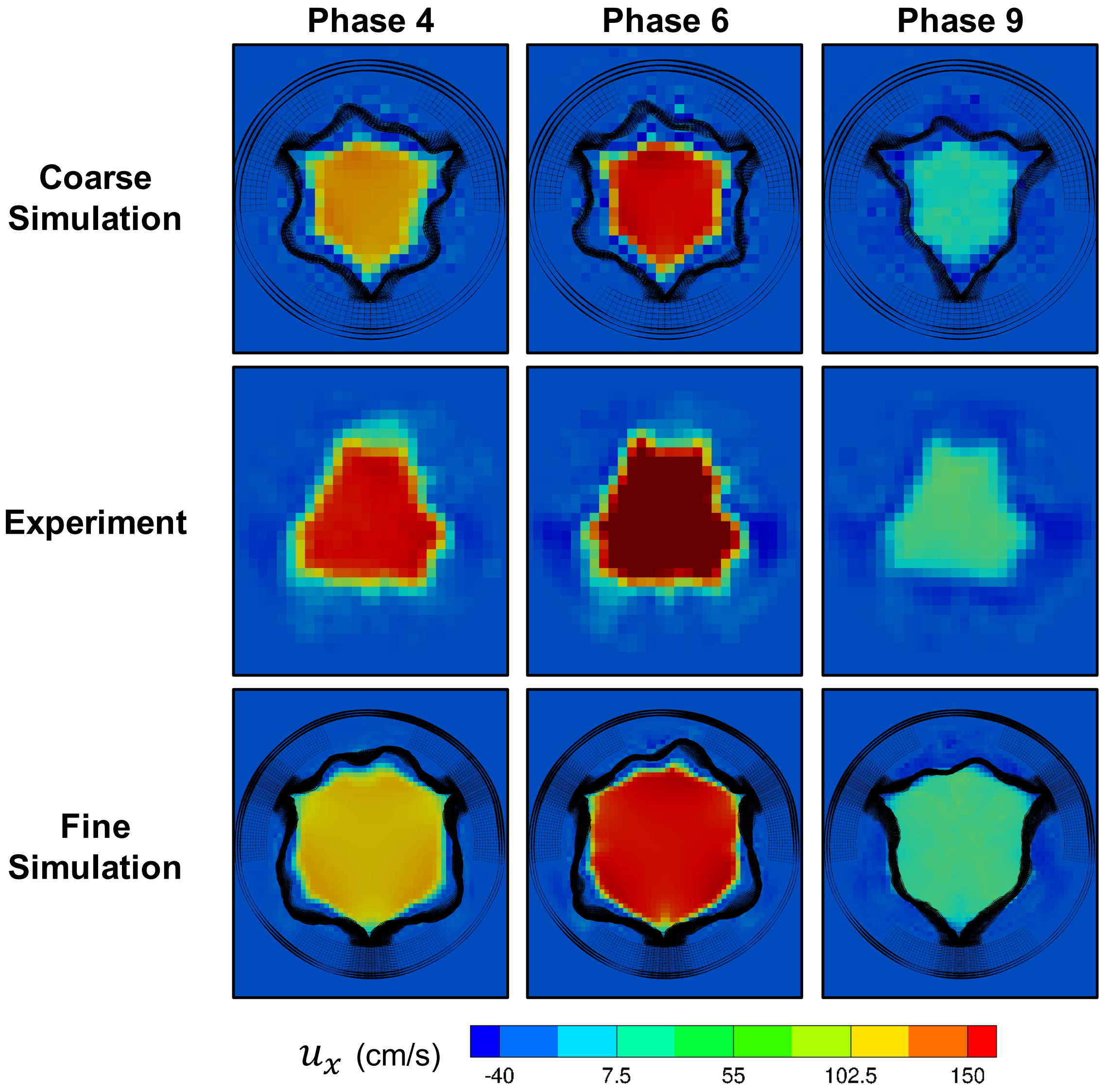

Figure 6.7: Contours of the x-component of velocity in the coarse resolution simulation (top row), experiment (middle row), and fine resolution simulation (bottom row) at axial slice x/D = 0.25 for phases 4, 6, and 9 of the cardiac cycle.

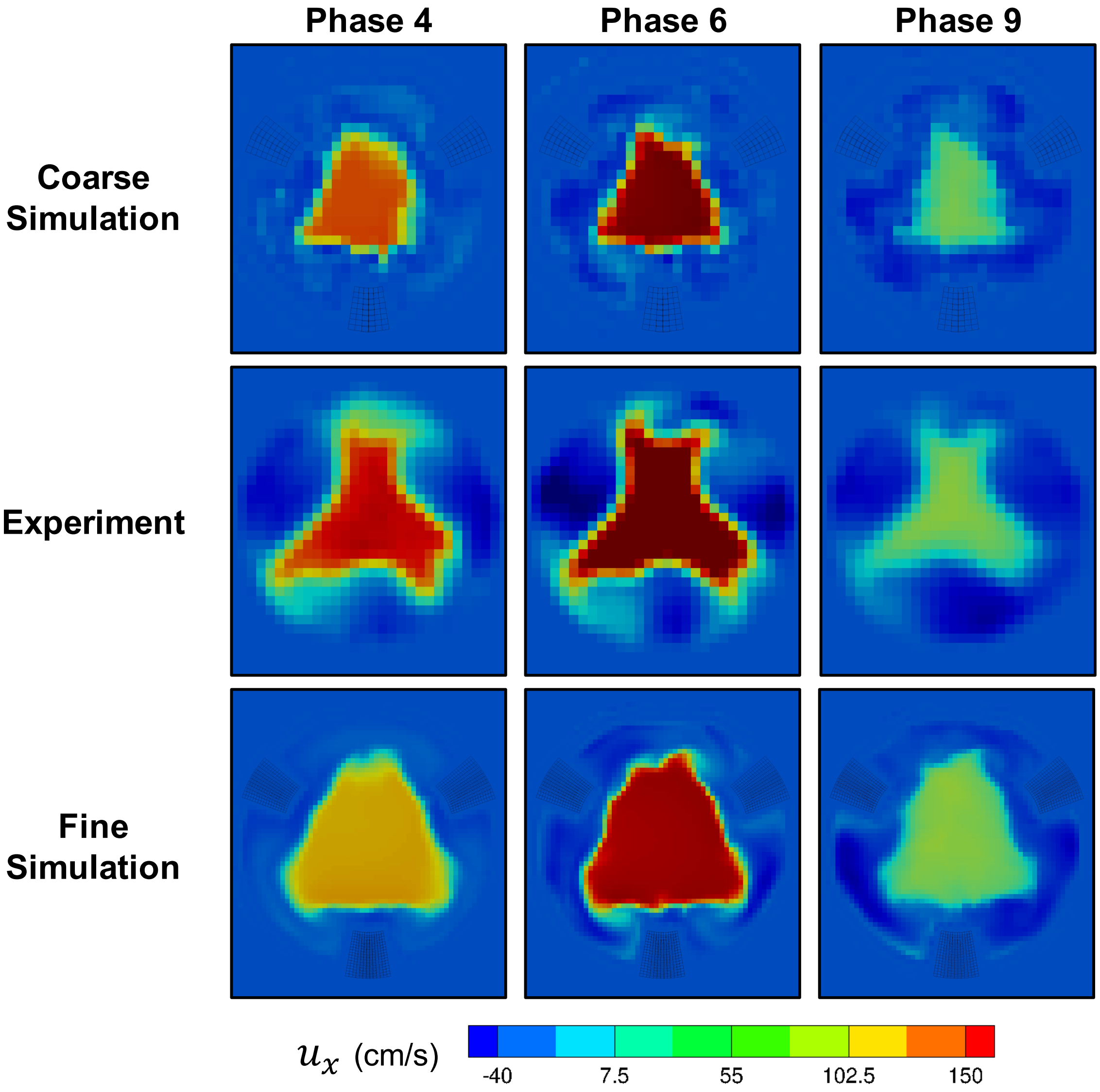

Figure 6.8: Contours of the x-component of velocity in the coarse resolution simulation (top row), experiment (middle row), and fine resolution simulation (bottom row) at axial slice x/D = 0.5 for phases 4, 6, and 9 of the cardiac cycle.

6.4 Conclusions

The experiments conducted in this work were designed with simulation validation in mind, as there is a lack of high quality data in the literature for valve modeling comparisons in realistic anatomies. The collaborative work in this chapter demonstrated the successful use of the healthy control RVOT model in validating a design-based model for the pulmonary valve. The 3D printed geometry was easily reproduced in the simulation framework and the coarse simulation was set up to exactly replicate the Cartesian grid and coordination system of the experimental data.

The simulations captured key features in the experimental velocity fields, particularly in the angle of the jet and formation of reversed flow regions. Though some features of the jet shape were not replicated by the simulations, the overall accuracy of the flow fields demonstrated that the framework was able to simulate the valve leaflet motion of the bioprosthetic valve in the experiment.

This work is ongoing, as we are developing outlet boundary conditions that will incorporate resistance and capacitance elements to match the conditions downstream of the model in the experimental flow loop. In addition, we will expand our comparisons with quantitative metrics including the volume of reversed flow in the model and integral metrics for streamwise momentum and secondary flow strength. The Cartesian grid of the experimental data and its direct alignment with the simulation mesh will facilitate quantitative comparisons of the two methods.

Chapter 7

Conclusions

7.1 Overview

Patients with ToF typically undergo PVR in their early teen years to alleviate pulmonary regurgitation and RV dysfunction after the initial ToF repair. The bioprosthetic surgical valves most commonly used in this procedure are expected to last 10 - 15 years. However, these valves fail early and unpredictably in many ToF patients. Despite extensive clinical experience, the hemodynamic and anatomical factors that may predispose valves for failure remain poorly understood. This thesis examined the effects of anatomy, cardiac output, valve position, and valve orientation on RVOT hemodynamics in experimental models. We found that each of these factors had a substantial impact on the flow features local to the bioprosthetic valve, including recirculation, reversed flow regions, jet angle and impingement on the vessel wall, and the effective orifice area of the valve.

In this work, we designed four anatomical models of the RVOT from the RV exit to the first PA bifurcation: a healthy control model to serve as a baseline, a diseased model with a dilated MPA, and two diseased models with an acute angle between the RV and the MPA, one with the valve aligned with the RV and the other with the valve aligned with the MPA. We studied two different valve orientations in all of these models and examined three different cardiac outputs in the dilated MPA model. We developed a physiological flow loop to run pulsatile flow through the RVOT models. For each configuration, we conducted 4D flow MRI experiments to obtain the full 3D, three component, time-averaged velocity fields in the model. This series of experiments provided extensive data on how the RVOT hemodynamics were impacted by a range of anatomies and valve positions.

7.1.1 Effects of RVOT Anatomy

We conducted 4D flow MRI experiments in the healthy control model and the dilated MPA model of the RVOT to study the effects of anatomy on the flow fields over the cardiac cycle. For each model, we placed the valve in the native orientation and in a second orientation rotated 180 degrees. All four cases had a cardiac output of 3.5 L/min.

The flow fields for each of these four cases had drastic differences. The dilated vessel in the diseased case led to stronger regions of recirculation and increased reversed flow volume through the cardiac cycle when compared to the healthy anatomy. In the healthy anatomy case, we observed a small region of reversed flow along the interior curve of the vessel that may actually assist in valve closure (Yoganathan et al., 2005). In the dilated MPA with the native valve orientation, the reversed flow along the inner curve developed further downstream, far from the valve annulus. When we changed to the rotated orientation in this anatomy, the reversed flow region along the interior curve was in the same location as the healthy case. However, this recovery of this reversed flow location was accompanied by a new large region of reversed flow along the outer vessel wall. This illustrated the complex impact of valve orientation on the flow fields, as both favorable and unfavorable flow features were produced by the rotated orientation in the dilated MPA case.

One of the key findings from these four cases was that the RVOT anatomy and the valve orientation have compound effects on the resulting flow fields. The effects of changing the valve orientation in one anatomy were not necessarily replicated in the other anatomy. We quantified this effect in the secondary flow strength metric I_2. In the healthy anatomy, the I_2 values were similar over the cardiac cycle for both valve orientations. In the dilated anatomy, the rotated orientation had stronger secondary flows that peaked later and lasted longer in the cardiac cycle than the native orientation. This indicated that determining what valve orientation may produce the most favorable hemodynamic environment for valve performance is likely dependent on the patient specific anatomy. A general surgical guideline, such as always placing the valve in the native orientation for all patients, may not lead to optimal hemodynamics and outcomes in all cases. For example, our research suggests that placing the valve in the 180 degrees rotated orientation in a dilated MPA anatomy will recover some of the flow features seen in the healthy anatomy.

7.1.2 Effects of Cardiac Output

We conducted five 4D flow MRI experiments in the dilated MPA model to study the impact of cardiac output on hemodynamics. Cardiac outputs of 2 L/min, 3.5 L/min, and 5 L/min with the native orientation and cardiac outputs of 2 L/min and 3.5 L/min with the rotated orientation were examined. We used high-speed imaging experiments to obtain the instantaneous valve leaflet motion for all three cardiac outputs, each with both valve orientations. Varying the cardiac output through the same 25mm valve corresponds to the clinical decision of valve sizing during PVR surgery. The 2 L/min case corresponded to valve oversizing, the 3.5 L/min case was a standard valve sizing, and the 5 L/min case represented valve undersizing. The effects of valve oversizing on long-term outcomes are an open question in the clinical literature. Some surgeons oversize the valve in younger patients in order to allow for patient growth, but some studies have found that oversizing is associated with earlier valve dysfunction (Batlivala et al., 2012; Chen et al., 2012; Askovich et al., 2007).

In our experiments, the 5 L/min case produced the most symmetric flow and the largest valve orifice area, indicating the most efficient use of the 25mm valve. In contrast, the 2 L/min cases, with the native and the rotated orientation, had multiple features that may lead to early valve failure. The flow fields had stronger regions of recirculation and a highly asymmetric jet through the valve, which may make the valve more prone to calcification and uneven leaflet fatigue. The valve leaflets did not fully open with the 2 L/min cardiac output and the 2 L/min cases had the smallest valve orifice area. The locations where portions of the leaflets did not open corresponded directly to the recirculation regions and asymmetry in the flow fields. In addition, the free edges of the leaflets did not fully separate at the commissures, meaning they may be more likely to fuse due to calcification, which commonly occurs at commissures. Thus, our experiments found that the 2 L/min case produced adverse hemodynamic features and leaflet behaviors. All of these indicate that valve oversizing may actually predispose the valve for early failure, mitigating any potential benefits from allowing the patient to grow into the valve.

7.1.3 Effects of Valve Position

A common anatomical variation in ToF patients is an acute angle between the RV and the MPA. This presents surgeons with a critical decision in where to place the valve in the vessel. The most common options are to align the valve with the RV, upstream of the curvature, or to align the valve with the MPA, downstream of the curvature. We represented these valve positions in two models of the RVOT with acute curvature. We conducted 4D flow MRI experiments on both models, each with the native and rotated orientation, at a cardiac output of 3.5 L/min.

The valve alignment drastically affected the resulting flow fields, with each case resulting in a different jet direction in the RVOT. In the case with the valve aligned with the MPA, the jet impinged on the vessel wall above the bifurcation with the native orientation. When the valve was aligned with the RV, the jet impacted the vessel wall closer to the valve annulus as the flow encountered the acute curvature. The location and amount of reversed flow were also substantially different between the two cases. In both orientations with the valve aligned with the RV, reversed flow developed along the inner and outer curves of the vessel, similar to the dilated MPA model. In contrast, when the valve was aligned with the MPA, large reversed flow regions were produced around the entire vessel wall, with the exception of the inner curve. Overall, varying the valve alignment produced significantly different flow fields. The differences between the valve alignment cases were even more substantial than the differences between the healthy and dilated MPA anatomy and the varying cardiac outputs. Thus, valve position in anatomies with acute curvature is a critical decision during PVR.

The valve orientation within a given alignment had a significant impact on the jet angle and direction. In both cases, rotating the valve orientation lessened the jet impingement by redirecting the jet through the valve. This was particularly interesting in the valve aligned with the MPA case. With the rotated orientation, the jet impingement on the vessel wall was almost entirely eliminated, as the flow was directed downwards towards the PA branches instead. This could have a substantial clinical impact, since jet impingement may lead to adverse vessel remodeling and PA dilation. In the case with the rotated orientation, we observed slightly larger reversed flow regions, but few other adverse hemodynamic features. Thus, for this particular anatomy, we were able to identify a valve position and orientation that produced an overall favorable hemodynamic environment.

7.1.4 Simulation Validation

The experiments conducted in this work produced high quality data sets that can be used to validate computational valve models. The 3D printed model designs can be easily imported into a simulation framework and the specifications of the valve leaflets, support structure, and exact position in the vessel are known. The MRI experiments result in 3D data on a Cartesian grid that can be directly compared with simulations, allowing for precise comparison of the flow fields. We used the healthy anatomy with the native orientation to validate the valve modeling methodology developed by Kaiser et al. (2021).

The simulation flow fields matched well with the experimental data, particularly in producing the correct jet angle out of the valve annulus and the reversed flow regions along the inner curve of the vessel wall. However, in initial comparisons, the speed of the jet was underestimated in the simulations and the triangular shape of the experimental jet was not captured. Improvements will be made to the simulation boundary conditions to better replicate the downstream resistance and capacitance of the experimental flow loop, which might lead to better matching between velocity fields. In addition, the high quality experimental data will facilitate quantitative comparisons with the simulation data.

7.2 Implications and Future Directions

There are currently no standard clinical guidelines for how to place the bioprosthetic valve during PVR surgery. This work demonstrated that the valve position and orientation within a given anatomy had a substantial impact on the flow fields. Certain configurations of anatomy, cardiac output, orientation, and position produced flow features, such as stronger recirculation and jet impingement, that are associated with modes of valve failure and adverse vessel remodeling. In addition, the effect of changing the valve orientation differed depending of the RVOT anatomy and cardiac output. These results highlight the need for guidelines on how to place the valve based on the patient-specific anatomy. Standardizing valve placement to produce favorable hemodynamics in the RVOT after PVR could help prevent early bioprosthetic valve failure in the ToF patient population.

Future experiments could be conducted to assess inter-valve variability. Conducting experiments with multiple valves would identify any features that might be unique to a particular valve as opposed to position and orientation with the anatomy. Additional experiments could use RVOT models made of compliant material to assess how native vessel material properties impact the flow fields. Future work is planned to fully validate the valve model discussed in Chapter 6. A wider range of RVOT anatomies, including patient-specific cases, and valve positions within those anatomies could be studied with a series of simulations to provide more insights on how these factors impact the hemodynamics. A primary long-term future direction of this work would be to develop a simulation tool that could assist clinicians in planning PVR by testing different valve position options in the patients anatomy before the surgery.

Another significant future direction would be determining which flow features are associated with long-term patient outcomes using *in vivo* data. Prospective clinical studies could use 4D flow MRI data taken after PVR to assess hemodynamics in a cohort of patients. Following the patients for years after the PVR procedure would identify which patients experienced early valve dysfunction. The combination of the hemodynamic data and the long-term outcomes in a cohort of patients would demonstrate which flow features were associated with early failure. The analysis and metrics developed in this thesis could be translated to patient 4D flow MRI to quantify the hemodynamic features. A clinical study of this nature would determine the optimal hemodynamic environment for long-term valve function. This information could be combined with the knowledge developed in this work and future experiments on how valve position and orientation within patient-specific anatomies with physiological material properties affect the hemodynamics. Thus, this would aid clinicians in determining the optimal bioprosthetic valve placement for long-term performance.

Bibliography

Veronica Toro Arana, Frandics P. Chan, Jin Long, Nicole K. Schiavone, Sushma Reddy, Frank L. Hanley, Amy Lin, Alison L. Marsden, and Doff B. McElhinney. Geometric Variability of the RVOT in Patients with Tetralogy of Fallot Undergoing Pulmonary Valve Replacement. *Pediatr Cardiol*, 2021. In submission.

Bojana Askovich, John A. Hawkins, C. Todd Sower, L. LuAnn Minich, Lloyd Y. Tani, Greg Stoddard, and Michael D. Puchalski. Right Ventricle–to–Pulmonary Artery Conduit Longevity: Is it Related to Allograft Size? *The Annals of Thoracic Surgery*, 84(3):907–912, September 2007. ISSN 0003-4975. doi: 10.1016/j.athoracsur.2007.04.104. URL `https://www.sciencedirect.com/science/article/pii/S000349750700954X`.

Sonya V. Babu-Narayan, Gerhard-Paul Diller, Radu R. Gheta, Anthony J. Bastin, Theodoros Karonis, Wei Li, Dudley J. Pennell, Hideki Uemura, Babulal Sethia, Michael A. Gatzoulis, and Darryl F. Shore. Clinical Outcomes of Surgical Pulmonary Valve Replacement After Repair of Tetralogy of Fallot and Potential Prognostic Value of Preoperative Cardiopulmonary Exercise Testing. *Circulation*, 129(1):18–27, January 2014. ISSN 0009-7322, 1524-4539. doi: 10.1161/CIRCULATIONAHA.113.001485. URL `https://www.ahajournals.org/doi/10.1161/CIRCULATIONAHA.113.001485`.

Sripal Bangalore and Deepak L. Bhatt. Right Heart Catheterization, Coronary Angiography, and Percutaneous Coronary Intervention. *Circulation*, 124(17):e428–e433, October 2011. doi: 10.1161/CIRCULATIONAHA.111.065219.

A. J. Banko, F. Coletti, D. Schiavazzi, C. J. Elkins, and J. K. Eaton. Three-dimensional inspiratory flow in the upper and central human airways. *Exp Fluids*, 56(6):117, May 2015. ISSN 1432-1114. doi: 10.1007/s00348-015-1966-y. URL `https://doi.org/10.1007/s00348-015-1966-y`.

Andrew J. Banko, Filippo Coletti, Christopher J. Elkins, and John K. Eaton. Oscillatory flow in the human airways from the mouth through several bronchial generations. *International Journal of Heat and Fluid Flow*, 61:45–57, October 2016. ISSN 0142-727X. doi: 10.1016/j.ijheatfluidflow.2016.04.006. URL `://WOS:000390745800006`.

Vinayak N. Bapat, Rizwan Attia, and Martyn Thomas. Effect of valve design on the stent internal diameter of a bioprosthetic valve: a concept of true internal diameter and its implications for the valve-in-valve procedure. *JACC Cardiovasc Interv*, 7 (2):115–127, February 2014. ISSN 1876-7605. doi: 10.1016/j.jcin.2013.10.012.

Alex J. Barker, Alejandro Roldán-Alzate, Pegah Entezari, Sanjiv J. Shah, Naomi C. Chesler, Oliver Wieben, Michael Markl, and Christopher J. François. Four-dimensional flow assessment of pulmonary artery flow and wall shear stress in adult pulmonary arterial hypertension: results from two institutions. *Magn Reson Med*, 73(5):1904–1913, May 2015. ISSN 1522-2594. doi: 10.1002/mrm.25326.

Roger J. F Baskett, Maurice A Nanton, Andrew E Warren, and David B Ross. Human leukocyte antigen-DR and ABO mismatch are associated with accelerated homograft valve failure in children: implications for therapeutic interventions. *The Journal of Thoracic and Cardiovascular Surgery*, 126(1):232–238, July 2003. ISSN 0022-5223. doi: 10.1016/S0022-5223(03)00210-1. URL `http://www.sciencedirect.com/science/article/pii/S0022522303002101`.

Sarosh P. Batlivala, Sitaram Emani, John E. Mayer, and Doff B. McElhinney. Pulmonary Valve Replacement Function in Adolescents: A Comparison of Bioprosthetic Valves and Homograft Conduits. *The Annals of Thoracic Surgery*, 93(6):2007–2016, June

2012. ISSN 0003-4975. doi: 10.1016/j.athoracsur.2012.02.039. URL `http://www.sciencedirect.com/science/article/pii/S0003497512003980`.

Odd Bech-Hanssen, Kenneth Caidahl, Ingemar Wallentin, Per Ask, and Bengt Wranne. Assessment of effective orifice area of prosthetic aortic valves with Doppler echocardiography: An in vivo and in vitro study. *The Journal of Thoracic and Cardiovascular Surgery*, 122(2):287–295, August 2001. ISSN 0022-5223. doi: 10.1067/mtc.2001.115161. URL `https://www.sciencedirect.com/science/article/pii/S002252230149283X`.

Hamid Bigdelian, Davoud Mardani, and Mohsen Sedighi. The Effect of Pulmonary Valve Replacement (PVR) Surgery on Hemodynamics of Patients Who Underwent Repair of Tetralogy of Fallot (TOF). *J Cardiovasc Thorac Res*, 7(3):122–125, 2015. ISSN 2008-5117. doi: 10.15171/jcvtr.2015.26. URL `https://www.ncbi.nlm.nih.gov/pmc/articles/PMC4586599/`.

Giovanni Biglino, Alessandro Giardini, Tain-Yen Hsia, Richard Figliola, Andrew M. Taylor, Silvia Schievano, and MOCHA Collaborative Group. Modeling single ventricle physiology: review of engineering tools to study first stage palliation of hypoplastic left heart syndrome. *Front Pediatr*, 1:31, October 2013a. ISSN 2296-2360. doi: 10.3389/fped.2013.00031.

Giovanni Biglino, Peter Verschueren, Raf Zegels, Andrew M. Taylor, and Silvia Schievano. Rapid prototyping compliant arterial phantoms for in-vitro studies and device testing. *Journal of Cardiovascular Magnetic Resonance*, 15(1): 2, January 2013b. ISSN 1532-429X. doi: 10.1186/1532-429X-15-2. URL `https://doi.org/10.1186/1532-429X-15-2`.

A. Blalock and H. B. Taussig. Landmark article May 19, 1945: The surgical treatment of malformations of the heart in which there is pulmonary stenosis or pulmonary atresia. By Alfred Blalock and Helen B. Taussig. *JAMA*, 251(16):2123–2138, April 1984. ISSN 0098-7484. doi: 10.1001/jama.251.16.2123.

Philipp Bonhoeffer, Younes Boudjemline, Zakhia Saliba, Jacques Merckx, Yacine Aggoun, Damien Bonnet, Philippe Acar, Jérôme Le Bidois, Daniel Sidi, and Jean Kachaner. Percutaneous replacement of pulmonary valve in a right-ventricle to pulmonary-artery prosthetic conduit with valve dysfunction. *The Lancet*, 356(9239):1403–1405, October 2000. ISSN 0140-6736. doi: 10.1016/S0140-6736(00)02844-0. URL `https://www.sciencedirect.com/science/article/pii/S0140673600028440`.

Younes Boudjemline, Georgia Brugada, Isabelle Van-Aerschot, Mehul Patel, Adeline Basquin, Caroline Bonnet, Antoine Legendre, Damien Bonnet, and Laurence Iserin. Outcomes and safety of transcatheter pulmonary valve replacement in patients with large patched right ventricular outflow tracts. *Archives of Cardiovascular Diseases*, 105(8):404–413, August 2012. ISSN 1875-2136. doi: 10.1016/j.acvd.2012.05.002. URL `https://www.sciencedirect.com/science/article/pii/S1875213612001428`.

Berto J. Bouma and Barbara J.M. Mulder. Changing Landscape of Congenital Heart Disease. *Circulation Research*, 120(6):908–922, March 2017. doi: 10.1161/CIRCRESAHA.116.309302. URL `https://www.ahajournals.org/doi/10.1161/CIRCRESAHA.116.309302`. Publisher: American Heart Association.

Neil W Bressloff. Parametric geometry exploration of the human carotid artery bifurcation. *Journal of Biomechanics*, 40(11):2483–2491, January 2007. ISSN 0021-9290. doi: 10.1016/j.jbiomech.2006.11.002. URL `http://www.sciencedirect.com/science/article/pii/S0021929006004398`. Publisher: Elsevier.

Margarita Brida and Michael A. Gatzoulis. Adult congenital heart disease: Past, present, future. *International Journal of Cardiology Congenital Heart Disease*, 1:100052, July 2020. ISSN 2666-6685. doi: 10.1016/j.ijcchd.2020.100052. URL `https://www.sciencedirect.com/science/article/pii/S2666668520300525`.

Jagdish Butany and Richard Leask. The Failure Modes of Biological Prosthetic Heart Valves. *JLT*, 11(3&4), 2001. ISSN 1050-6934, 1940-4379. doi: 10.1615/JLongTermEffMedImplants.v11.i34.30. Publisher: Begel House Inc.

Pablo Bächler, Natalia Pinochet, Julio Sotelo, Gérard Crelier, Pablo Irarrazaval, Cristián Tejos, and Sergio Uribe. Assessment of normal flow patterns in the pulmonary circulation by using 4D magnetic resonance velocity mapping. *Magnetic Resonance Imaging*, 31(2):178–188, February 2013. ISSN 0730-725X. doi: 10.1016/j.mri.2012.06.036. URL `http://www.sciencedirect.com/science/article/pii/S0730725X12002469`.

T. A. Camp, K. C. Stewart, R. S. Figliola, and T. McQuinn. In vitro study of flow regulation for pulmonary insufficiency. *J Biomech Eng*, 129(2):284–288, April 2007. ISSN 0148-0731. doi: 10.1115/1.2540892.

Qi-Ling Cao, Damien Kenny, Daxin Zhou, Wenzhi Pan, Lihua Guan, Junbo Ge, and Ziyad M. Hijazi. Early clinical experience with a novel self-expanding percutaneous stent-valve in the native right ventricular outflow tract. *Catheterization and Cardiovascular Interventions*, 84 (7):1131–1137, 2014. ISSN 1522-726X. doi: 10.1002/ccd.25544. URL `https://onlinelibrary.wiley.com/doi/abs/10.1002/ccd.25544`. _eprint: https://onlinelibrary.wiley.com/doi/pdf/10.1002/ccd.25544.

Francesco Capuano, Yue-Hin Loke, and Elias Balaras. Blood Flow Dynamics at the Pulmonary Artery Bifurcation. *Fluids*, 4(4):190, December 2019. doi: 10.3390/fluids4040190. URL `https://www.mdpi.com/2311-5521/4/4/190`.

Peter C. Chen, Maggie S. Sager, David Zurakowski, Frank A. Pigula, Christopher W. Baird, John E. Mayer, Pedro J. del Nido, and Sitaram M. Emani. Younger age and valve oversizing are predictors of structural valve deterioration after pulmonary valve replacement in patients with tetralogy of Fallot. *The Journal of Thoracic and Cardiovascular Surgery*, 143(2):352–360, February 2012. ISSN 0022-5223. doi: 10.1016/j.jtcvs.2011.10.079. URL `http://www.sciencedirect.com/science/article/pii/S002252231101244X`.

Christopher P. Cheng, Robert J. Herfkens, Charles A. Taylor, and Jeffrey A. Feinstein. Proximal pulmonary artery blood flow characteristics in healthy subjects measured in an upright posture using MRI: The effects of exercise and age. *Journal of Magnetic Resonance Imaging*, 21 (6):752–758, 2005. ISSN 1522-2586. doi: 10.1002/jmri.20333. URL `https://onlinelibrary.wiley.com/doi/abs/10.1002/jmri.20333`.

Ming-Jyh Chern, Ming-Ting Wu, and Sheau-Wei Her. Numerical Study for Blood Flow in Pulmonary Arteries after Repair of Tetralogy of Fallot. *Computational and Mathematical Methods in Medicine*, 2012:e198108, December 2012. ISSN 1748-670X. doi: 10.1155/2012/198108. URL `https://www.hindawi.com/journals/cmmm/2012/198108/`. Publisher: Hindawi.

M.J. Chern, Wu Mt, and Wang Hl. Numerical investigation of regurgitation phenomena in pulmonary arteries of Tetralogy of Fallot patients after repair. *J Biomech*, 41(14):3002–3009, September 2008. ISSN 0021-9290, 1873-2380. doi: 10.1016/j.jbiomech.2008.07.017. URL `https://europepmc.org/article/med/18771769`.

Sherman C. P. Cheung, Kelvin K. L. Wong, Guan Heng Yeoh, William Yang, Jiyuan Tu, Richard Beare, and Thanh Phan. Experimental and numerical study on the hemodynamics of stenosed carotid bifurcation. *Australas Phys Eng Sci Med*, 33(4): 319–328, December 2010. ISSN 1879-5447. doi: 10.1007/s13246-010-0050-4. URL `https://doi.org/10.1007/s13246-010-0050-4`.

Jan T. Christenson, Dominique Vala, Jorge Sierra, Maurice Beghetti, and Afksendiyos Kalangos. Blood group incompatibility and accelerated homograft fibrocalcifications. *The Journal of Thoracic and Cardiovascular Surgery*, 127(1): 242–250, January 2004. ISSN 0022-5223. doi: 10.1016/j.jtcvs.2003.07.047. URL `http://www.sciencedirect.com/science/article/pii/S0022522303016027`.

Ashish Das, William Gottliebson, Madhra Karve, and Rupak K. Banerjee. Assessment of Energy Loss due to Pulmonary Valve Insufficiency in Tetralogy of Fallot

Physiology Using Patient Specific Geometry. In *ASME 2010 Summer Bioengineering Conference, Parts A and B*, pages 245–246, Naples, Florida, USA, June 2010. American Society of Mechanical Engineers. ISBN 978-0-7918-4403-8. doi: 10.1115/SBC2010-19631.

Lakshmi P Dasi, Helene A Simon, Philippe Sucosky, and Ajit P Yoganathan. FLUID MECHANICS OF ARTIFICIAL HEART VALVES. *Clin Exp Pharmacol Physiol*, 36(2):225–237, February 2009. ISSN 0305-1870. doi: 10.1111/j.1440-1681.2008.05099.x. URL `https://www.ncbi.nlm.nih.gov/pmc/articles/PMC2752693/`.

G. Michael Deeb, Michael J. Reardon, Stan Chetcuti, Himanshu J. Patel, P. Michael Grossman, Steven J. Yakubov, Neal S. Kleiman, Joseph S. Coselli, Thomas G. Gleason, Joon Sup Lee, James B. Hermiller, John Heiser, William Merhi, George L. Zorn, Peter Tadros, Newell Robinson, George Petrossian, G. Chad Hughes, J. Kevin Harrison, Brijeshwar Maini, Mubashir Mumtaz, John Conte, Jon Resar, Vicken Aharonian, Thomas Pfeffer, Jae K. Oh, Hongyan Qiao, David H. Adams, and Jeffrey J. Popma. 3-Year Outcomes in High-Risk Patients Who Underwent Surgical or Transcatheter Aortic Valve Replacement. *Journal of the American College of Cardiology*, 67(22):2565–2574, June 2016. ISSN 0735-1097. doi: 10.1016/j.jacc.2016.03.506. URL `https://www.sciencedirect.com/science/article/pii/S0735109716016909`.

Michael P. DiLorenzo, Okan U. Elci, Yan Wang, Anirban Banerjee, Tomoyuki Sato, Bonnie Ky, Elizabeth Goldmuntz, and Laura Mercer-Rosa. Longitudinal Changes in Right Ventricular Function in Tetralogy of Fallot in the Initial Years after Surgical Repair. *J Am Soc Echocardiogr*, 31(7):816–821, 2018. ISSN 1097-6795. doi: 10.1016/j.echo.2018.02.013.

Andras P. Durko, Stuart J. Head, Philippe Pibarot, Pavan Atluri, Vinayak Bapat, Duke E. Cameron, Filip P. A. Casselman, Edward P. Chen, Gry Dahle, Tjark Ebels, John A. Elefteriades, Patrizio Lancellotti, Richard L. Prager, Raphael Rosenhek, Alan Speir, Marco Stijnen, Giordano Tasca, Ajit Yoganathan, Thomas

Walther, and Ruggero De Paulis. Characteristics of surgical prosthetic heart valves and problems around labeling: A document from the European Association for Cardio-Thoracic Surgery (EACTS)—The Society of Thoracic Surgeons (STS)—American Association for Thoracic Surgery (AATS) Valve Labelling Task Force. *The Journal of Thoracic and Cardiovascular Surgery*, 158(4):1041–1054, October 2019. ISSN 0022-5223. doi: 10.1016/j.jtcvs.2019.04.001. URL `https://www.sciencedirect.com/science/article/pii/S0022522319307755`.

C. J. Elkins, M. Markl, N. Pelc, and J. K. Eaton. 4D Magnetic resonance velocimetry for mean velocity measurements in complex turbulent flows. *Exp Fluids*, 34 (4):494–503, April 2003. ISSN 1432-1114. doi: 10.1007/s00348-003-0587-z. URL `https://doi.org/10.1007/s00348-003-0587-z`.

Christopher J. Elkins and Marcus T. Alley. Magnetic resonance velocimetry: applications of magnetic resonance imaging in the measurement of fluid motion. *Experiments in Fluids*, 43(6):823–858, December 2007. ISSN 0723-4864. doi: 10.1007/s00348-007-0383-2. URL `://WOS:000251010400001`.

Richard S. Figliola, Alessandro Giardini, Tim Conover, Tiffany A. Camp, Giovanni Biglino, John Chiulli, and Tain-Yen Hsia. In Vitro Simulation and Validation of the Circulation with Congenital Heart Defects. *Prog. Pediatr. Cardiol.*, 30(1-2): 71–80, December 2010. ISSN 1058-9813. doi: 10.1016/j.ppedcard.2010.09.009.

Christopher J. François, Shardha Srinivasan, Mark L. Schiebler, Scott B. Reeder, Eric Niespodzany, Benjamin R. Landgraf, Oliver Wieben, and Alex Frydrychowicz. 4D cardiovascular magnetic resonance velocity mapping of alterations of right heart flow patterns and main pulmonary artery hemodynamics in tetralogy of Fallot. *J Cardiovasc Magn Reson*, 14:16, February 2012. ISSN 1532-429X. doi: 10.1186/1532-429X-14-16.

Alessandro Frigiola, Alessandro Giamberti, Massimo Chessa, Marisa Di Donato, Raul Abella, Sara Foresti, Concettina Carlucci, Diana Negura, Mario Carminati, Gerald Buckberg, Lorenzo Menicanti, and the RESTORE group. Right ventricular restoration during pulmonary valve implantation in adults with congenital heart disease. *European Journal of Cardio-Thoracic Surgery*, 29(Supplement_1): S279–S285, April 2006. ISSN 1010-7940. doi: 10.1016/j.ejcts.2006.03.007. URL `https://doi.org/10.1016/j.ejcts.2006.03.007`.

Stephanie Fuller. Tetralogy of Fallot and Pulmonary Valve Replacement: Timing and Techniques in the Asymptomatic Patient. *Seminars in Thoracic and Cardiovascular Surgery: Pediatric Cardiac Surgery Annual*, 17(1):30–37, January 2014. ISSN 1092-9126. doi: 10.1053/j.pcsu.2014.01.012. URL `https://www.sciencedirect.com/science/article/pii/S1092912614000131`.

Damien Garcia, Philippe Pibarot, Champlain Landry, Amélie Allard, Boris Chayer, Jean G. Dumesnil, and Louis-Gilles Durand. Estimation of aortic valve effective orifice area by Doppler echocardiography: effects of valve inflow shape and flow rate. *Journal of the American Society of Echocardiography*, 17(7):756–765, July 2004. ISSN 0894-7317, 1097-6795. doi: 10.1016/j.echo.2004.03.030. URL `https://www.onlinejase.com/article/S0894-7317(04)00310-4/abstract`. Publisher: Elsevier.

Aungkana Gengsakul, Louise Harris, Timothy J. Bradley, Gary D. Webb, William G. Williams, Samuel C. Siu, Naeem Merchant, and Brian W. McCrindle. The impact of pulmonary valve replacement after tetralogy of Fallot repair: a matched comparison. *European Journal of Cardio-Thoracic Surgery*, 32(3):462–468, September 2007. ISSN 1010-7940. doi: 10.1016/j.ejcts.2007.06.009. URL `https://doi.org/10.1016/j.ejcts.2007.06.009`.

Tal Geva. Repaired tetralogy of Fallot: the roles of cardiovascular magnetic resonance in evaluating pathophysiology and for pulmonary valve replacement decision support. *Journal of Cardiovascular Magnetic Resonance*, 13 (1):9, January 2011. ISSN 1532-429X. doi: 10.1186/1532-429X-13-9. URL `https://doi.org/10.1186/1532-429X-13-9`.

Suzanne M. Gilboa, Owen J. Devine, James E. Kucik, Matthew E. Oster, Tiffany Riehle-Colarusso, Wendy N. Nembhard, Ping Xu, Adolfo Correa, Kathy Jenkins, and Ariane J. Marelli. Congenital Heart Defects in the United States: Estimating the Magnitude of the Affected Population in 2010. *Circulation*, 134(2):101–109, July 2016. ISSN 1524-4539. doi: 10.1161/CIRCULATIONAHA.115.019307.

Jeffrey Gohean, Richard Figliola, Tiffany Camp, and Tim McQuinn. Comparative in vitro study of bileaflet and tilting disk valve behavior in the pulmonary position. *J Biomech Eng*, 128(4):631–635, August 2006. ISSN 0148-0731. doi: 10.1115/1.2206204.

B. E. Griffith. IBAMR: Immersed boundary adaptive mesh refinement, August 2021. URL `https://github.com/IBAMR/IBAMR`. original-date: 2014-04-18T03:50:44Z.

Tianqi Hang, Alessandro Giardini, Giovanni Biglino, Timothy Conover, Richard S. Figliola, and MOCHA Collaborative Group. In Vitro Validation of a Multiscale Patient-Specific Norwood Palliation Model. *ASAIO J.*, 62(3):317–324, June 2016. ISSN 1538-943X. doi: 10.1097/MAT.0000000000000336.

Hoda Hatoum, Atieh Yousefi, Scott Lilly, Pablo Maureira, Juan Crestanello, and Lakshmi P. Dasi. An in vitro evaluation of turbulence after transcatheter aortic valve implantation. *J Thorac Cardiovasc Surg*, 156(5):1837–1848, November 2018. ISSN 1097-685X. doi: 10.1016/j.jtcvs.2018.05.042.

Hoda Hatoum, Lakshmi Prasad Dasi, and Vinod H. Thourani. Surgical Aortic Valve Sizing: Imagine the Benefits of Imaging. *The Annals of Thoracic Surgery*, 110 (5):1511, November 2020. ISSN 0003-4975. doi: 10.1016/j.athoracsur.2020.03.099. Publisher: Elsevier.

Ivo R. Henkens, Alexander van Straten, Martin J. Schalij, Mark G. Hazekamp, Albert de Roos, Ernst E. van der Wall, and Hubert W. Vliegen. Predicting Outcome of Pulmonary Valve Replacement in Adult Tetralogy of Fallot Patients. *The Annals of Thoracic Surgery*, 83(3):907–911, March 2007. ISSN 0003-4975. doi: 10.1016/j.athoracsur.2006.09.090. URL `https://www.sciencedirect.com/science/article/pii/S0003497506019163`.

Aaron T Hess, Malenka M Bissell, Steffan J Glaze, Alex Pitcher, Saul Myerson, Stefan Neubauer, and Matthew D Robson. Evaluation of Circulation as a quantifying metric in 4D flow MRI. *J Cardiovasc Magn Reson*, 15(Suppl 1): E36, January 2013. ISSN 1097-6647. doi: 10.1186/1532-429X-15-S1-E36. URL `https://www.ncbi.nlm.nih.gov/pmc/articles/PMC3559358/`.

Jennifer C. Hirsch, Ralph S. Mosca, and Edward L. Bove. Complete Repair of Tetralogy of Fallot in the Neonate. *Ann Surg*, 232(4):508–514, October 2000. ISSN 0003-4932. URL `https://www.ncbi.nlm.nih.gov/pmc/articles/PMC1421183/`.

Julien I. E Hoffman and Samuel Kaplan. The incidence of congenital heart disease. *Journal of the American College of Cardiology*, 39(12):1890–1900, June 2002. ISSN 0735-1097. doi: 10.1016/S0735-1097(02)01886-7. URL `https://www.sciencedirect.com/science/article/pii/S0735109702018867`.

Kathryn W. Holmes. Timing of Pulmonary Valve Replacement in Tetralogy of Fallot Using Cardiac Magnetic Resonance Imaging. *Journal of the American College of Cardiology*, 60(11):1015–1017, September 2012. doi: 10.1016/j.jacc.2012.05.026. URL `https://www.jacc.org/doi/full/10.1016/j.jacc.2012.05.026`. Publisher: American College of Cardiology Foundation.

Kimberly A. Holst, Sameh M. Said, Timothy J. Nelson, Bryan C. Cannon, and Joseph A. Dearani. Current Interventional and Surgical Management of Congenital Heart Disease. *Circulation Research*, 120(6): 1027–1044, March 2017. doi: 10.1161/CIRCRESAHA.117.309186. URL `https://www.ahajournals.org/doi/full/10.1161/circresaha.117.309186`. Publisher: American Heart Association.

Syed F. Hussaini, David R. Rutkowski, Alejandro Roldán-Alzate, and Christopher J. François. Left and right ventricular kinetic energy using time-resolved versus time-average ventricular volumes. *Journal of Magnetic Resonance Imaging*, 45(3): 821–828, 2017. ISSN 1522-2586. doi: https://doi.org/10.1002/jmri.25416. URL `https://onlinelibrary.wiley.com/doi/abs/10.1002/jmri.25416`. _eprint: https://onlinelibrary.wiley.com/doi/pdf/10.1002/jmri.25416.

Raluca Ionescu-Ittu, Andrew S. Mackie, Michal Abrahamowicz, Louise Pilote, Christo Tchervenkov, Giuseppe Martucci, and Ariane J. Marelli. Valvular Operations in Patients With Congenital Heart Disease: Increasing Rates From 1988 to 2005. *The Annals of Thoracic Surgery*, 90(5):1563–1569, November 2010. ISSN 0003-4975. doi: 10.1016/j.athoracsur.2010.07.017. URL `https://www.sciencedirect.com/science/article/pii/S0003497510016279`.

Daniel Jeong, Petros V. Anagnostopoulos, Alejandro Roldan-Alzate, Shardha Srinivasan, Mark L. Schiebler, Oliver Wieben, and Christopher J. François. Ventricular kinetic energy may provide a novel noninvasive way to assess ventricular performance in patients with repaired tetralogy of Fallot. *J. Thorac. Cardiovasc. Surg.*, 149(5):1339–1347, May 2015. ISSN 1097-685X. doi: 10.1016/j.jtcvs.2014.11.085.

Alexander D. Kaiser, David M. McQueen, and Charles S. Peskin. Modeling the mitral valve. *International Journal for Numerical Methods in Biomedical Engineering*, 35(11):e3240, 2019. ISSN 2040-7947. doi: 10.1002/cnm.3240. URL `https://onlinelibrary.wiley.com/doi/abs/10.1002/cnm.3240`. _eprint: https://onlinelibrary.wiley.com/doi/pdf/10.1002/cnm.3240.

Alexander D. Kaiser, Rohan Shad, William Hiesinger, and Alison L. Marsden. A Design-Based Model of the Aortic Valve for Fluid-Structure Interaction. *Biomechanics and Modeling in Mechanobiology*, 2021. Accepted, To appear.

Kirk R. Kanter, Jason M. Budde, W. James Parks, Vincent K. H. Tam, Shiva Sharma, Willis H. Williams, and Derek A. Fyfe. One hundred pulmonary valve replacements in children after relief of right ventricular outflow tract obstruction. *Ann Thorac Surg*, 73(6):1801–1806; discussion 1806–1807, June 2002. ISSN 0003-4975. doi: 10.1016/s0003-4975(02)03568-3.

Tara Karamlou, Ross M. Ungerleider, Bahaaldin Alsoufi, Grant Burch, Michael Silberbach, Mark Reller, and Irving Shen. Oversizing pulmonary homograft conduits does not significantly decrease allograft failure in children. *Eur J Cardiothorac Surg*, 27(4):548–553, April 2005. ISSN 1010-7940. doi: 10.1016/j.ejcts.2004.12.054. URL `https://academic.oup.com/ejcts/article/27/4/548/372087`.

Sachin Khambadkone, Louise Coats, Andrew Taylor, Younes Boudjemline, Graham Derrick, Victor Tsang, Jeffrey Cooper, Vivek Muthurangu, Sanjeet R. Hegde, Reza S. Razavi, Denis Pellerin, John Deanfield, and Philipp Bonhoeffer. Percutaneous Pulmonary Valve Implantation in Humans. *Circulation*, 112(8): 1189–1197, August 2005. doi: 10.1161/CIRCULATIONAHA.104.523266. URL `https://www.ahajournals.org/doi/10.1161/CIRCULATIONAHA.104.523266`. Publisher: American Heart Association.

Amber D. Khanna, Kevin D. Hill, Sara K. Pasquali, Amelia S. Wallace, Frederick A. Masoudi, Marshall L. Jacobs, Jeffrey P. Jacobs, and Tara Karamlou. Benchmark Outcomes for Pulmonary Valve Replacement Using The Society of Thoracic Surgeons Databases. *The Annals of Thoracic Surgery*, 100(1):138–146, July 2015. ISSN 0003-4975. doi: 10.1016/j.athoracsur.2015.03.025. URL `http://www.sciencedirect.com/science/article/pii/S0003497515004063`.

John W. Kirklin, Eugene H. Blackstone, Richard A. Jonas, Yasuhisa Shimazaki, James K. Kirklin, John E. Mayer, Albert D. Pacifico, and Aldo R. Castaneda. Morphologic and surgical determinants of outcome events after repair of tetralogy of Fallot and pulmonary stenosis: A two-institution study. *The Journal of Thoracic and Cardiovascular Surgery*, 103(4):706–723, April 1992. ISSN 0022-5223. doi: 10.1016/S0022-5223(19)34954-2. URL `https://www.sciencedirect.com/science/article/pii/S0022522319349542`.

G. Kleinveld, R.W. Joyner, D. Sallee, K.R. Kanter, and W.J. Parks. Hemodynamic and Electrocardiographic Effects of Early Pulmonary Valve Replacement in Pediatric Patients After Transannular Complete Repair of Tetralogy of Fallot. *Pediatr Cardiol*, 27(3):329–335, June 2006. ISSN 1432-1971. doi: 10.1007/s00246-005-1137-7. URL `https://doi.org/10.1007/s00246-005-1137-7`.

Brian E. Kogon, Katherine A. Rodby, Paul M. Kirshbom, Kirk R. Kanter, Teresa Lyle, Michael McConnell, and Wendy M. Book. Adult Congenital Pulmonary

Valve Replacement: A Simple, Effective, and Reproducible Technique. *Congenital Heart Disease*, 2(5):314–318, 2007. ISSN 1747-0803. doi: 10.1111/j.1747-0803.2007.00118.x.

K. Z. Konakci, B. Bohle, R. Blumer, W. Hoetzenecker, G. Roth, B. Moser, G. Boltz-Nitulescu, M. Gorlitzer, W. Klepetko, E. Wolner, and H. J. Ankersmit. Alpha-Gal on bioprostheses: xenograft immune response in cardiac surgery. *Eur J Clin Invest*, 35(1):17–23, January 2005. ISSN 0014-2972. doi: 10.1111/j.1365-2362.2005.01441.x.

Ethan O. Kung and Charles A. Taylor. Development of A Physical Windkessel Module to Re-Create In-Vivo Vascular Flow Impedance for In-Vitro Experiments. *Cardiovasc Eng Technol*, 2(1):2–14, March 2011. ISSN 1869-408X. doi: 10.1007/s13239-010-0030-6. URL `https://www.ncbi.nlm.nih.gov/pmc/articles/PMC4548962/`.

Ethan O. Kung, Andrea S. Les, C. Alberto Figueroa, Francisco Medina, Karina Arcaute, Ryan B. Wicker, Michael V. McConnell, and Charles A. Taylor. In Vitro Validation of Finite Element Analysis of Blood Flow in Deformable Models. *Ann Biomed Eng*, 39(7):1947–1960, July 2011a. ISSN 1573-9686. doi: 10.1007/s10439-011-0284-7. URL `https://doi.org/10.1007/s10439-011-0284-7`.

Ethan O. Kung, Andrea S. Les, Francisco Medina, Ryan B. Wicker, Michael V. McConnell, and Charles A. Taylor. In Vitro Validation of Finite-Element Model of AAA Hemodynamics Incorporating Realistic Outlet Boundary Conditions. *J Biomech Eng*, 133(4), April 2011b. ISSN 0148-0731. doi: 10.1115/1.4003526.

Jae Gun Kwak, Cheul Lee, Mina Lee, Chang-Ha Lee, So-Ick Jang, Sang Yun Lee, Su-Jin Park, Mi Kyoung Song, and Seong-Ho Kim. Does implantation of larger bioprosthetic pulmonary valves in young patients guarantee durability in adults? Durability analysis of stented bioprosthetic valves in the pulmonary position in patients with Tetralogy of Fallot†. *Eur J Cardiothorac Surg*, 49(4):1207–1212, April 2016. ISSN 1873-734X. doi: 10.1093/ejcts/ezv298.

Claire Lawley, Kathryn Broadhouse, Fraser Callaghan, David Winlaw, Gemma

Figtree, and Stuart Grieve. 4D flow magnetic resonance imaging: role in pediatric congenital heart disease. *Asian Cardiovascular and Thoracic Annals*, 26: 021849231769424, February 2017. doi: 10.1177/0218492317694248.

Cheul Lee, Chun Soo Park, Chang-Ha Lee, Jae Gun Kwak, Soo-Jin Kim, Woo-Sup Shim, Jin Young Song, Eun Young Choi, and Sang Yun Lee. Durability of bioprosthetic valves in the pulmonary position: long-term follow-up of 181 implants in patients with congenital heart disease. *J. Thorac. Cardiovasc. Surg.*, 142(2):351–358, August 2011. ISSN 1097-685X. doi: 10.1016/j.jtcvs.2010.12.020.

Cheul Lee, Yang Min Kim, Chang-Ha Lee, Jae Gun Kwak, Chun Soo Park, Jin Young Song, Woo-Sup Shim, Eun Young Choi, Sang Yun Lee, and Jae Suk Baek. Outcomes of Pulmonary Valve Replacement in 170 Patients With Chronic Pulmonary Regurgitation After Relief of Right Ventricular Outflow Tract Obstruction: Implications for Optimal Timing of Pulmonary Valve Replacement. *Journal of the American College of Cardiology*, 60(11):1005–1014, September 2012. ISSN 0735-1097. doi: 10.1016/j.jacc.2012.03.077. URL `http://www.sciencedirect.com/science/article/pii/S073510971202325X`.

Cheul Lee, Chang-Ha Lee, and Jae Gun Kwak. Outcomes of redo pulmonary valve replacement for bioprosthetic pulmonary valve failure in 61 patients with congenital heart disease. *Eur J Cardiothorac Surg*, 50(3):470–475, September 2016. ISSN 1873-734X. doi: 10.1093/ejcts/ezw037.

Namheon Lee, Ashish Das, Rupak K. Banerjee, and William M. Gottliebson. Comparison of stroke work between repaired tetralogy of Fallot and normal right ventricular physiologies. *Heart Vessels*, 28(1):76–85, January 2013. ISSN 1615-2573. doi: 10.1007/s00380-011-0212-7. URL `https://doi.org/10.1007/s00380-011-0212-7`.

Sang-Wook Lee, Luca Antiga, J. David Spence, and David A. Steinman. Geometry of the Carotid Bifurcation Predicts Its Exposure to Disturbed Flow. *Stroke*, 39(8):2341–2347, August 2008. doi: 10.1161/STROKEAHA.107.510644. URL `https://www.ahajournals.org/doi/10.1161/STROKEAHA.107.510644`. Publisher: American Heart Association.

Kenneth K. Liao, Xiaohuan Li, Ranjit John, Devesh M. Amatya, Lyle D. Joyce, Soon J. Park, Richard Bianco, and R. Morton Bolman. Mechanical stress: an independent determinant of early bioprosthetic calcification in humans. *Ann. Thorac. Surg.*, 86(2):491–495, August 2008. ISSN 1552-6259. doi: 10.1016/j.athoracsur.2008.03.061.

C W Lillehei, R L Varco, M Cohen, H E Warden, V L Gott, R A DeWall, C Patton, and J H Moller. The first open heart corrections of tetralogy of Fallot. A 26-31 year follow-up of 106 patients. *Ann Surg*, 204(4):490–502, October 1986. ISSN 0003-4932. URL `https://www.ncbi.nlm.nih.gov/pmc/articles/PMC1251326/`.

C. Walton Lillehei, Morley Cohen, Herbert E. Warden, Raymond C. Read, Joseph B. Aust, Richard A. DeWall, and Richard L. Varco. Direct Vision Intracardiac Surgical Correction of the Tetralogy of Fallot, Pentalogy of Fallot, and Pulmonary Atresia Defects. *Ann Surg*, 142(3):418–442, September 1955. ISSN 0003-4932. URL `https://www.ncbi.nlm.nih.gov/pmc/articles/PMC1465089/`.

W. L Lim, Y. T Chew, T. C Chew, and H. T Low. Pulsatile flow studies of a porcine bioprosthetic aortic valve in vitro: PIV measurements and shear-induced blood damage. *Journal of Biomechanics*, 34(11):1417–1427, November 2001. ISSN 0021-9290. doi: 10.1016/S0021-9290(01)00132-4. URL `http://www.sciencedirect.com/science/article/pii/S0021929001001324`.

Leslie M. Louvelle, Matthew G. Doyle, Glen S. Van Arsdell, and Cristina H. Amon. A Methodology to Assess Subregional Geometric Complexity for Tetralogy of Fallot Patients. *ASME J of Medical Diagnostics*, 2(4), November 2019. ISSN 2572-7958. doi: 10.1115/1.4044949.

George K. Lui, Susan Fernandes, and Doff B. McElhinney. Management of Cardiovascular Risk Factors in Adults With Congenital Heart Disease. *Journal of the American Heart Association*, 3(6):e001076, 2014. doi: 10.1161/JAHA.114.001076. URL `https://www.ahajournals.org/doi/full/10.1161/JAHA.114.001076`. Publisher: American Heart Association.

Qiancheng Luo, Xiaomin He, Zhiying Song, Xiaoyang Zhang, Zhirong Tong, Juanya Shen, Liwei Hu, Yumin Zhong, Jinlong Liu, and Jinghao Zheng. Preoperative Morphological Prediction of Early Reoperation Risk After Primary Repair in Tetralogy of Fallot: A Contemporary Analysis of 83 Cases. *Pediatr Cardiol*, June 2021. ISSN 1432-1971. doi: 10.1007/s00246-021-02635-9. URL `https://doi.org/10.1007/s00246-021-02635-9`.

Philipp Lurz, Louise Coats, Sachin Khambadkone, Johannes Nordmeyer, Younes Boudjemline, Silvia Schievano, Vivek Muthurangu, Twin Yen Lee, Giovanni Parenzan, Graham Derrick, Seamus Cullen, Fiona Walker, Victor Tsang, John Deanfield, Andrew M. Taylor, and Philipp Bonhoeffer. Percutaneous Pulmonary Valve Implantation. *Circulation*, 117(15):1964–1972, April 2008. doi: 10.1161/CIRCULATIONAHA.107.735779. URL `https://www.ahajournals.org/doi/10.1161/CIRCULATIONAHA.107.735779`. Publisher: American Heart Association.

A. López-Zazueta, R. Ledesma-Alonso, J. E. V. Guzman, and R. Zenit. Study of the Velocity and Strain Fields in the Flow Through Prosthetic Heart Valves. *J Biomech Eng*, 133(12), December 2011. ISSN 0148-0731. doi: 10.1115/1.4005475.

Katsuhide Maeda, George K. Lui, Yulin Zhang, Shiraz A. Maskatia, Anitra Romfh, Vamsi V. Yarlagadda, Frank L. Hanley, and Doff B. McElhinney. Durability of Pulmonary Valve Replacement with Large Diameter Stented Porcine Bioprostheses. *Seminars in Thoracic and Cardiovascular Surgery*, May 2021. ISSN 1043-0679. doi: 10.1053/j.semtcvs.2021.03.044. URL `https://www.sciencedirect.com/science/article/pii/S1043067921001921`.

Amir Manbachi, Yiemeng Hoi, Bruce A. Wasserman, Edward G. Lakatta, and

David A. Steinman. On the shape of the common carotid artery with implications for blood velocity profiles. *Physiol. Meas.*, 32(12):1885–1897, October 2011. ISSN 0967-3334. doi: 10.1088/0967-3334/32/12/001. URL `https://doi.org/10.1088/0967-3334/32/12/001`. Publisher: IOP Publishing.

Ariane J. Marelli, Andrew S. Mackie, Raluca Ionescu-Ittu, Elham Rahme, and Louise Pilote. Congenital Heart Disease in the General Population: Changing Prevalence and Age Distribution. *Circulation*, 115(2):163–172, January 2007. ISSN 0009-7322, 1524-4539. doi: 10.1161/CIRCULATIONAHA.106.627224. URL `https://www.ahajournals.org/doi/10.1161/CIRCULATIONAHA.106.627224`.

Ariane J. Marelli, Raluca Ionescu-Ittu, Andrew S. Mackie, Liming Guo, Nandini Dendukuri, and Mohammed Kaouache. Lifetime Prevalence of Congenital Heart Disease in the General Population From 2000 to 2010. *Circulation*, 130(9):749–756, August 2014. doi: 10.1161/CIRCULATIONAHA.113.008396. Publisher: American Heart Association.

Michael Markl, Frandics P. Chan, Marcus T. Alley, Kris L. Wedding, Mary T. Draney, Chris J. Elkins, David W. Parker, Ryan Wicker, Charles A. Taylor, Robert J. Herfkens, and Norbert J. Pelc. Time-resolved three-dimensional phase-contrast MRI. *Journal of Magnetic Resonance Imaging*, 17(4):499–506, 2003. ISSN 1522-2586. doi: 10.1002/jmri.10272. URL `https://onlinelibrary.wiley.com/doi/abs/10.1002/jmri.10272`.

Michael Markl, Alex Frydrychowicz, Sebastian Kozerke, Mike Hope, and Oliver Wieben. 4D flow MRI. *J. Magn. Reson. Imaging*, 36(5):1015–1036, November 2012. ISSN 10531807. doi: 10.1002/jmri.23632. URL `http://doi.wiley.com/10.1002/jmri.23632`.

Gerard R. Martin and Richard A. Jonas. Surgery for Congenital Heart Disease: Improvements in Outcomes. *Am J Perinatol*, 35(6):557–560, May 2018. ISSN 0735-1631, 1098-8785. doi: 10.1055/s-0038-1639358. URL `http://www.thieme-connect.de/DOI/DOI?10.1055/s-0038-1639358`. Publisher: Thieme Medical Publishers.

Doff B. McElhinney, William E. Hellenbrand, Evan M. Zahn, Thomas K. Jones, John P. Cheatham, James E. Lock, and Julie A. Vincent. Short- and Medium-Term Outcomes After Transcatheter Pulmonary Valve Placement in the Expanded Multicenter US Melody Valve Trial. *Circulation*, 122(5): 507–516, August 2010. doi: 10.1161/CIRCULATIONAHA.109.921692. URL `https://www.ahajournals.org/doi/10.1161/CIRCULATIONAHA.109.921692`. Publisher: American Heart Association.

Doff B. McElhinney, Cheatham John P., Jones Thomas K., Lock James E., Vincent Julie A., Zahn Evan M., and Hellenbrand William E. Stent Fracture, Valve Dysfunction, and Right Ventricular Outflow Tract Reintervention After Transcatheter Pulmonary Valve Implantation. *Circulation: Cardiovascular Interventions*, 4(6): 602–614, December 2011. doi: 10.1161/CIRCINTERVENTIONS.111.965616.

Rafael Medero, Carson Hoffman, and Alejandro Roldán-Alzate. Comparison of 4D Flow MRI and Particle Image Velocimetry Using an In Vitro Carotid Bifurcation Model. *Ann Biomed Eng*, 46(12):2112–2122, December 2018. ISSN 1573-9686. doi: 10.1007/s10439-018-02109-9. URL `https://doi.org/10.1007/s10439-018-02109-9`.

Rafael Medero, Katrina Ruedinger, David Rutkowski, Kevin Johnson, and Alejandro Roldán-Alzate. In Vitro Assessment of Flow Variability in an Intracranial Aneurysm Model Using 4D Flow MRI and Tomographic PIV. *Ann Biomed Eng*, June 2020. ISSN 1573-9686. doi: 10.1007/s10439-020-02543-8. URL `https://doi.org/10.1007/s10439-020-02543-8`.

F. Migliavacca, G. Pennati, G. Dubini, R. Fumero, R. Pietrabissa, G. Urcelay, E. L. Bove, T. Y. Hsia, and M. R. de Leval. Modeling of the Norwood circulation: effects of shunt size, vascular resistances, and heart rate. *Am. J. Physiol. Heart Circ. Physiol.*, 280(5):H2076–2086, May 2001. ISSN 0363-6135. doi: 10.1152/ajpheart.2001.280.5.H2076.

Fotios M. Mitropoulos, Meletios A. Kanakis, Christos Ntellos, Constantinos Loukas, Periklis Davlouros, Theophili Kousi, and Andrew C. Chatzis. Pulmonary valve replacement in patients with corrected tetralogy of Fallot. *J Cardiovasc Thorac Res*, 9(2):71–77, 2017. ISSN 2008-5117. doi: 10.15171/jcvtr.2017.12.

Philip Moons, Lore Bovijn, Werner Budts, Ann Belmans, and Marc Gewillig. Temporal Trends in Survival to Adulthood Among Patients Born With Congenital Heart Disease From 1970 to 1992 in Belgium. *Circulation*, 122(22): 2264–2272, November 2010. doi: 10.1161/CIRCULATIONAHA.110.946343. URL `https://www.ahajournals.org/doi/10.1161/CIRCULATIONAHA.110.946343`. Publisher: American Heart Association.

Umberto Morbiducci, Annette M. Kok, Brenda R. Kwak, Peter H. Stone, David A. Steinman, and Jolanda J. Wentzel. Atherosclerosis at arterial bifurcations: evidence for the role of haemodynamics and geometry. *Thromb Haemost*, 115 (03):484–492, 2016. ISSN 0340-6245, 2567-689X. doi: 10.1160/th15-07-0597. URL `http://www.thieme-connect.de/DOI/DOI?10.1160/th15-07-0597`. Publisher: Schattauer GmbH.

Justine B. Nasejje, Henry Mwambi, Keertan Dheda, and Maia Lesosky. A comparison of the conditional inference survival forest model to random survival forests based on a simulation study as well as on two applications with time-to-event data. *BMC Med Res Methodol*, 17, July 2017. ISSN 1471-2288. doi: 10.1186/s12874-017-0383-8. URL `https://www.ncbi.nlm.nih.gov/pmc/articles/PMC5534080/`.

Kien T. Nguyen, Christopher D. Clark, Thomas J. Chancellor, and Dimitrios V. Papavassiliou. Carotid geometry effects on blood flow and on risk for vascular disease. *Journal of Biomechanics*, 41(1):11–19, January 2008. ISSN 0021-9290. doi: 10.1016/j.jbiomech.2007.08.012. URL `https://www.sciencedirect.com/science/article/pii/S0021929007003491`.

Yen Ngoc Nguyen, Munirah Ismail, Foad Kabinejadian, Chi Wei Ong, Edgar Lik Wui Tay, and Hwa Liang Leo. Experimental Study of Right Ventricular Hemodynamics After Tricuspid Valve Replacement Therapies to Treat Tricuspid Regurgitation. *Cardiovasc Eng Technol*, 8(4):401–418, 2017. ISSN 1869-4098. doi: 10.1007/s13239-017-0328-8.

Lili Niu, Xiliang Zhu, Min Pan, Abbott Derek, Lisheng Xu, Long Meng, and Hairong Zheng. Influence of vascular geometry on local hemodynamic parameters: phantom and small rodent study. *BioMedical Engineering OnLine*, 17 (1):30, March 2018. ISSN 1475-925X. doi: 10.1186/s12938-018-0458-8. URL `https://doi.org/10.1186/s12938-018-0458-8`.

Johannes Nordmeyer, Victor Tsang, Régis Gaudin, Philipp Lurz, Alessandra Frigiola, Alexander Jones, Silvia Schievano, Carin van Doorn, Philipp Bonhoeffer, and Andrew M. Taylor. Quantitative assessment of homograft function 1 year after insertion into the pulmonary position: impact of in situ homograft geometry on valve competence. *Eur. Heart J.*, 30(17):2147–2154, September 2009. ISSN 1522-9645. doi: 10.1093/eurheartj/ehp204.

Jose Maria Oliver, Diego Garcia-Hamilton, Ana Elvira Gonzalez, Jose Ruiz-Cantador, Angel Sanchez-Recalde, Maria Luz Polo, and Angel Aroca. Risk Factors for Prosthetic Pulmonary Valve Failure in Patients With Congenital Heart Disease. *The American Journal of Cardiology*, 116(8):1252–1256, October 2015. ISSN 0002-9149. doi: 10.1016/j.amjcard.2015.07.043. URL `http://www.sciencedirect.com/science/article/pii/S0002914915017038`.

Thomas Oosterhof, Alexander van Straten, Hubert W. Vliegen, Folkert J. Meijboom, Arie P. J. van Dijk, Anje M. Spijkerboer, Berto J. Bouma, Aeilko H. Zwinderman, Mark G. Hazekamp, Albert de Roos, and Barbara J. M. Mulder. Preoperative thresholds for pulmonary valve replacement in patients with corrected tetralogy of Fallot using cardiovascular magnetic resonance. *Circulation*, 116(5):545–551, July 2007. ISSN 1524-4539. doi: 10.1161/CIRCULATIONAHA.106.659664.

C. A. Palacios-Morales, J. E. V. Guzmán, A. Beltrán, L. Ruiz-Huerta, A. Caballero-Ruiz, and R. Zenit. On the maximum operating frequency of prosthetic heart valves. *Biomedical Physics & Engineering Express*, 4(4):047007, June 2018. ISSN 2057-1976. doi: 10.1088/2057-1976/aacc2e.

N. J. Pelc. Flow quantification and analysis methods. *Magn Reson Imaging Clin N Am*, 3(3):413–424, August 1995. ISSN 1064-9689.

N. J. Pelc, F. G. Sommer, K. C. Li, T. J. Brosnan, R. J. Herfkens, and D. R. Enzmann. Quantitative magnetic resonance flow imaging. *Magn Reson Q*, 10(3):125–147, September 1994. ISSN 0899-9422.

Changnong Peng, Xiaoqing Wang, Zhanchao Xian, Xin Liu, Wenhua Huang, Pengcheng Xu, and Jinyang Wang. The Impact of the Geometric Characteristics on the Hemodynamics in the Stenotic Coronary Artery. *PLOS ONE*, 11(6):e0157490, June 2016. ISSN 1932-6203. doi: 10.1371/journal.pone.0157490. Publisher: Public Library of Science.

Charles S. Peskin. The immersed boundary method. *Acta Numerica*, 11:479–517, January 2002. ISSN 1474-0508, 0962-4929. doi: 10.1017/S0962492902000077. Publisher: Cambridge University Press.

Vrishank Raghav, Sudeep Sastry, and Neelakantan Saikrishnan. Experimental Assessment of Flow Fields Associated with Heart Valve Prostheses Using Particle Image Velocimetry (PIV): Recommendations for Best Practices. *Cardiovasc Eng Technol*, 9(3):273–287, 2018. ISSN 1869-4098. doi: 10.1007/s13239-018-0348-z.

Vrishank Raghav, Chris Clifford, Prem Midha, Ikechukwu Okafor, Brian Thurow, and Ajit Yoganathan. Three-dimensional extent of flow stagnation in transcatheter heart valves. *Journal of The Royal Society Interface*, 16(154):20190063, May 2019. doi: 10.1098/rsif.2019.0063. URL `https://royalsocietypublishing.org/doi/full/10.1098/rsif.2019.0063`.

Gert Reiter, Ursula Reiter, Gabor Kovacs, Bernhard Kainz, Karin Schmidt, Robert Maier, Horst Olschewski, and Rainer Rienmueller. Magnetic resonance-derived 3-dimensional blood flow patterns in the main pulmonary artery as a marker of pulmonary hypertension and a measure of elevated mean pulmonary arterial pressure. *Circ Cardiovasc Imaging*, 1(1):23–30, July 2008. ISSN 1942-0080. doi: 10.1161/CIRCIMAGING.108.780247.

Alejandro Roldán-Alzate, Sylvana García-Rodríguez, Petros V. Anagnostopoulos, Shardha Srinivasan, Oliver Wieben, and Christopher J. François. Hemodynamic study of TCPC using in vivo and in vitro 4D Flow MRI and numerical simulation. *J Biomech*, 48(7):1325–1330, May 2015. ISSN 1873-2380. doi: 10.1016/j.jbiomech.2015.03.009.

Christoph Roloff, Daniel Stucht, Oliver Beuing, and Philipp Berg. Comparison of intracranial aneurysm flow quantification techniques: standard PIV vs stereoscopic PIV vs tomographic PIV vs phase-contrast MRI vs CFD. *Journal of NeuroInterventional Surgery*, 11(3):275–282, March 2019. ISSN 1759-8478, 1759-8486. doi: 10.1136/neurintsurg-2018-013921. URL `https://jnis.bmj.com/content/11/3/275`. Publisher: British Medical Journal Publishing Group Section: Basic Science.

Michael S Sacks and Ajit P Yoganathan. Heart valve function: a biomechanical perspective. *Philos Trans R Soc Lond B Biol Sci*, 362(1484):1369–1391, August 2007. ISSN 0962-8436. doi: 10.1098/rstb.2007.2122. URL `https://www.ncbi.nlm.nih.gov/pmc/articles/PMC2440402/`.

Michael S. Sacks, W. David Merryman, and David E. Schmidt. ON THE BIOMECHANICS OF HEART VALVE FUNCTION. *J Biomech*, 42(12):1804–1824, August 2009. ISSN 0021-9290. doi: 10.1016/j.jbiomech.2009.05.015. URL `https://www.ncbi.nlm.nih.gov/pmc/articles/PMC2746960/`.

Erwan Salaun, Anne-Sophie Zenses, Morgane Evin, Frédéric Collart, Gilbert Habib, Philippe Pibarot, and Régis Rieu. Effect of oversizing and elliptical shape of aortic annulus on transcatheter valve hemodynamics: An in vitro study. *International Journal of Cardiology*, 208:28–35, April 2016. ISSN 0167-5273. doi: 10.1016/j.ijcard.2016.01.048. URL `https://www.sciencedirect.com/science/article/pii/S0167527316300250`.

Nicole K. Schiavone, Christopher J. Elkins, Doff B. McElhinney, John K.

Eaton, and Alison L. Marsden. In Vitro Assessment of Right Ventricular Outflow Tract Anatomy and Valve Orientation Effects on Bioprosthetic Pulmonary Valve Hemodynamics. *Cardiovasc Eng Tech*, January 2021. ISSN 1869-4098. doi: 10.1007/s13239-020-00507-6. URL `https://doi.org/10.1007/s13239-020-00507-6`.

Silvia Schievano, Louise Coats, Francesco Migliavacca, Wendy Norman, Alessandra Frigiola, John Deanfield, Philipp Bonhoeffer, and Andrew Taylor. Variations in Right Ventricular Outflow Tract Morphology Following Repair of Congenital Heart Disease: Implications for Percutaneous Pulmonary Valve Implantation. *Journal of cardiovascular magnetic resonance : official journal of the Society for Cardiovascular Magnetic Resonance*, 9:687–95, February 2007. doi: 10.1080/10976640601187596.

Silvia Schievano, Andrew M. Taylor, Claudio Capelli, Louise Coats, Fiona Walker, Philipp Lurz, Johannes Nordmeyer, Sue Wright, Sachin Khambadkone, Victor Tsang, Mario Carminati, and Philipp Bonhoeffer. First-in-man implantation of a novel percutaneous valve: a new approach to medical device development. *EuroIntervention*, 5(6):745–750, January 2010. ISSN 1969-6213. doi: 10.4244/eijv5i6a122.

Silvia Schievano, Claudio Capelli, Carol Young, Philipp Lurz, Johannes Nordmeyer, Catherine Owens, Philipp Bonhoeffer, and Andrew M. Taylor. Four-dimensional computed tomography: a method of assessing right ventricular outflow tract and pulmonary artery deformations throughout the cardiac cycle. *Eur Radiol*, 21(1): 36–45, January 2011. ISSN 1432-1084. doi: 10.1007/s00330-010-1913-5. URL `https://doi.org/10.1007/s00330-010-1913-5`.

F. J. Schoen and R. J. Levy. Tissue heart valves: current challenges and future research perspectives. *J Biomed Mater Res*, 47(4):439–465, December 1999. ISSN 0021-9304. doi: 10.1002/(sici)1097-4636(19991215)47:4¡439::aid-jbm1¿3.0.co;2-o.

F. J. Schoen, J. Fernandez, L. Gonzalez-Lavin, and A. Cernaianu. Causes of failure and pathologic findings in surgically removed Ionescu-Shiley standard bovine pericardial heart valve bioprostheses: emphasis on progressive structural deterioration. *Circulation*, 76(3):618–627, September 1987. ISSN 0009-7322. doi: 10.1161/01.cir.76.3.618.

Sara Søndergaard Schwartz, Nicolas Madsen, Henning Bækgaard Laursen, Russel Hirsch, and Morten Smærup Olsen. Incidence and Mortality of Adults With Pulmonary Hypertension and Congenital Heart Disease. *The American Journal of Cardiology*, 121(12):1610–1616, June 2018. ISSN 0002-9149. doi: 10.1016/j.amjcard.2018.02.051. URL `https://www.sciencedirect.com/science/article/pii/S000291491830287X`.

Michal Schäfer, Stephen Humphries, Kurt R. Stenmark, Vitaly O. Kheyfets, J. Kern Buckner, Kendall S. Hunter, and Brett E. Fenster. 4D-flow cardiac magnetic resonance-derived vorticity is sensitive marker of left ventricular diastolic dysfunction in patients with mild-to-moderate chronic obstructive pulmonary disease. *Eur Heart J Cardiovasc Imaging*, 19(4):415–424, 2018. ISSN 2047-2412. doi: 10.1093/ehjci/jex069.

Shawn C. Shadden, Matteo Astorino, and Jean-Frédéric Gerbeau. Computational analysis of an aortic valve jet with Lagrangian coherent structures. *Chaos*, 20 (1):017512, January 2010. ISSN 1054-1500. doi: 10.1063/1.3272780. URL `https://aip.scitation.org/doi/10.1063/1.3272780`.

Wan-Chen Shen, Chun-An Chen, Chung-I Chang, Yih-Sharng Chen, Shu-Chien Huang, Mei-Hwan Wu, and Jou-Kou Wang. Outflow tract geometries are associated with adverse outcome indicators in repaired tetralogy of Fallot. *The Journal of Thoracic and Cardiovascular Surgery*, 162(1):196–205, July 2021. ISSN 0022-5223. doi: 10.1016/j.jtcvs.2020.09.072. URL `https://www.sciencedirect.com/science/article/pii/S0022522320326702`.

Yubing Shi, Patricia Lawford, and Rodney Hose. Review of Zero-D and 1-D Models of Blood Flow in the Cardiovascular System. *BioMedical Engineering OnLine*, 10(1):33, April 2011. ISSN 1475-925X. doi: 10.1186/1475-925X-10-33. URL `https://doi.org/10.1186/1475-925X-10-33`.

Raheela Fareed Siddiqui, Johnathan Rajiv Abraham, and Jagdish Butany. Bioprosthetic heart valves: modes of failure. *Histopathology*, 55(2):135–144, August 2009. ISSN 1365-2559. doi: 10.1111/j.1365-2559.2008.03190.x.

Pia Sjöberg, Sebastian Bidhult, Jelena Bock, Einar Heiberg, Håkan Arheden, Ronny Gustafsson, Shahab Nozohoor, and Marcus Carlsson. Disturbed left and right ventricular kinetic energy in patients with repaired tetralogy of Fallot: pathophysiological insights using 4D-flow MRI. *Eur Radiol*, 28(10):4066–4076, October 2018. ISSN 1432-1084. doi: 10.1007/s00330-018-5385-3.

Clayton A. Smith, Courtney McCracken, Amanda S. Thomas, Logan G. Spector, James D. St Louis, Matthew E. Oster, James H. Moller, and Lazaros Kochilas. Long-term Outcomes of Tetralogy of Fallot: A Study From the Pediatric Cardiac Care Consortium. *JAMA Cardiol*, 4(1):34–41, January 2019. ISSN 2380-6591. doi: 10.1001/jamacardio.2018.4255.

Simon J. Sonntag, Maximilan Kütting, Pejman Farhadi Ghalati, Tim Kaufmann, Jaime Vazquez-Jimenez, Ulrich Steinseifer, and Janez Vodiskar. Effect of Pulmonary Conduit Oversizing on Hemodynamics in Children. *Int J Artif Organs*, 38(10):548–556, October 2015. ISSN 0391-3988. doi: 10.5301/ijao.5000443. URL `https://doi.org/10.5301/ijao.5000443`. Publisher: SAGE Publications Ltd STM.

Fotis Sotiropoulos, Trung Bao Le, and Anvar Gilmanov. Fluid Mechanics of Heart Valves and Their Replacements. *Annual Review of Fluid Mechanics*, 48(1):259–283, 2016. doi: 10.1146/annurev-fluid-122414-034314. URL `https://doi.org/10.1146/annurev-fluid-122414-034314`.

Zoran Stankovic, Bradley D. Allen, Julio Garcia, Kelly B. Jarvis, and Michael Markl. 4D flow imaging with MRI. *Cardiovasc Diagn Ther*, 4(2):173–192, April 2014. ISSN 2223-3652. doi: 10.3978/j.issn.2223-3652.2014.01.02.

Viktória Stanová, Anne-Sophie Zenses, Lionel Thollon, Lyes Kadem, Paul Barragan, Régis Rieu, and Philippe Pibarot. Effects of hemodynamic conditions and valve sizing on leaflet bending stress in self-expanding transcatheter aortic valve: An in vitro study. *Artificial Organs*, 44(7):E277–E287, 2020. ISSN 1525-1594. doi: https://doi.org/10.1111/aor.13654. URL `https://onlinelibrary.wiley.com/doi/abs/10.1111/aor.13654`. _eprint: https://onlinelibrary.wiley.com/doi/pdf/10.1111/aor.13654.

Tariq Suleiman, Clifford J. Kavinsky, Clare Skerritt, Damien Kenny, Michael N. Ilbawi, and Massimo Caputo. Recent Development in Pulmonary Valve Replacement after Tetralogy of Fallot Repair: The Emergence of Hybrid Approaches. *Front Surg*, 2, June 2015. ISSN 2296-875X. doi: 10.3389/fsurg.2015.00022. URL `https://www.ncbi.nlm.nih.gov/pmc/articles/PMC4451578/`.

Kartik S. Sundareswaran, Christopher M. Haggerty, Diane de Zélicourt, Lakshmi P. Dasi, Kerem Pekkan, David H. Frakes, Andrew J. Powell, Kirk R. Kanter, Mark A. Fogel, and Ajit P. Yoganathan. Visualization of flow structures in Fontan patients using 3-dimensional phase contrast magnetic resonance imaging. *The Journal of Thoracic and Cardiovascular Surgery*, 143(5):1108–1116, May 2012. ISSN 0022-5223. doi: 10.1016/j.jtcvs.2011.09.067. URL `https://www.sciencedirect.com/science/article/pii/S0022522311011299`.

W. Milton Swanson and Richard E. Clark. Dimensions and Geometric Relationships of the Human Aortic Value as a Function of Pressure. *Circulation Research*, 35(6):871–882, December 1974. doi: 10.1161/01.RES.35.6.871. URL `https://www.ahajournals.org/doi/abs/10.1161/01.res.35.6.871`. Publisher: American Heart Association.

Beverly T. Tang, Tim A. Fonte, Frandics P. Chan, Philip S. Tsao, Jeffrey A. Feinstein, and Charles A. Taylor. Three-Dimensional Hemodynamics in the Human Pulmonary Arteries Under Resting and Exercise Conditions. *Ann Biomed Eng*, 39 (1):347–358, January 2011. ISSN 1573-9686. doi: 10.1007/s10439-010-0124-1. URL `https://doi.org/10.1007/s10439-010-0124-1`.

C van Doorn. The unnatural history of tetralogy of Fallot: surgical repair is not as definitive as previously thought. *Heart*, 88(5):447–448, November 2002. ISSN 1355-6037. URL `https://www.ncbi.nlm.nih.gov/pmc/articles/PMC1767405/`.

Alexander van Straten, Hubert W. Vliegen, Mark G. Hazekamp, Jeroen J. Bax, Paul H. Schoof, Jaap Ottenkamp, Ernst E. van der Wall, and Albert de Roos. Right Ventricular Function after Pulmonary Valve Replacement in Patients with Tetralogy of Fallot. *Radiology*, 233(3):824–829, December 2004. ISSN 0033-8419. doi: 10.1148/radiol.2333030804. URL `https://pubs.rsna.org/doi/10.1148/radiol.2333030804`.

Riccardo Vismara, Katia Laganà, Francesco Migliavacca, Silvia Schievano, Louise Coats, Andrew Taylor, and Philipp Bonhoeffer. Experimental Setup to Evaluate the Performance of Percutaneous Pulmonary Valved Stent in Different Outflow Tract Morphologies. *Artificial Organs*, 33(1):46–53, 2009. ISSN 1525-1594. doi: 10.1111/j.1525-1594.2008.00673.x.

Hubert W. Vliegen, Alexander van Straten, Albert de Roos, Arno A.W. Roest, Paul H. Schoof, Aeilko H. Zwinderman, Jaap Ottenkamp, Ernst E. van der Wall, and Mark G. Hazekamp. Magnetic Resonance Imaging to Assess the Hemodynamic Effects of Pulmonary Valve Replacement in Adults Late After Repair of Tetralogy of Fallot. *Circulation*, 106(13):1703–1707, September 2002. doi: 10.1161/01.CIR.0000030995.59403.F8. Publisher: American Heart Association.

Wanpen Vongpatanasin, L. David Hillis, and Richard A. Lange. Prosthetic Heart Valves. *New England Journal of Medicine*, 335(6):407–416, August 1996. ISSN 0028-4793. doi: 10.1056/NEJM199608083350607. URL `https://doi.org/10.1056/NEJM199608083350607`.

Marija Vukicevic, Timothy Conover, Michael Jaeggli, Jian Zhou, Giancarlo Pennati, Tain-Yen Hsia, and Richard S. Figliola. Control of respiration-driven retrograde flow in the subdiaphragmatic venous return of the Fontan circulation. *ASAIO J.*, 60 (4):391–399, August 2014. ISSN 1538-943X. doi: 10.1097/MAT.0000000000000093.

Winfield J. Wells, Hector Arroyo, Ross M. Bremner, John Wood, and Vaughn A. Starnes. Homograft conduit failure in infants is not due to somatic outgrowth. *The Journal of Thoracic and Cardiovascular Surgery*, 124(1):88–96, July 2002. ISSN 0022-5223. doi: 10.1067/mtc.2002.121158. URL `http://www.sciencedirect.com/science/article/pii/S0022522302000442`.

Weiliang Wu, Jinxian He, and Xiaobo Shao. Incidence and mortality trend of congenital heart disease at the global, regional, and national level, 1990–2017. *Medicine (Baltimore)*, 99(23), June 2020. ISSN 0025-7974. doi: 10.1097/MD.0000000000020593. URL `https://www.ncbi.nlm.nih.gov/pmc/articles/PMC7306355/`.

Ajit P. Yoganathan, Zhaoming He, and S. Casey Jones. Fluid Mechanics of Heart Valves. *Annual Review of Biomedical Engineering*, 6 (1):331–362, 2004. doi: 10.1146/annurev.bioeng.6.040803.140111. URL `https://doi.org/10.1146/annurev.bioeng.6.040803.140111`.

Ajit P. Yoganathan, K. B. Chandran, and Fotis Sotiropoulos. Flow in Prosthetic Heart Valves: State-of-the-Art and Future Directions. *Ann Biomed Eng*, 33(12): 1689–1694, December 2005. ISSN 1573-9686. doi: 10.1007/s10439-005-8759-z. URL `https://doi.org/10.1007/s10439-005-8759-z`.

Evan M. Zahn, William E. Hellenbrand, James E. Lock, and Doff B. McElhinney. Implantation of the Melody Transcatheter Pulmonary Valve in Patients With a Dysfunctional Right Ventricular Outflow Tract Conduit. *Journal of the American College of Cardiology*, 54 (18):1722–1729, October 2009. doi: 10.1016/j.jacc.2009.06.034. URL `https://www.jacc.org/doi/full/10.1016/j.jacc.2009.06.034`. Publisher: American College of Cardiology Foundation.

Weimin Zhang, Jinlong Liu, Qin Yan, Jinfen Liu, Haifa Hong, and Le Mao. Computational haemodynamic analysis of left pulmonary artery angulation effects on pulmonary blood flow. *Interactive CardioVascular and Thoracic Surgery*, 23

(4):519–525, October 2016. ISSN 1569-9293. doi: 10.1093/icvts/ivw179. URL `https://doi.org/10.1093/icvts/ivw179`.

Rahel Zubairi, Sadia Malik, Robert D. B. Jaquiss, Michiaki Imamura, Jeff Gossett, and W. Robert Morrow. Risk Factors for Prosthesis Failure in Pulmonary Valve Replacement. *The Annals of Thoracic Surgery*, 91(2):561–565, February 2011. ISSN 0003-4975. doi: 10.1016/j.athoracsur.2010.07.111. URL `http://www.sciencedirect.com/science/article/pii/S0003497510018825`.